Dissertation
submitted to the
Combined Faculties for the Natural Sciences and for Mathematics
of the Ruperto-Carola University of Heidelberg, Germany
for the degree of
Doctor of Natural Sciences

presented by

Dipl. Phys. Rachik Soualah
born in Biskra, Algeria
Oral examination: 24 June 2009

Production of Neutral Pions in Pb+Au collisions at 158 AGeV/c

Referees: Prof. Dr. Johanna Stachel
Prof. Dr. Norbert Herrmann

Abstract

The direct photons are a particularly useful probe to search for an evidence of the Quark-Gluon Plasma formation in ultra-relativistic heavy-ion collisions. Direct photons can be extracted experimentally by measuring the large background from π^0 and η meson decays. This thesis work represents the production of the neutral pion mesons measured with the CERES/NA45 experiment at the top SPS energy in 158 AGeV/c Pb-Au collisions. The $\pi^0 \longrightarrow \gamma\gamma$ (98.8%) is the decay channel used in the reconstruction scheme. The π^0 measurement is based on the data taken in the year 2000. The CERES experiment can measure the photons that convert shortly before the TPC by measuring the e^+e^- pairs in the TPC. The RICH2 mirror is the main converter used for this analysis. The presented analysis method describes in more details the selection of the e^+ and e^- tracks using only the TPC information to reconstruct the converted photon. A Secondary vertex technique was developed and used to select the photons converted in the RICH2 mirror area. The extraction of the π^0 needs a careful study of the combinatorial background determined using the mixed event technique. The obtained invariant mass distribution of the two photons defined well the π^0 peak. The neutral pion transverse spectra compared to phenomenological models and other experiments validate our analysis method.

Direkte Photonen sind ein besonders gute Probe zum Nachweis eines Quark-Gluon-Plasmas in ultrarelativistischen Kollisionen von Schwerionen. Sie können experimentell nach der Messung des erheblichen Untergrundes aus Zerfällen von π^0- und η-Mesonen extrahiert werden. Die vorliegende Arbeit stellt die Erzeugung von neutralen Pionen vor, die innerhalb des CERES/NA5-Experimentes bei der topSPS-Energie von 158 $AGeV/c$ Pb-Au-Kollisionen gemessen wurden. Die Analyse basiert auf der Datennahme des Jahres 2000. Zur Rekonstruktion wurde der $\pi^0 \longrightarrow \gamma\gamma$-Zerfallskanal (98.8%) verwendet. Das CERES-Experiment kann Photonen, die kurz vor der TPC konvertieren, durch die Messung von e^+e-Paaren nachweisen. Der in dieser Arbeit verwendete Hauptkonverter ist der RICH2-Spiegel. Die hier vorgestellte Rekonstruktionsmethode beschreibt detailliert die Auswahl der e^+e-Spuren, wobei ausschliesslich TPC-Informationen zur Rekonstruktion konvertierter Photonen benutzt wurden. Eine Sekundär-Vertex-Technik wurde entwickelt und zur Auswahl von konvertierten Photonen im Bereich des RICH2-Spiegels verwendet. Zur Extraktrion der neutralen Pionen ist eine sorgfältige Studie des kombinatorischen Untergrundes erforderlich, welcher mittels Mixed-Event-Technik bestimmt wurde.

Die Verteilung der invarianten Massen von Photonpaaren zeigt den Peak bei der π^0-Masse sehr deutlich. Der Vergleich des hier ermittelten transversalen Spektrums fuer neutrale Pionen mit phänomenologischen Modellen und anderen Experimenten verifizieren diese Analysemethode.

To my grandmother ...

Contents

List of Figures

List of Tables

Prelude

The study of direct photons is a particularly useful probe to search for an evidence of the Quark-Gluon Plasma formation in ultra-relativistic heavy-ion collisions. Direct photons are very difficult to measure experimentally due to the large background from π^0 and η meson decays. In addition, the main source of systematic errors in the measurement of the dilepton pairs in the low mass range, main physics topic of the CERES experiment, comes from the η/π^0 ratio which is not measured with a good accuracy at SPS energies yet. If the measurement of the π^0 and η mesons yields would be possible with good accuracy within the CERES experiment, the systematic errors on the dilepton measurement would be reduced. The only possibility to measure photons in the CERES experiment is by reconstructing the converted photons.
The subject of this thesis is the measurement of π^0 meson production in Pb-Au collisions at 158 AGeV/c in the SPS using the CERES experiment. The π^0 measurement is based on the data taken in 2000. The organization of this Thesis is presented as follows:

The first Chapter is an introductory chapter. It illustrates a description on the theoretical part of the high energy heavy ion physics, which is dealing with the Quantum Chromo Dynamics. Starting from the Standard Model unification and the anticipation of the Strong interactions at the quark level. The main ideas which lead to the QGP creation and phenomenological models which are promoted by the experimental data are briefly discussed.

Chapter 2 presents the experimental apparatus of the CERES experiment and its different subdetectors. We will emphasize on the description of the Time Projection Chamber, since only the TPC information is used on the neutral pion production analysis.

The third Chapter explains the procedure used to reconstruct the neutral pions. The data selection and analysis scheme will be started with the measurement of the electrons pairs with opposite charge, then this Section will be followed by the reconstruction of the photons which convert (shortly) before the TPC mainly in the RICH2 mirror. For this purpose, we have developed a technique to reconstruct the Secondary vertices that allows to select the photon conversions in the RICH2 mirror region. The π^0 signal is obtained from the two photons invariant mass distributions after subtraction of the combinatorial background calculated using the mixed event

technique. The background subtracted two-photons invariant mass distributions are then investigated in various transverse momentum and rapidity phase-spaces in order to obtain the neutral pion transverse momentum distributions.

Chapter four is devoted to the Monte Carlo simulations description. The complete steps of the Monte Carlo method are presented and the obtained results are used for efficiency and acceptance corrections.

In Chapter five, the results of this work are presented. The neutral pion yields and the corrected transverse momentum distribution is obtained. The results are then compared to theoretical models as well as to other existing experimental data.

Finally, the conclusions and the summary of this Thesis work are given in Chapter six.

In any subject which has principles, causes, and elements, scientific knowledge and understanding stems from a grasp of these, for we think we know a thing only when we have grasped its first causes and principles and have traced it back to its elements

Aristotle, Physics

1 Introduction

1.1 The Standard Model

The laws of physics governing the world of elementary particles are now very well described by what we call the Standard Model [1, 2, 3] of particle physics fruit of major theoretical and experimental advances of the twentieth century. To describe and understand Nature, physicists have worked out to determine the basic constituents (elementary particles) which it is made of and to define the interactions that govern theirs fundamental interactions.
In nature there are 12 elementary particles and the 4 gauge bosons that describe the interactions of the standard model. It also provides that for every particle there is an anti-particle same mass but an opposed charge and parity. All these building blocks are grouped into three families growing masses. The stable matter particles composed of the first family whose members are the lightest.
Today, physics is understood through a series of elementary particles, which are classified into two main families: the fermions(particles of half-integer spin) and bosons (integer spin). The fermions follow the Pauli Exclusion Principle and they are the constituent particles of the ordinary matter-the proton, neutron and electron belong to this family. The bosons are the particles carrying the information exchanged between fermions during an interaction.
Among the fermions, six of them are classified as quarks (up, down, charm, strange, top, bottom), and the other six as leptons (electron, muon, tau, and their corresponding neutrinos). The quarks feel the strong interaction, and leptons are insensitive to it. Leptons are directly observable in nature. Quarks, however, are not

directly observed, they do not appear to exist by themselves as free particles. We can model each fundamental interaction between elementary particles by the exchange of bosons, namely particles integer spin, obeying the Bose-Einstein statistics which allows them to accumulate in the same conditions. These particles "carry" the interaction of a particle to another and are thus called vector bosons. Four interactions have been identified:
Electromagnetic interaction where the photon is the intermediate vector boson. The photon does not have itself an electric charge, it is neutral, and particles exchanging photons retain their electric charge unchanged after the exchange. The mass of the photon is zero; the electromagnetic interaction length is infinite.
The weak interaction with three vector bosons: Z^0, electrically neutral, and $W^{\pm}$ have an electric charge ± 1. It deals with all fermions through two charges, where one of these two charges is laid by the left handed fermions.
The strong interaction, the gauge bosons are the gluons and they form an octet. Among the fermions, only quarks have a known color, which may take three values appointed by agreement "red", "green" and "blue". These three new quantum number concept of colors was firstly proposed by Han and Nambu in 1964 [4]. The gluons also have this feature, a combination of colors and anti-colors, and can thus combine them. They have zero mass.
The standard model thus encompasses all known particles and the three interactions with a wide effect of the particle. This is done through the quantum field theory that constitutes the mathematical framework of the model. The standard model allows us to explain all natural phenomena except gravity, which is for the moment, resists the theorists for a quantum theory and which can be neglected during the interaction between elementary particles, because of the weakness of the gravitational intensity force compared to the previous forces [5, 6].
The structure of each interactions included in the Standard Model is dictated by the symmetry of the group which leaves the action invariant [7]. The model introduces the following gauge symmetry group:

$$SU(2)_L \otimes U(1)_Y \otimes SU(3)_C \tag{1.1}$$

The $SU(2)_L \otimes U(1)_Y$ gauge group combines both the electromagnetism and weak interaction theories into a single unified theory of electroweak theory [1] with the gauge group.
It contains four quanta of radiation, one for the $U(1)$ part and three for $SU(2)$. The term $SU(3)_C$ is the color gauge group which describes the strong interactions. The Gluons are its 8 quanta of radiation.

[1]The Glashow-Salam-Weinberg Model (GSW) where the particle physics collectively describe the electroweak and strong interactions of elementary

1.2 The Strong interactions

The Quantum ChromoDynamique (QCD) is the general accepted gauge theory [8, 9] used to describe the strong interactions [10, 11] between basic constituents of nuclear matter. This approach to standard model is certainly its most complicated component insofar as its Lagrangian uses only quarks and gluons to describe the confined states (hadrons). Quarks do not interact with each other directly; they do so through the gluons as intermediated agents. We can only refer to theirs presence in objects which are color singlets. A colored quark can be bound with an antiquark with the corresponding anti-color to form a *meson*. Three quarks of different colors can be bound to form *baryon*. Mesons and baryons are collectively called hadrons to be distinguished from the leptons and field bosons as the "particles" which can be directly measured.

1.2.1 The QCD Lagrangian

The QCD is a Yang-Mills theory of colored quarks and gluons introduced by Gell-Mann [12] and Zweig [13] in the 60's. It required the introduction of a new hidden quantum number in order to do not violate the Fermi Statistics for the particle $\Delta^{++}(uuu)$: color. All baryons (set of three quarks) and all mesons (pair of quark-antiquark) are color singlet states. Theirs symmetry properties are described by the $SU(3)_c$. We can define a local gauge transformation as the form:

$$U = \exp(g_3 \sum_a \alpha_a(x) T_a), a = 1, 8 \tag{1.2}$$

here the g_3 is the QCD coupling constant, the matrices T_a represent the generators of the $SU(3)_c$ gauge group and α_a are an arbitrary phases dependent on the space-time coordinates. The QCD Lagrangian involves a bosonic part and fermionic part, it takes the following form:

$$\mathcal{L}_{QCD} = -\frac{1}{4} F^a_{\mu\nu} F^{\mu\nu}_a + \sum_{q=1}^{6} (i\bar{\psi}_q \gamma^\mu D_\mu \psi q - m_q \bar{\psi}_q \psi_q) \tag{1.3}$$

with the field strength tensor:

$$F^a_{\mu\nu} = \partial_\mu A^a_\nu - \partial_\nu A^a_\mu - g_s f_{abc} A^b_\nu A^c_\mu \tag{1.4}$$

and the covariant derivative:

$$D_\mu = \partial_\mu + i g_s \frac{\lambda^a}{2} A^a_\mu \tag{1.5}$$

The last term in equation (1.4) contains the fundamental difference between QED and QCD which describes the self coupling of gluons [14]. This approach allows interaction between gluons giving rise to the definition of a vertex 3 or 4 gluons while in QED, the interaction between photons is not permitted. The six quarks q are represented by the spinors ψ_q which are the 4-component Dirac spinors associated with each quark field of *(3)* color i and flavor q, the A^a_ν are the (8) Yang-Mills (gluon) fields as well as the associated covariant derivatives D_μ and f_{abc} are the structure constants of the $SU(3)$ algebra. The very limited scale length of the strong interaction, of the order of 10^{-15} meters, is due to the gauge bosons self-coupling. This also particularly implies that the interaction strength between two quarks increases with their relative distance. The interaction between quarks grows weaker as the quarks approach one another more closely. These important properties of the strong interaction and its physics can be divided into two regimes: asymptotic freedom and confinement [15, 16].

1.2.2 Asymptotic freedom

One of the striking properties of QCD is the asymptotic freedom which leads to the Nobel prize for 2004 awarded to David Gross, David Politzer and Frank Wilczek. This important theoretical discovery states that the interaction strength between quarks becomes smaller as the distance between them gets shorter so that quarks behave almost as free particles. Similarly to the QED, the coupling constant of QCD is defined by

$$\alpha_s = \frac{g_s^2}{4\pi} \tag{1.6}$$

The α_s value shows a strong dependence on the momentum transfer Q^2 in a collision. The $\alpha_s(Q^2)$ evolution is governed by theory through the differential equation of renormalization group [17]:

$$Q^2 \frac{\partial \alpha_s}{\partial Q^2} = \beta(\alpha_s) \tag{1.7}$$

If we consider only the first order of α_s, the function is calculated by a perturbative treatment of QCD as a development of the strong coupling [18, 19] and written in the form:

$$\beta(\alpha_s) = -b\alpha_s^2(1 + b'\alpha_s + b''\alpha_s^2\vartheta(\alpha_s^3)) \quad \text{with} \quad \mathrm{b} = \frac{33 - 2\mathrm{n_f}}{12\pi} \tag{1.8}$$

For the leading order perturbative approximation the solution of this equation gives the variation of the coupling constant to the scale of the momentum transfer at large momentum:

$$\alpha_s(Q^2) = \frac{\alpha_0}{1 + \alpha_0 \frac{33-2n_f}{12\pi} \ln \frac{Q^2}{\mu^2}} \tag{1.9}$$

Where α_0 is the coupling constant for n_f number of active quark flavors with the momentum transfer μ.

From equation (1.8) we conclude that for a number of flavors less than 17, the coupling constant is decreasing slowly to zero when $Q^2 >> \mu^2$,i.e. precisely where the asymptotic freedom is. Therefore the quarks behave as they were free inside the hadrons. At this stage when the momentum transfer is large, the strong interaction physics can be calculated in perturbative theory. The variation of the coupling constant diverges for small values of $Q^2 < \mu^2$ where the application of perturbative treatment to calculate the physical observable inaccurate. In this prevailing order a new phenomenon, coming directly from the non-abelian propriety of the theory. Figure (1.1) illustrates the decreasing of the strong interaction coupling constant depending on the momentum transfer. The QCD is therefore perturbative and calculable at short distance (large Q): the asymptotic freedom. However, long-distance (low Q), the coupling constant becomes too big and the perturbative calculations are no longer valid.

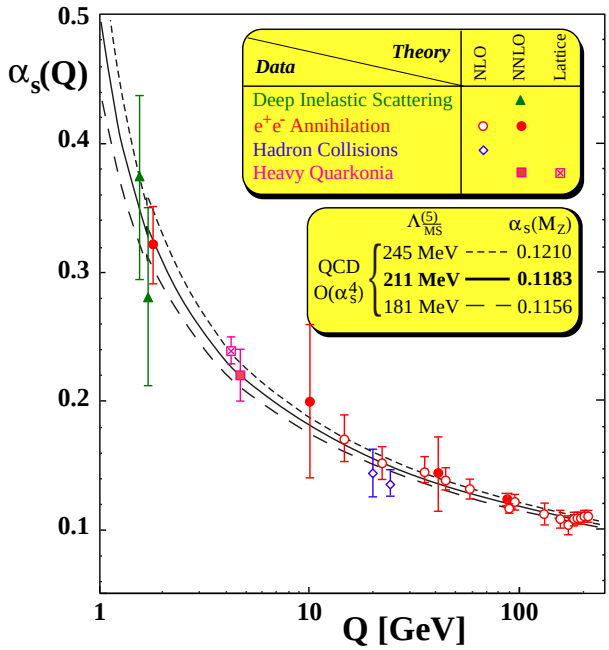

Figure 1.1: The α_{QCD} coupling constant [20].

Another approach can be done, in order to estimate the evolution of the coupling

constant by introducing directly in the definition of the coupling a new parameter Λ_{QCD} [21] which sets the scale to large coupling constant where the physics becomes nonperturbative. The Λ_{QCD} value can be determined experimentally and it is on the order of 200 MeV:

$$\alpha_s(Q^2) = \frac{12\pi}{(33 - 2n_f)\ln(\frac{Q}{\Lambda_{QCD}})^2} \tag{1.10}$$

It remains to solve the problem of formulating the QCD theory in a non-perturbative regime when the strong interaction coupling becomes hard for large distances between quarks (larger than 1 fm) or for small energy scale energy (less than 1 GeV). A solution is provided by the Lattice QCD method (see Section 1.2.5).

1.2.3 The quarks confinement

One of the success properties of QCD is the formation of color singlet objects. This feature is called the color confinement of quarks in hadrons. In the same way as the electric charges of the opposite sign suffer attraction, the color charge attracts quarks with different colors. The QCD explains, in particular, the formation of hadrons. The quarks behave almost as free partons inside the hadron [22, 23]. When the quarks move away from each other (the energy put into play decreases), more gluons are exchanged. These gluons themselves can interact with each other or a couple of virtual quark-antiquark new pairs. Beyond a typical distance of 1 fm ($10^{-15}m$), quarks are no longer spread freely and remain confined within hadrons. This phase of hadronization taken over the non-perturbative QCD regime is generally described by phenomenological models. In general, if the potential between two quarks is proportional to the distance between them, then the two quarks can never be separated. To illustrate this character, a classic parameterization [24, 25, 26] of inter-quarks potential is proposed in the equation:

$$V(r) = -\frac{4}{3}.\frac{\alpha_s}{r} + \sigma.r \tag{1.11}$$

The second term of this equation shows the Coulombian interaction for short distances, the confinement is represented by the last term where σ is called the string tension. One may try to separate the quarks by pulling them apart, then the restoring force of the linear potential between them grows sufficiently rapidly to prevent them from being separated. The interaction between the quarks gets stronger as the distance between them gets larger. The form of the potential results of these two terms is shown in figure (1.2) depending on the separation distance r. The potential between the two quarks becomes linear and is it growing to infinity with the inter-quarks distance.

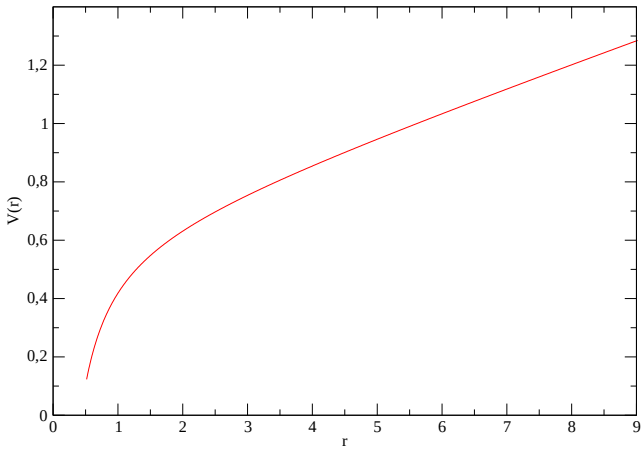

Figure 1.2: The potential between two quarks as function of the distance.

1.2.4 Deconfinement and the Quark Gluon Plasma

It is believed that the universe consisted of quarks and gluons transforming to hadronic matter just a few microseconds after the Big Bang [27, 28]. Theories also predict that it may still exist in the universe that we see today since the cores of dense neutron stars [29, 30, 31] and the supernova supply extreme astrophysical environments which favor the creation and the existence of this state.
Among the goals of current nuclear researches is the observation and characterization of this new state called Quark-Gluon Plasma (QGP) [32, 33] in which its building blocks (quarks and gluons) act in like free particles. The search for a such phase transition from the confined hadronic matter to the deconfined QGP matter is a fascinating subject to study the dynamics of this interface. The nature of the strong interaction has been described as in the case of the ordinary hadronic matter. However, it is crucial to be able to describe the behavior of the matter under conditions of temperature and density, particularly when one or both of these two quantities are extremely high [34, 35]. The challenge is to understand the substance of the Universe during its first moments, but also of existing forms such as inside the compact stars formed by the gravitational collapse of the supernovae nucleus.
We can talk about phase transition when certain properties of nuclear matter undergo a radical change for that reason the system can be well described using statistical mechanics description which provides global variables and other conserved

quantities. The grand canonical ensemble is therefore used to describe the whole system allowing the variation of the particles number. The parameters of the control are then the temperature T, the volume V and the chemical potential μ. The latter represents the necessary energy to provide to the system in order to add a quark. Generally the diagram of phases depending on the temperature (T) and potential chemical baryonic, as shown in the figure (1.3) [36].

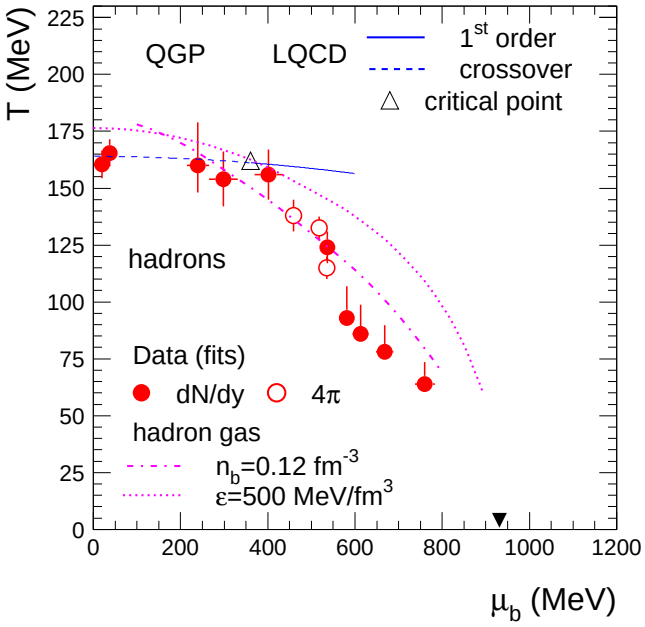

Figure 1.3: The QCD phase transition diagram of the hadronic matter [36].

By increasing T or μ_b, a phase transition is possible to occur. The evolution of the universe can be traced from its earliest moments, where the temperature was well above T_c and at low chemical potential. The bottom left of this diagram corresponds to low temperature and low baryonic potential, the behavior of QCD thermodynamics can be described in terms of hadron gas (states composed of related quarks and gluons): if we increase the temperature of the system, this state cannot exist as it is. There is a small area where this matter is undergoing a transition considered as cross over, from which the degrees of freedom are not the hadrons but quarks and gluons themselves. The high μ and small T on the right of the diagram, corresponds to a region accessible by compressing the system. This state of matter

is a matter of quarks that can be found in the hearts of neutron stars [37, 38].

1.2.5 The Lattice QCD

At large distances (i.e. small scales) it becomes impossible to use the perturbative theory to achieve results. Indeed, the interactions between quarks and gluons are too strong and perturbative approach can not work. In particular, the QGP can not really be considered as a gas of particles without interaction. To take in account these interactions we should use the QCD to model all the interactions existing in the system. In this framework, Lattice simulations of QCD thermodynamics have made significant progress during the last decade.
The method of Lattice QCD allows a statistical approach of the strong interaction for complex systems. It gives access to the thermodynamic characteristics of a quarks and gluons system at the equilibrium. The rapid rise in computational power and implementation of better algorithms authorize the simulation of the behavior of matter by the QCD equations, which describes the strong interaction suffered by the quarks and gluons. The whole technic is based on the discretization of space-time coordinates on a finite domain [39, 40]. The particles involved in the simulation are located on the nodes of the Lattice. An introduction to the used lattice QCD methods and its technical details could be founded in [41].

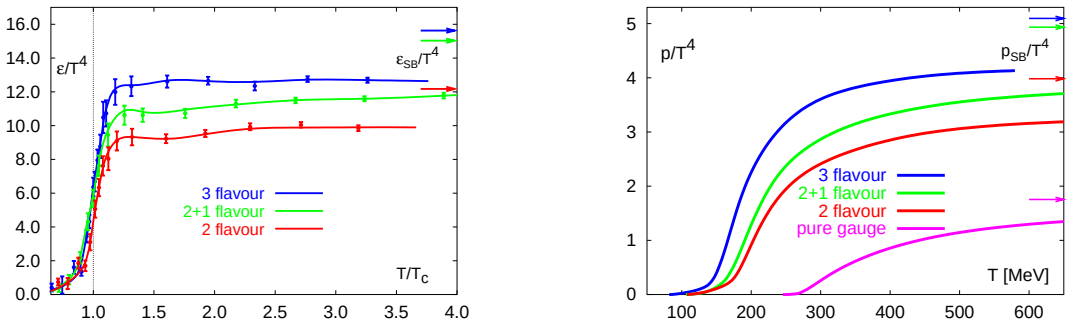

Figure 1.4: The lattice QCD energy density (left) and pressure (right) as function of temperature for $n_f = 0, 2$ and 3 light quarks as well as two light flavors (u and d) and one heavy flavor (s) [42].

Initially, the developments were limited to $\mu_b = 0$ and they can calculate the evolution of pressure depending on the temperature. Figure (1.4) shows the evolution predictions of the energy density (left) and pressure (right) depending on the temperature. This method of studying deconfinement take into account 3 assumptions: two light quarks (u and d), three light quarks (u, d or s), or two light flavors

Name	Mode	Beam	$E\ (AGeV)$	$\sqrt{(}s_{NN})\ (GeV)$	$\epsilon(GeV/fm^3)$
SIS	fixed target	^{238}U	1	1.4	0.5
AGS	fixed target	^{208}Pb	12	4.9	1.0
SPS	fixed target	^{208}Pb	158	17.3	3.5
RHIC	collider	^{197}Au	100	200	5
LHC	collider	^{208}Pb	2750	5500	$15-60$

Table 1.1: The main characteristics of the ultra-relativistic accelerators used in the high energy heavy ion physics and theirs achieved energy densities.

(u and d) and a heavy flavor(s). A transition from the hadronic phase to partonic phase is clearly visible. The energy density undergoes a rapid change near a critical temperature T_c, enhanced by almost an order of magnitude, as indicated in figure (1.4). The temperature T_C depends on the number of flavors (n_f) considered: $T_c =$ 175 MeV for two light quarks (2 flavors), $T_c = 155$ MeV for three light quarks (3 flavors) [42]. The reported error is the statistical error only and therefore it does not takes into account the engendered systematical error by the discretization of the lattice. The Lattice QCD confirms the sharp increase of the number of degrees of freedom of the system to the temperature of the phase transition. This rapid change is an indication that the fundamental degrees of freedom are different above and below the critical temperature.

1.3 Ultra relativistic heavy ion collisions

1.3.1 Accelerators

The goal of research in ultra relativistic heavy ion collisions is studying the possible formation of a new state of nuclear matter called Quark and Gluon Plasma (QGP). It is believed that this state of matter can be reached at ultra relativistic heavy ion collisions where sufficient energy density and temperature is achieved. Under these circumstances, the nuclear material undergoes a deconfined phase transition leading to the QGP formation. To simulate such extreme conditions here on earth, Ultra relativistic heavy ion collisions between two nuclei were performed and an experimental campaign has been therefore launched since 1986 to prove its existence and to study it. The program of this campaign used to study the dense matter. The different machines used for this subject are presented in Table 1.1: the Alternating Gradient Synchrotron (AGS), the Relativistic Heavy Ion Collider (RHIC) at the Brookhaven National Laboratory (BNL), the Super Proton Synchrotron (SPS) and the future Linear Hadron Collider (LHC) at CERN.

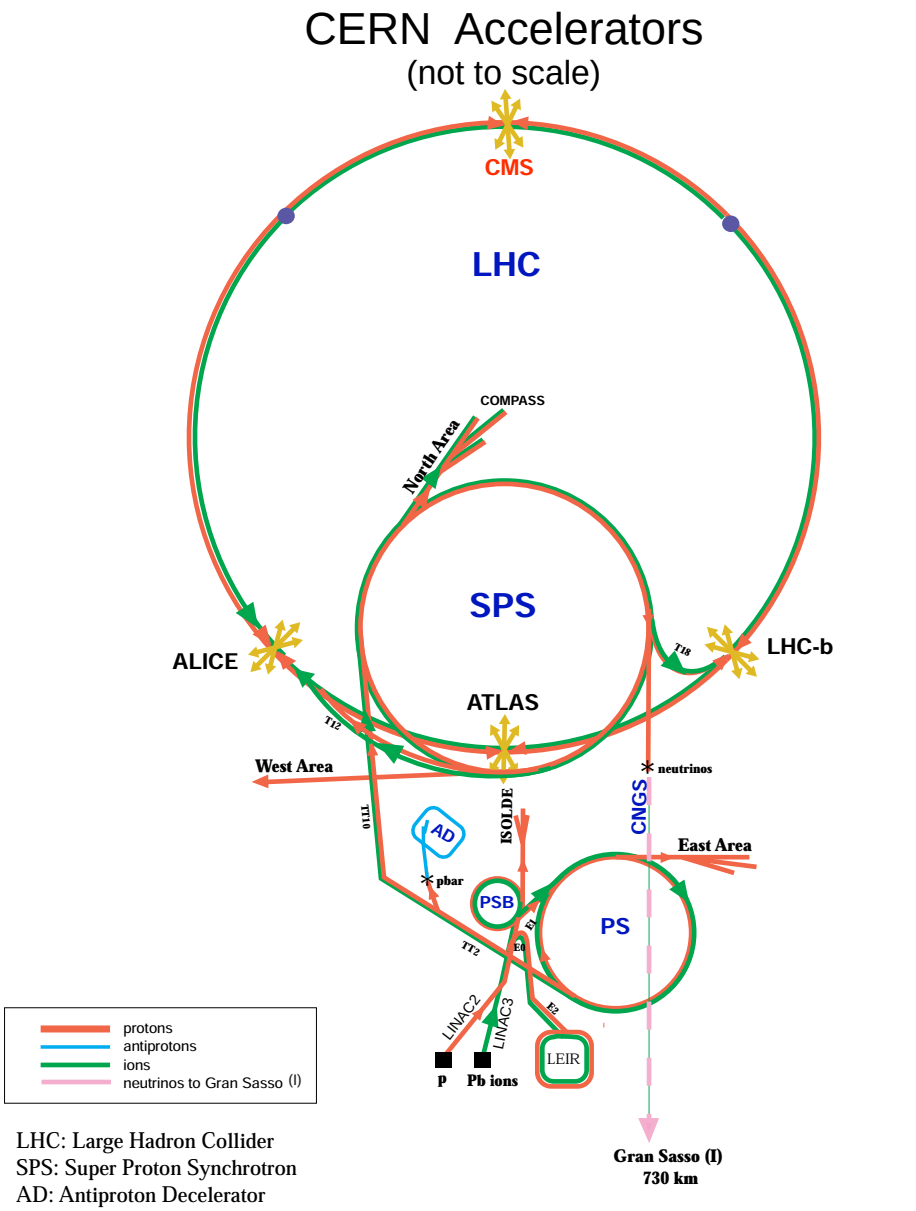

Figure 1.5: The accelerator complex at CERN.

The main objective of these accelerators is to draw a detailed description for the path of the universe in the opposite direction by raising the temperature. The future of the discipline lies at the LHC back at CERN with a rise in energy by a factor of almost thirty.
The QGP state will be examined by the ALICE detector which is the only experiment optimized for the heavy ion collisions to study the physics of the strongly interacting matter and the quark gluon plasma in nucleus-nucleus collisions [43]. It will reach center of mass energies of about 14 TeV for protons, and 5.5 TeV for nuclei, which is much higher than the previous experiments. ALICE is built around the largest TPC in the world [44]. In the future, it would be possible to probe deeper into matter than ever before and increasing our knowledge of how the universe began.

1.3.2 The evolution of the QGP: Scenario of Bjorken

To reach the Quark-Gluons Plasma, extreme scenarios must be re-created by colliding heavy ions with velocities close to the speed of light: enormous temperatures, pressure and densities of those first few microseconds. The framework of the space-time evolution of ultra-relativistic heavy ion collisions is defined qualitatively and even quantitatively in terms of the reached energy density. This scenario of evolution was proposed by Bjorken in 1983 [45] and is represented in figure (1.6).

The system presents a succession of several phases. In the pre-equilibrium phase, about typical time of T_0 of 1 fm/c, the system is thermalized and led to the formation of QGP in total lifetime of the order of 5 to 7 fm/c. The quark-gluon plasma state created in collisions will expand and cool down very rapidly, $t = 10^{-23}$s till reaching the critical temperature T_c transition. That means that the quarks are grouped into hadrons and the cooling system will be gradually transformed into a hadronic phase. The hadronic matter keeps expanding and cooling off.
The hadrons undergo elastic and inelastic collisions that change the production rate and the momentum spectrum of different particles. They finally stopped when the system expansion reach its limit. This ultimate step is called chemical freeze-out where eventually all inelastic interactions are stopped and the particles species are no longer changed by collisions but only by decays. The nature of particles and their energies are then frozen. This will disintegrate to provide stable particles that eventually end up their course in the detector.
Such scenario raises some questions about the possibilities to probe the partonic phase since the short lifespan of the QGP for a few fm make it more difficult to be observed directly by the detectors. However the manifestation of the QGP probes at various moments during the evolution is the only way to find its evidence by the remnants of the collisions.

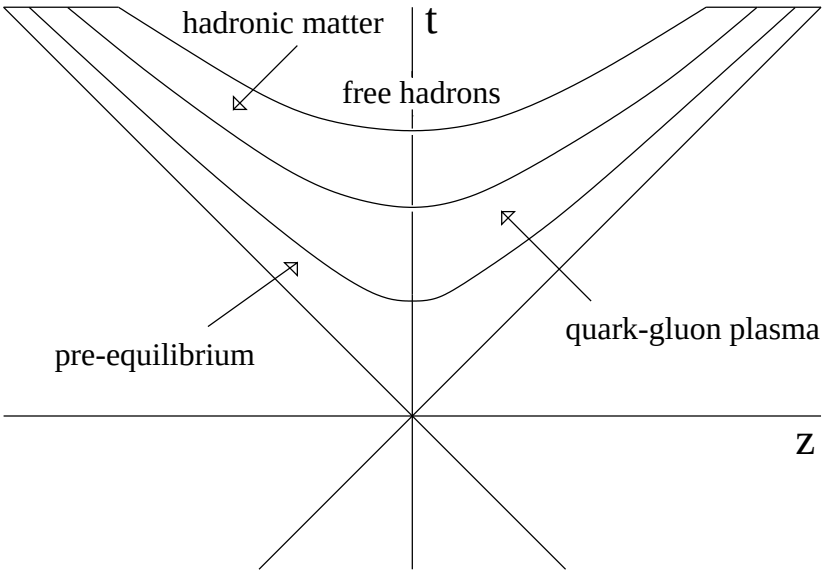

Figure 1.6: The evolution of Ultra-Relativistic Heavy Ion Collisions [46]. The different stages of the space-time evolution are shown starting from the non-equilibrium state to the final state as free hadrons.

1.3.3 The Geometry of the collision

A nucleus-nucleus collision at very high energy produces a large number of hadrons near the center of mass. The attained energy density during the collision depends on the energy of the incident nucleus, their longitudinal size (atomic mass) and the fireball volume that is big enough to explore the QGP. The corresponding Lorentz contraction is important since it is already $\gamma = 10$ for the SPS and it makes also sure that the deformation is in the direction of movement. The centrality of the collision or the degree of overlap of two nuclei at the collision time is usually given as a percentage of the total cross section. We might define then from these measurements an important variable at this stage: the impact parameter b, which gives the distance between the axes of the two nuclei. This description can be illustrated by figures (1.7).

Here we describe the case of the most central collisions as they permit to get the higher energy density where the system is essentially in the form of a hadrons gas. When a collision occurs at low impact parameter b, the measured number of particles will be big, and the collision will be central. In contrast, a collision at high impact parameter is peripheral. One can underline the principal observables which characterize the dynamic of the collision that are expressed in term of rapidity as:

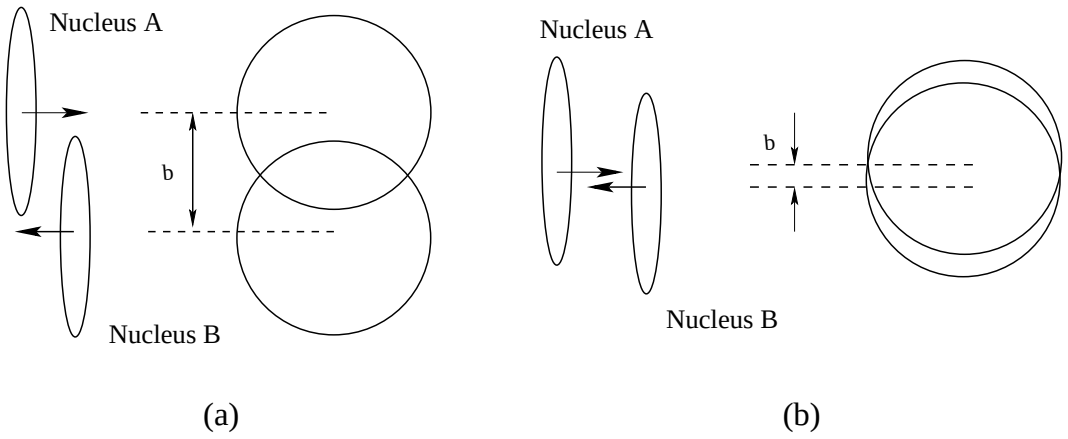

Figure 1.7: Schematic view of high energy particles scattering. The geometry of the collision describes two effects. In the left side, the impact parameter b is large, thereby the recovery zone is elliptic whereas in the right side the b factor is small and the recovery zone is nearly circular.

$$y = \frac{1}{2} \ln \frac{E + p_L}{E - p_L} \tag{1.12}$$

where E is the total energy of the particle and P_L is its longitudinal momentum. When the energy density is much greater than the mass of the particle, the preference then is to use the pseudo-rapidity variable:

$$\eta = \frac{1}{2} \ln \frac{|p| + p_L}{|p| - p_L} = -\ln(\tan \theta_0) \tag{1.13}$$

where θ is the angle between the particle momentum and the beam axis. The initial energy density E_{Bj} produced during the collisions can then be calculated using the formula (1.14) [45]:

$$E_{Bj} = \frac{1}{A_T \tau_0} . \frac{dE_t}{dy} \tag{1.14}$$

This equation takes into account the overlapping transverse surface between the nucleons A_T (depends on B), τ_0 the proper time of the partons thermalization (estimated at around $1 fm/c$) and the measurement of the total transverse energy, for such particle i emitted by an angle θ_i, is defined by:

$$E_T = \sum_{i=1} E_i . \sin(\theta) \tag{1.15}$$

The energy densities at CERN-SPS energy is on the average of 3.9 GeV/fm^3. From the equation (1.14), one can conclude that the more the energy density is high the more we have the possibility to create the QGP state.

1.3.4 The experimental observations of the QGP

The QGP scenario described previously raises some questions about the possibilities to probe the partonic phase. Due to the very short lifetime of the plasma, how to ensure that the observed gap is really deconfined phase ? In reasonable manner, the detection of a set of signatures might be really a clear way to discard any ambiguity [47]. The predicted signatures for the QGP can be roughly divided into 3 categories: electromagnetic signatures [48, 49] which are based on the detection of dileptons and photons, signatures associated with the measurement of the hadron production, and the signature coming from the deconfined phase which enhance the production of strange quarks and the J/ψ suppression [50]. Among these various probes, photons and dileptons are known to be advantageous as these signals examine the entire volume of the plasma because they do not interact with the medium. We will concentrate only on the electromagnetic signatures. The reader is referred to [51] [52] for more detailed review about the other probes.

1.3.5 Electromagnetic probes

Together with dileptons, photons constitute electromagnetic probes which are believed to reveal the history of the evolution of the plasma. Dileptons are produced in a QGP phase by quark-antiquark annihilation, which is governed by the thermal distribution of quarks and antiquarks in the plasma. The examination of photons provides a tool to study the different stages of a heavy ion collision. They are believed to originate from quark-antiquark annihilation ($q\bar{q} \rightarrow g\gamma$) and the QCD Compton scattering ($q(\bar{q})g \rightarrow q(\bar{q})\gamma$) processes and as well as from the photon radiation with bremsstrahlung processes ($q\bar{q} \rightarrow q\bar{q}\gamma$) at higher order of $\alpha_s^2\alpha$ [53, 54]. The Feymann diagrams of these three processes are illustrated in figure (1.8).

Consequently, the direct photons [55] which do not interact with the medium have various origins with rather different sources. They are created within three subprocess described previously which dominate the photons emission from the fireball. They can be obtained by extracting the decay photons where in this case one have to deal with formidable background problems because of the hadronic decays into photons most notably the $\pi^0 \longrightarrow \gamma\gamma$ and the $\eta \longrightarrow \gamma\gamma$. The direct photons are frequently divided into two-prong. The first type consists of photons originating from

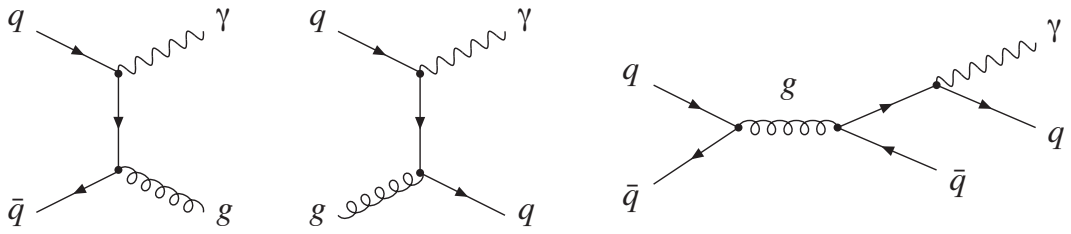

Figure 1.8: Feynman diagrams of the main production processes for direct photons.

the early hard proccess in the dense medium are called *prompt photons*. The second type stands for the photons radiated from thermalized matter the quark-gluon plasma phase, they are named *thermal photons* [56]. They can be produced during the whole history of the evolution of QGP and Hadron gas.

To my self I seem to have been only like a boy playing on the seashore, and diverting myself now and then finding a smoother pebble or a prettier shell than ordinary,whilst the great ocean of truth lay all undiscovered before me.

Sir Isaac Newton

2 The CERES Experiment

2.1 Experimental setup overview

The CERES/NA45 (Cherenkov Ring Electron Spectrometer) is the only experiment at the CERN Super Proton Synchroton (SPS) dedicated to the study of e^+e^- pairs produced in nucleon-nucleus and nucleus-nucleus collisions in a fixed target geometry in the low mass range up to 1 GeV/c^2 [57, 58, 59, 60]. It is axially symmetric around the beam and it has 2π azimuthal coverage. It was set-up in 1990, went into service in 1991 and started to take data in 1992.
The original setup included two Silicon Drift Detectors (SDD), two Ring Imaging CHerenkov Detectors (RICH) [61] for the electron identification. It was upgraded twice, once from 1994 to 1995 with an additional multiwire proportional chamber with pad readout (the Pad Chamber) to improve the momentum resolution and to allow operation in the environment of the multiplicity of lead on gold collisions [62]. A second time it was upgraded with an additional magnet and a new powerful tracking detector a cylindrical Time Projection Chamber (TPC) with radial drift field which replaced the pad chamber [63, 64, 65, 66]. This was done to improve the mass resolution.

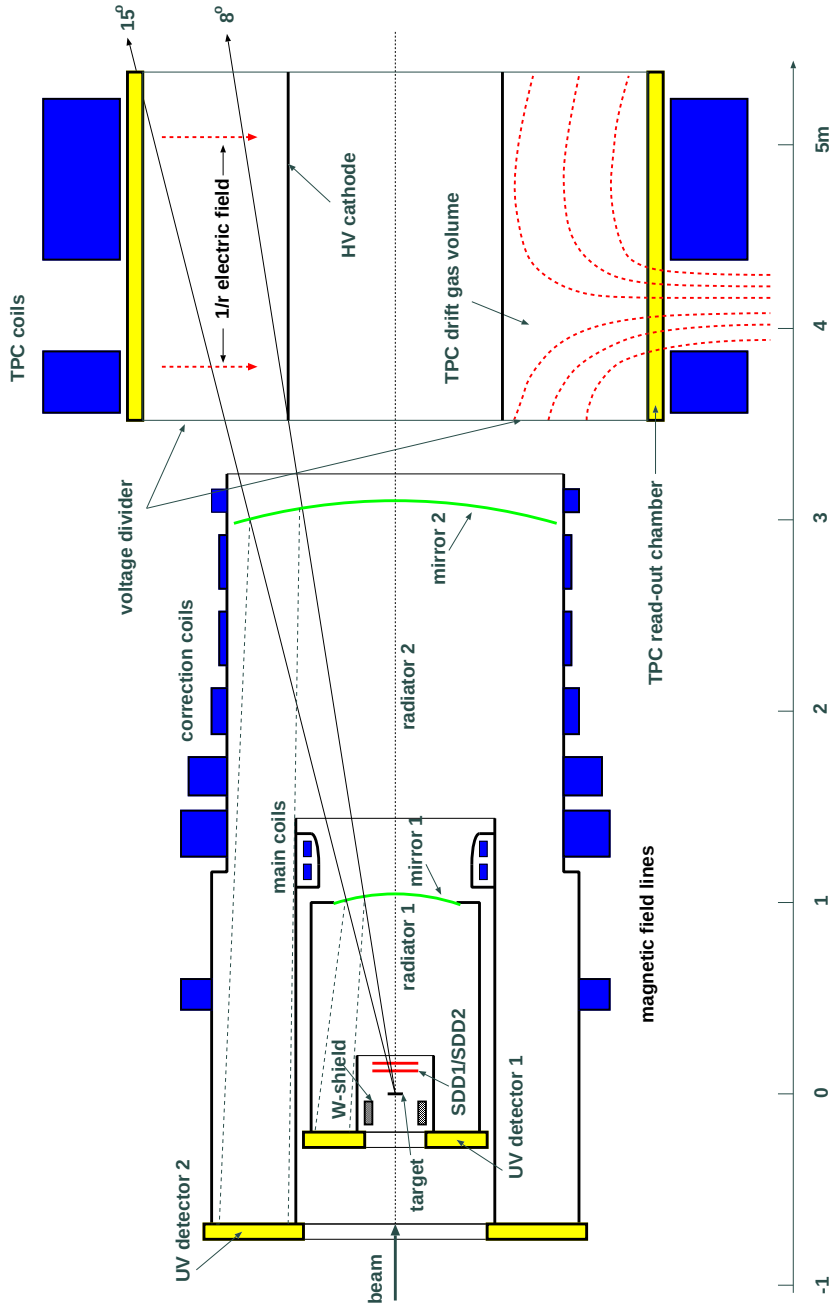

Figure 2.1: The CERES experimental setup after the upgrade with the Time Projection Chamber.

Moreover, the dE/dx signal in the TPC provides also electron identification in addition to the identification by the RICH detectors. The new experimental setup, with the TPC reaches a mass resolution $\delta m/m \sim 3.8\%$ [67, 68] at the ϕ-peak in the electron decay channel. The addition of the TPC opens the possibility to study hadronic observables [69, 64]. The upgraded experiment is shown in figure (2.1). The following sections of this chapter describe the main features of the subdetectors. They have a common acceptance in the polar range $8° < \theta < 14°$ which corresponds to pseudorapidity range of $2.1 < \eta < 2.65$ at full azimuthal coverage.

2.2 The target region

CERES used during the last data taking in the year 2000 a target system consisting of 13 fixed gold disks of $25\mu m$ thickness, and $600\mu m$ diameter, spaced uniformly by 1.98 mm in the beam direction. The distance between the disks was chosen such that particles coming from a collision in a given target disc and falling into the spectrometer acceptance do not hit any other disc. The reason behind this geometry is to minimize the conversion of the $\gamma's$ into e^+e^- pairs. A tungsten shield is installed around the target to absorb particles emitted backwards in order to protect the UV-counters of RICH detectors from long background signals.

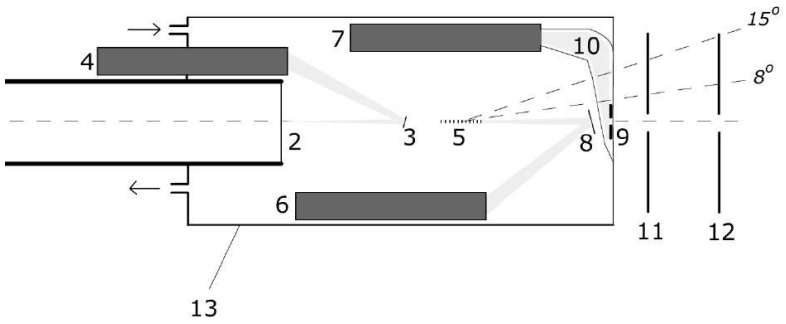

Figure 2.2: The Target area: 1 - The vacuum pipe, 2 - The entrance window, 3 - BC2 4 - BC2's PMT, 5 - Au target, 6 - BC3's PMT, 7 - MC's PMT, 8 - BC3, 9 - MC scintillator, 10 - Al-mylar light guide, 11 - SiDC1(down), 11 - SiDC2(up), 13 - Gas radiator.

2.3 The trigger system

Triggers are essential to optimize the quality and quantity of the physics events and to keep the same time, the background events very low. The CERES experiment trigger system starts the read-out sequence of the detectors if the occurrence of a collision has been detected. This is done with the system of beam/trigger detectors shown in figure (2.3). The **B**eam **C**ounters (BC1, BC2 and BC3) are the Cherenkov-counters with air as radiator. These detectors are used to detect collisions happened between projectile and target nuclei.

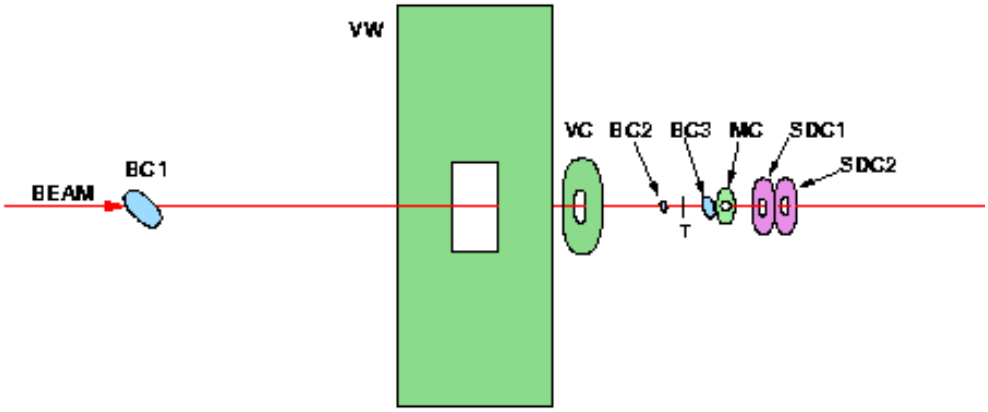

Figure 2.3: Schematic view of trigger detectors.

The beam trigger (BEAM) is defined by the coincidence of the two beam counters (BC1 and BC2) located in 60 mm and 40 mm in front of the target respectively:

$$T_{BEAM} = BC1.BC2 \tag{2.1}$$

The minimum bias trigger (MinB) is defined as beam and no signal in the beam counter (BC3) which is located 69 mm downstream the target system.

$$T_{MinB} = BC1 \times BC2 \times \overline{BC3} \tag{2.2}$$

To select the centrality of the collisions based on charged particle multiplicity a Multiplicity Counter (MC) located 77 mm downstream the target was used. Its output signal is approximately proportional to the number of charged particles passing through it. The central collision trigger is defined as:

$$T_{central} = T_{MinB}.MC \tag{2.3}$$

The veto detectors VW and VC are plastic scintillators. They are used to reject interactions which happened before the target. The main trigger detectors BC2, BC3 and MC are located in the target area followed by the Silicon Drift Detectors (SDD's), they form a vertex telescope which is a central part of the event and vertex reconstruction.

2.4 The Silicon Drift Detectors

The doublet Silicon Drift Detectors(SDD's) are placed approximately 10 cm behind the target. Each of them consists of a circular 4-inch silicon wafer with a thickness of 250 μm which has a central hole of about 6 mm diameter for the passage of the beam. The sensitive area covers the region between the radii 4.5 mm and 42 mm with full azimuthal acceptance and cover the pseudorapidity range [1.6,3.4]. The 4" SDD used in CERES is designed using the principle of the sideward dileption [70]. A charged particle traversing the detector creates a cloud of electron-hole pairs which then drifts along radially in the electric field towards the outer rim of the silicon wafer (figure (2.4)) where they are collected by an array of 360 anodes distributed equally over its surface and connected with a read-out chain.

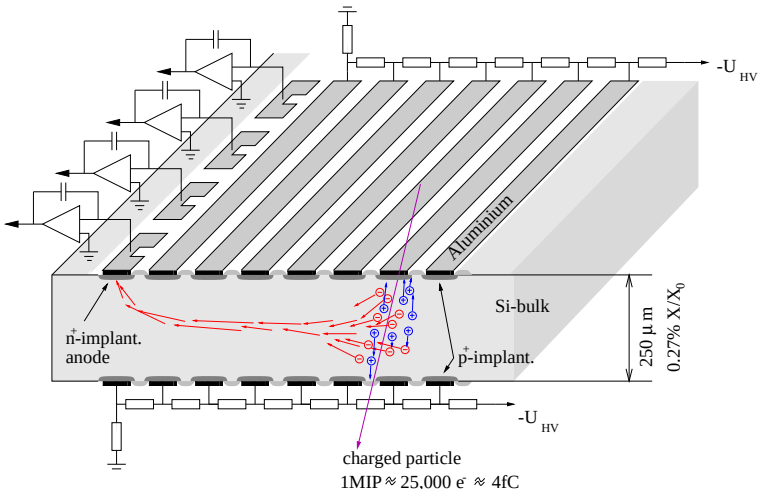

Figure 2.4: Working principle of the Silicon Detectors.

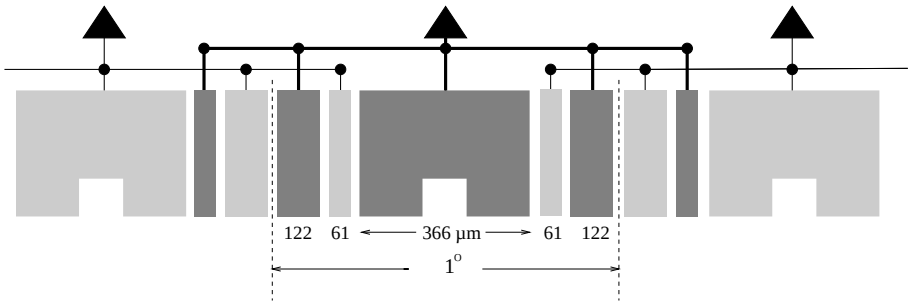

Figure 2.5: Detailed view of the SDD anode structure.

An Schematic view of the anode structure used in the SDD detectors is shown in figure (2.5) where its design guarantees optimal charge sharing and provides an accurate azimuthal position resolution [71]. The charge of one hit is detected by several anodes and a more exact position measurement can be done by calculating the center of gravity of this distribution. When a charged particle passed through the detector plane, the radial coordinate r (or the polar angle θ) of a point is calculated knowing the drift velocity and measuring the drift time with a FADC (Flash Analogue to Digital Counters) with sampling frequency of 50 MHz. An example of an event in the SiDC detector is shown in figure (2.6).

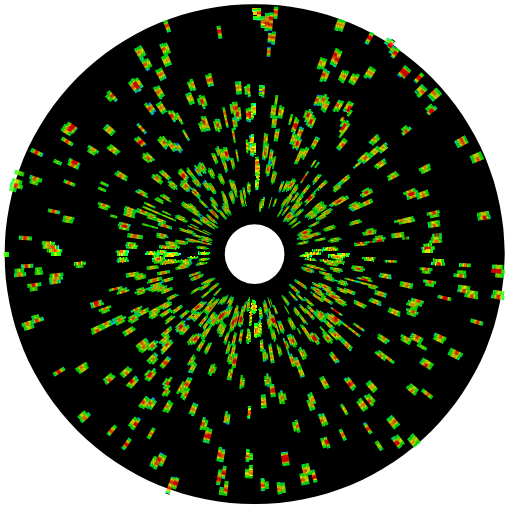

Figure 2.6: A central $Pb - Au$ event in one of the two SiDC detectors.

The two SDD's detectors provide a very precise vertex reconstruction, determine the pseudorapidity density of charged particles $dN/d\eta$, the coordinates of hundreds charged particles with high spatial resolution and interaction rate in addition to the suppression of e^+e^- pairs coming from conversions. This feature of the SDD is extremely necessary for the rejection of photon conversions before the RICH2 when studying low mass dilepton pairs. In this analysis the only information used from the SDD detectors is the reconstructed position of the event vertex for each event.

2.5 The RICH Detectors

The Ring Imaging Cherenkov Detectors (RICH) are used to identify the electrons and to measure the particle velocity β. They are the heart of the electron spectrometer. The RICH detectors were invented by J.Séguinot and T.Ypsilantis [72]. If the momentum of the particle is known the mass can be determined. Particles pass through radiator and the radiated photons are collected by a position-sensitive photon detector by focusing mirror. The simplest method to discriminate particles with Cherenkov radiation utilizes the existence of a threshold for radiation; thus providing a signal whenever β is above the threshold $\beta = 1/n$. According to electromagnetism, a charged particle emits photons in a medium when it moves faster than the speed of light in that medium (Cherenkov radiation). The speed of light in a medium with reflecting index n is given by:

$$v = \frac{c}{n} \tag{2.4}$$

where c is the velocity of light in a vacuum. When the velocity of charged particle exceeds the threshold, Cherenkov lights are emitted under a constant angle θ_c with respect to the particle trajectory.

$$\theta_c = acos(\frac{1}{n.\beta}) \tag{2.5}$$

From the asymptotic angle θ_c the Lorentz threshold for a charged particle to radiate can be expressed as:

$$\gamma_{th} = \frac{1}{\sqrt{1 - \frac{1}{n^2}}} \tag{2.6}$$

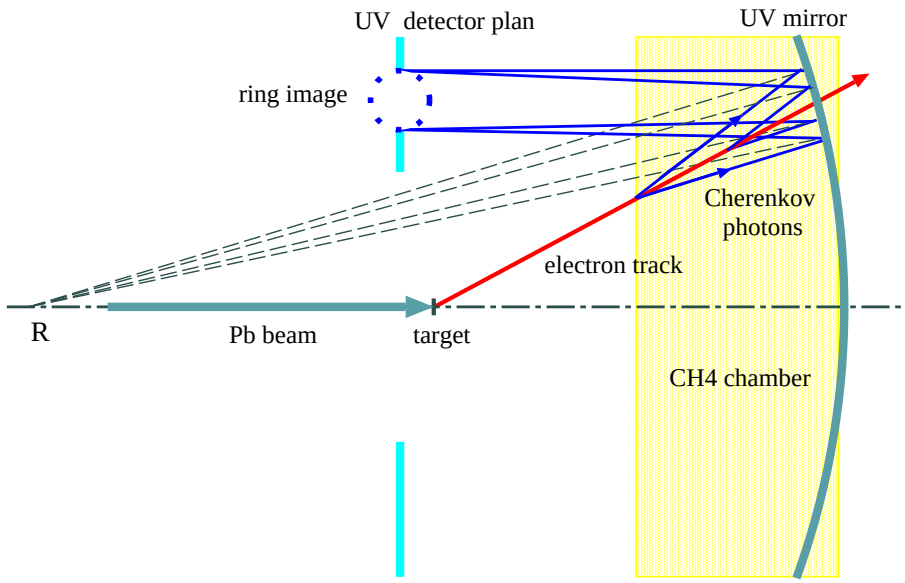

Figure 2.7: The Principle operation of the CERES RICH detector

The relativistic particles pass through a radiator, and the emitted photons are optically focused by a spherical mirror onto a position-sensitive photon detector, on which Cherenkov photons are detected on a ring with radius:

$$R = R_{\infty}\sqrt{\left(1 - (\frac{m.\gamma_{th}}{p})^2\right)} \tag{2.7}$$

where R_{∞} is the the asymptotic radius of particles with $\gamma >> \gamma_{th}$.
As the ring radius, the number of the Cherenkov photons depends also on the particle momentum and its mass:

$$N = N_{\infty}\left[1 - (\frac{m.\gamma_{th}}{p})^2\right] \tag{2.8}$$

where N_{∞} is the asymptotic number of the reconstructed photons with $\gamma >> \gamma_{th}$.
The RICH detectors in the CERES experiment operated with CH_4 at atmospheric pressure as radiator gas [61]. An illustrated view of the CERES RICH detector principle of operation is shown in figure (2.7).
The CH_4-gas has $\gamma_{th} \approx 32$ and very high transmission in the U-V region. Therefore, only electrons and positrons emit Cherenkov light. Charged pions need a momentum of 4.5 GeV in order to reach the threshold. Whereas most of hadrons 95(%) pass without creating any signal. The RICH detectors are therefore practically

hadron blind. In order to minimize the number of the converted photons in the spectrometer and to reduce the loss of momentum resolution due to multiple scattering, the amount of material within the acceptance is kept as small as possible. For this reason, the RICH1 mirror is based on a thin carbon fiber structure with 1 mm thickness ($0.4\%X_0$). The RICH2 mirror is built of 6 mm glass with radiation length of $X/X_0 = 4.5$ % at comparable U-V reflectivity [61, 73]. The UV detectors used for position sensitive measurement of the photons are gas counters consisting of three amplification stages, two **P**arallel-**P**late **A**vanlanche **C**hambers (PPAC) and a **M**ulti-**W**ire **P**ropotional **D**etector (MWPD), with a gas composition of 94% He and 6% CH_4 and saturated vapor pressure of TMAE (**T**etrakis-di-**M**ethyl-**A**mino-**E**htylen). The incoming photons are converted into electrons by adding TMAE as a photo-sensitive agent. In order to achieve a sufficient partial pressure, the TMAE is heated to $40°C$. For the purpose of protection from gas condensation and temperature gradients the whole spectrometer is operated at $50°C$. The produced ion cloud in the last step induces a signal on a pad plan of 53800 pads in RICH1 and 48400 pads in RICH2. The pad sizes are 2.7×2.7 and 7.6×7.6 mm^2 respectively which corresponds to a subtended solid angle of 2 mrad per pad in both cases.
In this analysis, the information provided by the RICH detectors is not used. However, the RICH2 mirror is an essential part of this work as with its $4.5\%X_0$ it is the main photon converter in the experiment.

2.6 The CERES Time Projection Chamber

Generally a TPC comprises a cylinder filled with gas (typically a mixture of argon and methane). In conventional TPC's uniform electric and magnetic fields are applied parallel to the axis of the cylinder. Charged particles created in the collisions pass through the chamber and ionize the chamber gas along the trajectories. Electrons produced by the ionization drift toward the end cap of the TPC due to the electric field. The electron trajectories follow the magnetic field in tiny spirals. On each end cap, the drifting electrons are amplified by a plane of anode wires, and signals are read out from small pads behind the anode wires. The TPC's are designed to provide a three-dimensional picture of all charged particles emitted in a large aperture surrounding the beam axis with a minimal disturbance to the original trajectories [74].
In contrast, the CERES TPC has a non-uniform electric and magnetic field that are not parallel to the axis of the cylinder (see next section).

2.6.1 Mechanical layout

The cylindrical geometry of the CERES TPC extends 2 m in length and 1.3 m in radius. In the center of the TPC there is a cylindrical electrode with radius of 48.6 cm. It is located at a distance of 3.8 m downstream the target. The TPC is composed of 16 Multi Wire Proportional readout Chambers installed in the outer circumference of the TPC ($r \approx 1.3m$). Each chamber has 20 readout planes along the beam axis with 48 pads each. This means each plane is with $16 \times 48 = 768$ readout channels. In total, 15360 (20 planes×48 pads×16 chambers) individual channels with 256 time bins allowing a three-dimensional reconstruction of particle tracks.

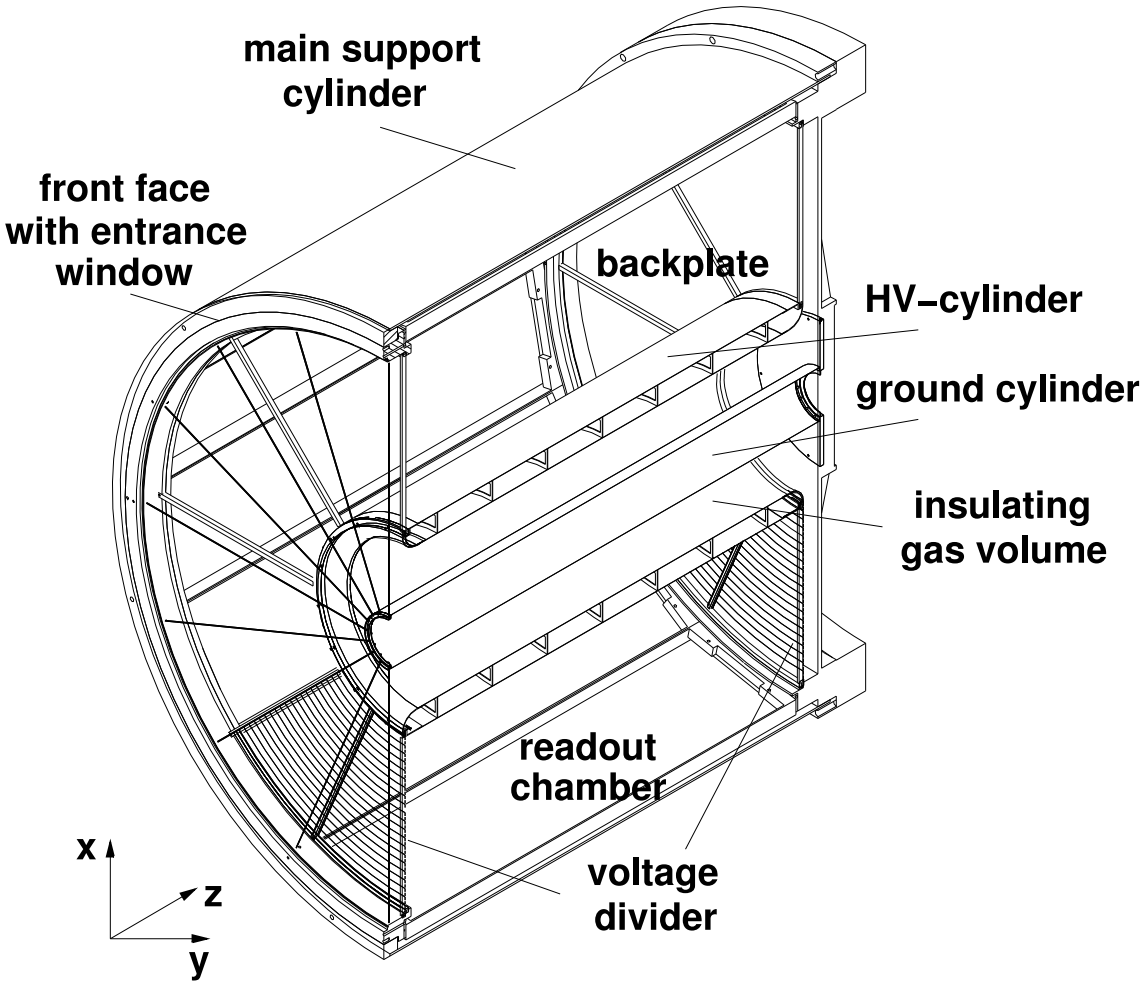

Figure 2.8: Perspective view of the CERES Time Projection Chamber.

A perspective view of CERES TPC is shown in figure (2.8) [75]. This special configuration is due to the fact that the new spectrometer system had to preserve the polar angle acceptance range which corresponds to $8° < \theta < 15°$ and the full azimuthal symmetry of the original CERES setup.

2.6.2 Electric field

The electric field in the CERES TPC is radial and it is define by the inner electrode which is an aluminum cylinder at a potential of $-30kV$ and the cathode wires of the read-out chambers at ground potential. In order to cancel rim effects of the electric field which should be parallel to $\overrightarrow{r}$, two voltage dividers consisting of 50 μm thick capton foils enclose the drift volume at the end caps of the TPC. The electric drift field strength is proportional to $1/r$. The dependence of the radial component as function of the radius and the azimuthal coordinate is illustrated in figure (2.9)

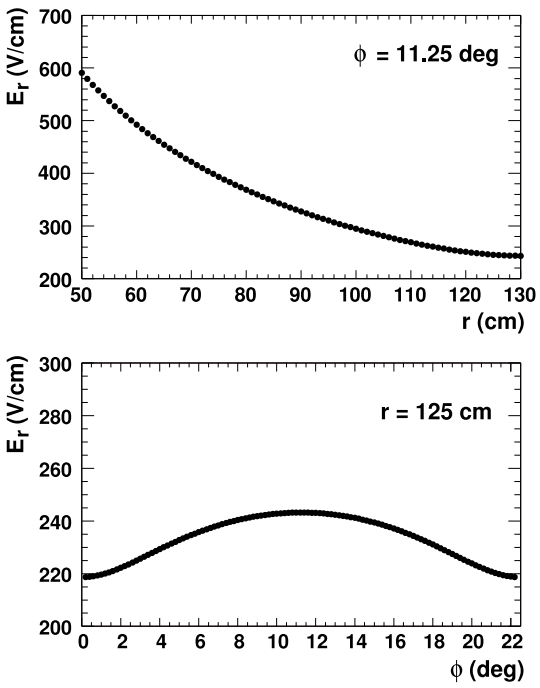

Figure 2.9: The electric dependence as function of the radius r (upper figure) and the azimuthal angle ϕ

2.6.3 Magnetic field

The TPC is operated in an inhomogeneous magnetic field, indicated in figure (2.1) by red dotted lines, generated by two warm coils with current flowing in opposite directions. The radial component of the magnetic field is maximal between the two coils and the deflection of charged particles is mainly in the azimuthal direction. The magnetic filed $\overrightarrow{B}$ has a radial B_r and longitudinal B_z components with strength up to $0.5T$. The field integral is 0.18 Tm at 8° and 0.38 Tm at $\theta = 15°$. Figure 2.10 shows the radial and longitudinal components of the magnetic field at the inner and the outer center end of the angular acceptance in θ.

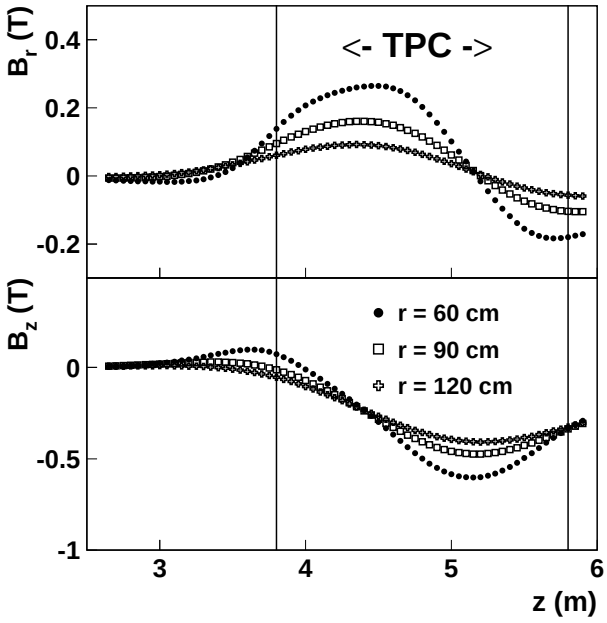

Figure 2.10: The magnetic field in the CERES TPC.

2.6.4 Counting gas and drift velocity

The ionization region or active volume of the TPC is 9 m^3 filled with 80%Ne and 20%CO_2 gas mixture. This composition was chosen as an optimum compromise between small diffusion, sufficient primary ionization, long radiation length and reasonable fast drift velocity [76].

The electric filed and the magnetic field in the CERES TPC are not constant along the drift path of the electrons. Therefore the drift velocity is not either. In the presence of a magnetic field $\overrightarrow{B}$ and an electric field $\overrightarrow{E}$ the drift velocity can be calculated using the following formula [76]:

$$\overrightarrow{v}_d = \frac{\mu}{1+(\omega\tau)^2}\left(\overrightarrow{E} + \omega\tau\frac{\overrightarrow{E}\times\overrightarrow{B}}{B} + (\omega\tau)^2\frac{(\overrightarrow{E}.\overrightarrow{B})\overrightarrow{B}}{B^2}\right) \tag{2.9}$$

In this equation: $\mu = e\tau/m$ is the mobility of the electrons, τ is the mean time between two collisions, and $\omega = \beta\mu$ is the cyclotron frequency. The mobility μ is a function of the electric field, the magnetic field and the gas composition. The angle between the drift velocity $\overrightarrow{v}_d$ and the electric field $\overrightarrow{E}$ is α_L the Lorentz angle given by:

$$\alpha_L = \widehat{(\overrightarrow{E}, v_D)} \tag{2.10}$$

Given a precise knowledge of $\mu, \overrightarrow{B}$ and $\overrightarrow{E}$ the actual drift path can be calculated. The drift velocities range from 0.7 cm/μs to 2.4 cm/μs with a maximal drift time of about 71 μs. The electrons drift along the path given by the drift velocity vector in equation (2.9) and reach one of the sixteen read-out chambers

2.6.5 Readout chambers

Before building the trace of a charged particle, a read-out stystem is needed for that purpose. The TPC is filled with a gas mixture (see previous section), which is ionized by the passage of a particle and the resulting charges are collected on the electrodes (pads) at the ends of the TPC cylinder. Signals originate from electrons that are freed when moving charged particles ionize the gas in the TPC.
At close distance to the anode wires, the electric field rises very sharply so drift electrons create ionized avalanches (electrons are multiply by factor 10^4) as they accelerate towards the anode wires where they are absorbed. Ions created in these avalanches produce image charge on the pad plan; the anode wires are close to the pad plane and are on 1.3 kV in potential.
The gating grid is furthest from the pad plane and it is operated at an offset voltage of -140 V. In the opened case, after an external trigger-signal, the electrons are allowed to pass through the gating grid which is switched to transparent mode at $U_{bias} = 0.V$. In the closed state, adjacent gating grid wires alternate from $-70V$ and $+70V$ then potentials differences set up electric fields between the wires that are perpendicular to the drift direction. By this way, stopping non-triggered electrons extends the life of the TPC by preventing unnecessary ionization from occurring in

the read-out chambers. The cross section of a read-out chamber with all the wire planes is shown in figure (2.11).

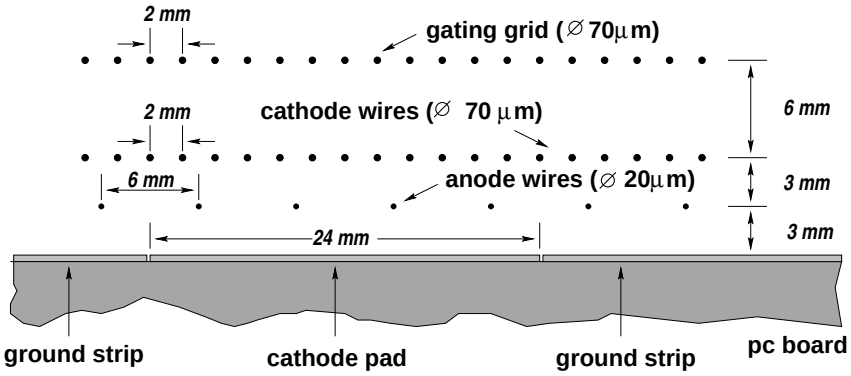

Figure 2.11: Cross section of the TPC readout chambers. The different wire planes are shown.

The experimental arrangement for the electric field close to the read-out chamber is calculated using the simulation package GARFILED [77]. The electric potential map performed for a read-out chambers with the gating grid during the open mode is drawn and shown in figure (2.12). The electric field lines helps to visualize the electric field near the charges. Field lines define the direction of the force that a positive charge experiences. The slowly drifting ions created near to the anode wires are neutralized in a very short time and captured by the cathode-pads.

The avalanche process produced close to the anode wires induces a signal in the chevron-type cathode pads [63]. In figure (2.13) we see the chevron structure which has been taken for the CERES TPC.
Measuring the drift time and knowing the drift velocity enables the reconstruction of the radial coordinates of the tracks. Due to the chevron geometric shape of the pads the charge cloud is reconstructed precisely and shared between the adjacent pads in the azimuthal direction. The analogue signals on the TPC pads are amplified, shaped and digitized in **F**ront **E**nd **E**lectronics (FEE).

2.7 TPC track reconstruction

The information provided by the TPC is the main component is this analysis. Therefore, we will describe in detail the different steps of the reconstruction. In this

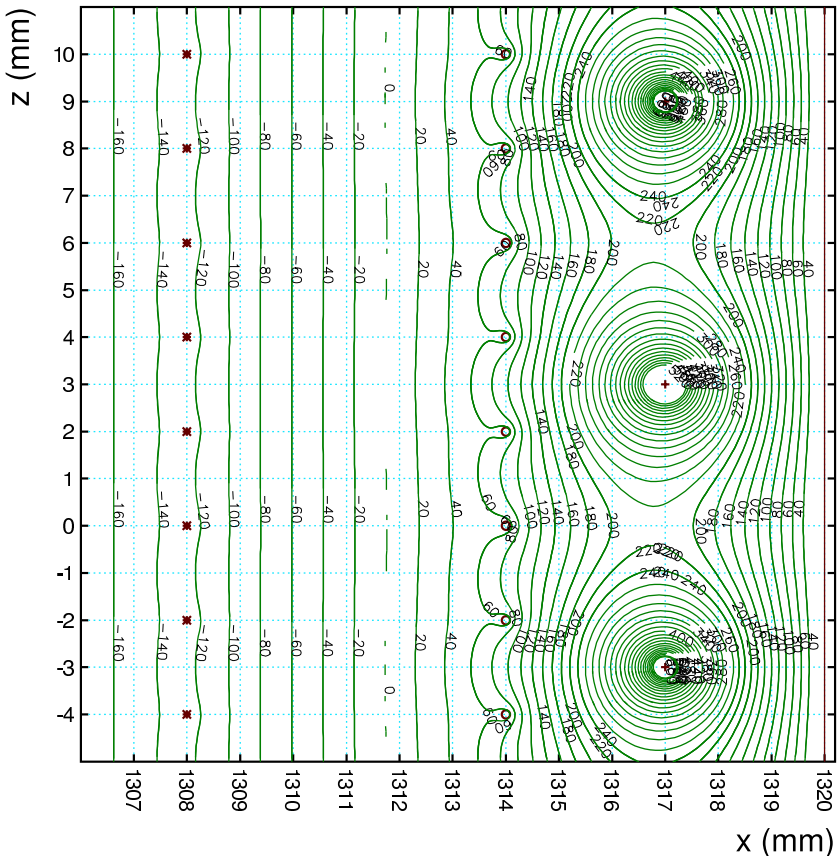

Figure 2.12: The electric potential map of the CERES TPC readout chambers simulated with the GARFIELD package.

section, we introduce firstly the algorithms (hit finding, track finding and track fitting) used to reconstruct the tracks in the radial drift TPC, then we describe the particle identification procedures by measuring its specific energy loss (dE/dx). A schematically event display of the TPC after track reconstruction is shown in figure (2.14).

2.7.1 TPC hit finding

The particle trajectories are reconstructed from hits in the tracking detectors using a tracking finding algorithm. As mentioned before (see Section 2.6.1) the CERES TPC has 20 planes with 768 pads along the azimuthal direction. The data of each channel consists of linear amplitude from 8-bit ADC in 256 time bins in radial direction. In total the $20 \times 768 \times 256 \approx 4$ million pixels make up the pixel grid.

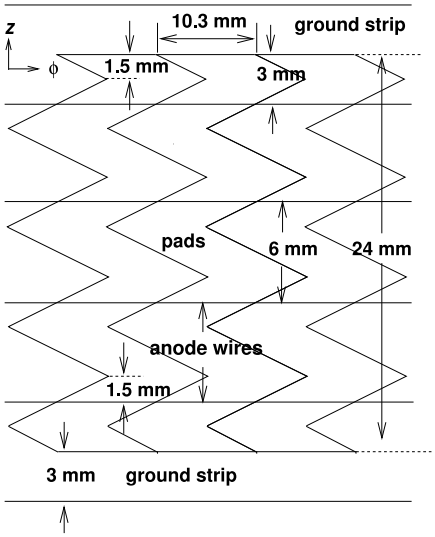

Figure 2.13: Scheme of the cathode pads. Four single cheveron pads of the cathode pads compose one readout chamber.

When a charged particle passes the counter gas of the detector the crossing point in each plane give a definition of the hit. It is described by a local maximum the adjacent pads and time bins [64, 78].
Hit coordinates are defined and encoded as pad amplitudes in two-dimensional array of pad versus time coordinates.

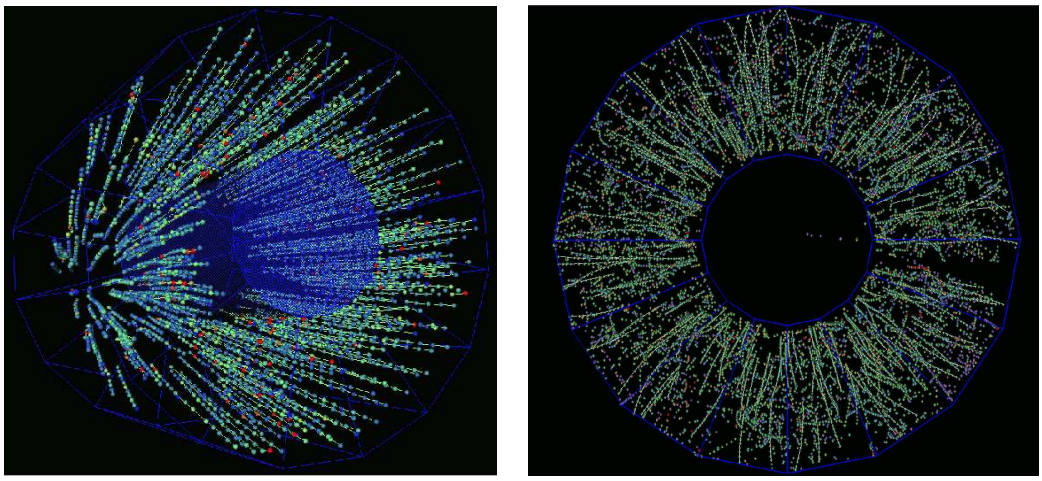

Figure 2.14: Schematic event display of the TPC.

The hit finding procedure starts to examine the pixel grid of the TPC in all the twenty planes searching the local maxima in the time direction for each pad. A local maximum corresponds to a hit only if the local maxima in time and pad directions are at the same location. The procedure is illustrated in figure (2.15).

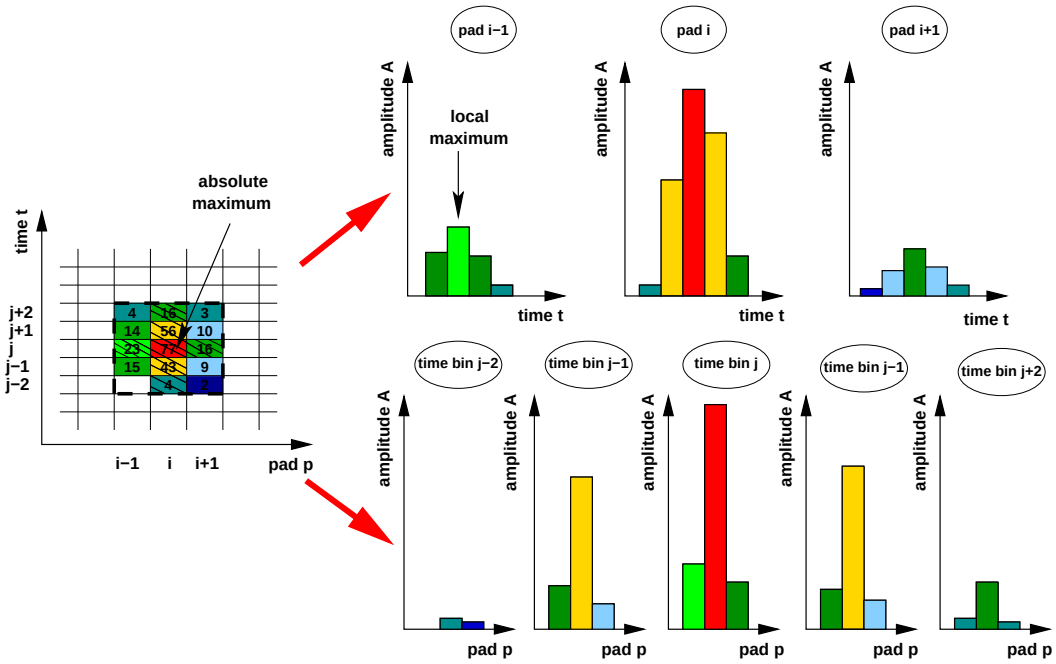

Figure 2.15: The TPC hit finding procedure.

An area of 3 pads ×5 time-bins around the local maximum is assigned to a hit. After finding all the maxima, the positions of all the individual hits are determined by calculating the center of gravity in pad and time directions for each of them. They are define as :

$$\overline{p} = \frac{\sum_i A_i \frac{A_{max}}{f_i} . p_i}{\sum_i A_i}$$

and

$$\overline{t} = \frac{\sum_i A_i \frac{A_{max}}{f_i} . t_i}{\sum_i A_i} \tag{2.11}$$

where the index i represent the pixels in the area of 15 pixels around the local maximum, A_i is the amplitude which corresponds the the pixel i, A_{max} is the absolute maximum, f_i is counter variable to each pixel. This method memorizes the the sum amplitudes of absolute maxima from those hits which share the same pixel. Thus the overlapping hits problem is solved. A detailed procedure and reconstruction of overlapping hits is schematiclay shown in figure (2.16).
The spatial coordinates of the individual hits *(x,y,z)* are calculated from *(pad,time,plane)* coordinates knowing the complete geometry of the chamber, the drift velocity of the TPC, which itself depend on the electric and magnetic field (equation (2.9)) and the gas properties.

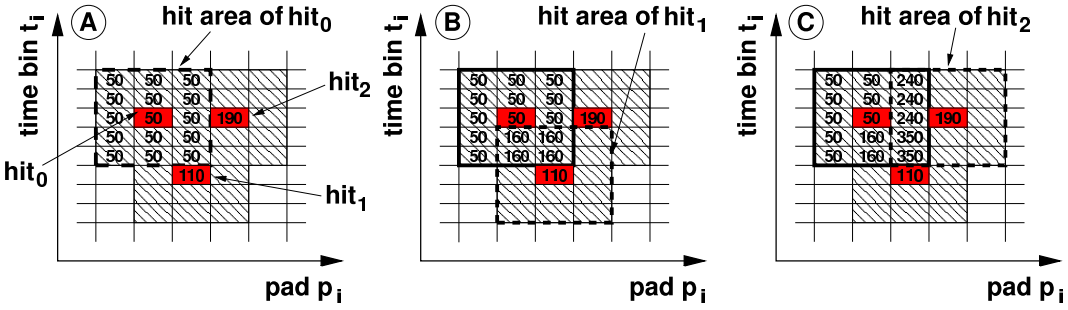

Figure 2.16: The TPC overlapping hit reconstruction. The absolute maximum of the considered hit is stored by the counter variable. It will be increases by the the absolute maxima of the overlapping neighbors whenever a founded pixel is shared to several hits.

2.7.2 The Track finding

Once the different hits are all identified and provided, it is possible to proceed to the combination of the reconstructed hits and then associate these into tracks. Depending on the polar angle, a TPC track consists of up to 20 hits. The track finding routine begins from taking a hits candidates in the middle planes of the TPC (5 to 15) along the Z-direction, where the hit density is lowest [79], and combine them with their closest neighbors in the two upstream and downstream planes in Z-direction to determine the sign of the track curvature in ϕ-direction. Within a window of $\Delta\phi = 5.3$ mrad and $\Delta\theta = 1.4$ mrad, further hits in both directions are searched around the predicted ϕ position done with a linear extrapolation using the two previous hits. If no hits were found, the procedure stops at this point. In the next step, the tracking software uses a second order polynomial with Tukey Weights [64] fit to find missing hits and to collect all the hits which are possibly

assigned to the track in several iterations. Again the tracking stops in that direction if no additional hits are found.

2.7.3 TPC Track fitting

In order to obtain the parameters defining a particle trajectory, the path of the track must be known as function of these parameters. The task of the fitting algorithm is to to provide $\overrightarrow{p}$, θ and ϕ angles of the particles. The presence of the strong inhomogeneous magnetic field in the TPC make the analytical description of the particle trajectory not possible. Therefore, the momentum of the particle is calculated using a two-dimensional momentum fit in the $\phi - z$ and $r - z$ planes based on reference tables. These tables were produced by Monte Carlo simulations of the CERES TPC using the GEANT software package [80, 81]. Applying several iterations, the hits are closed to the fitted track and those with large residuals $\Delta r > 0.4$ cm and $r\Delta\phi > 0.2$ cm are discarded from the fit.
It is assumed that the deflection in the magnetic filed is in first order only in ϕ-direction. The momentum is determined from the ϕ-deflection. The θ angle is obtained by fitting a straight line through the hits in the $r - z$ plane. A second-order corrections in θ is applied to improve the quality of the fit. The track fitting performs two types of fitting, one is the 2-parameters fit (pcor2) and the other one the 3-parameters fit (pco3). A better resolution is obtained by using a weighted combination of these two fits variables (pcomb), where their weights depend on the momentum resolution over the whole momentum range presented in figure (2.17). During this fitting we are able to determine the charge of the track by looking to the sign of the momentum. The two-parameter fit supply better results for high momentum tracks. The multiple scattering competes with the detector resolution whereby the three-parameter fit absorbs their effect for low momentum. The magnitude of the momentum and the angles θ and ϕ of the track are the whole output information of the fitting function. From the combined momentum fit, the relative momentum resolution of the CERES TPC is expressed by:

$$\frac{dp}{p} = \sqrt{(1\%p)^2 + (2\%)^2}. \tag{2.12}$$

Another parameterization is presented by taking the assumption that the track is originating from the target area, which permit to determine the local angles for the polar (θ or $\theta R2M$) and azimuthal (ϕ or $\phi R2M$) angles. This can be done and recorded by the projection of the TPC track corresponding to the second RICH mirror. Then making the TPC reconstructed track extrapolation to the target area.

$$\phi_{local} = arctan(\frac{YLine1}{XLine1}) \tag{2.13}$$

$$\theta_{local} = arctan(\sqrt{XLine1^2 + YLine1^2}) \tag{2.14}$$

where $XLine1$ is the slope in the xz plane and $YLine1$ is the slope in the yz plane of the TPC track. The angles are recalculated from the four original parameters of

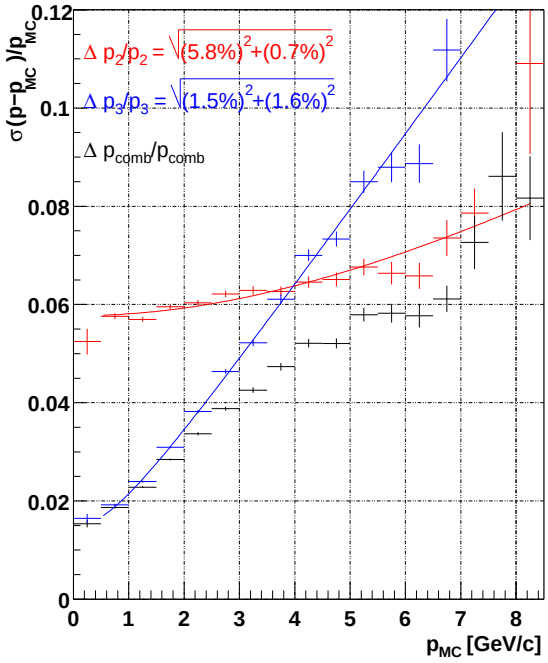

Figure 2.17: The momentum resolution obtained from a Monte Carlo simulation of the detector, the blue points used for the 3-parameter fit, the red for the 2-parameter fit and black for the combined momentum fit.

the fit $Xline0$, $Xline1$, $Yline0$, and $Yline0$ that represent the offset and the slope of straight line. The equation (2.14) is obtained for $z \to \infty$.
The relative momentum resolution dp/p as a function of the momentum p is determined by the resolution at high momentum of the detector (res.det) and the multiple scattering (ms) in the detector material at low momentum [82]:

$$\left(\frac{dp}{p}\right)^2 = \left(\frac{dp}{p}\right)^2_{res.det} + \left(\frac{dp}{p}\right)^2_{ms} \tag{2.15}$$

with

$$\left(\frac{dp}{p}\right)_{res.det} \propto p \tag{2.16}$$

$$\left(\frac{dp}{p}\right)_{ms} \propto \frac{1}{\vec{B}}\sqrt{\frac{1}{L.x_0}} \tag{2.17}$$

where: L is the the measured track length and x_0 is the radiation length.

2.7.4 The coordinate system

The global coordinate laboratory system used in the CERES experiment is shown in figure (2.18). Its origin located in the middle of the target area. The z-axis is defined by the beam axis. The event polar coordinates are the polar angle θ, the pad coordinate which is translated to the angle ϕ given by the read-out channel and the distance z to the center of the target area.

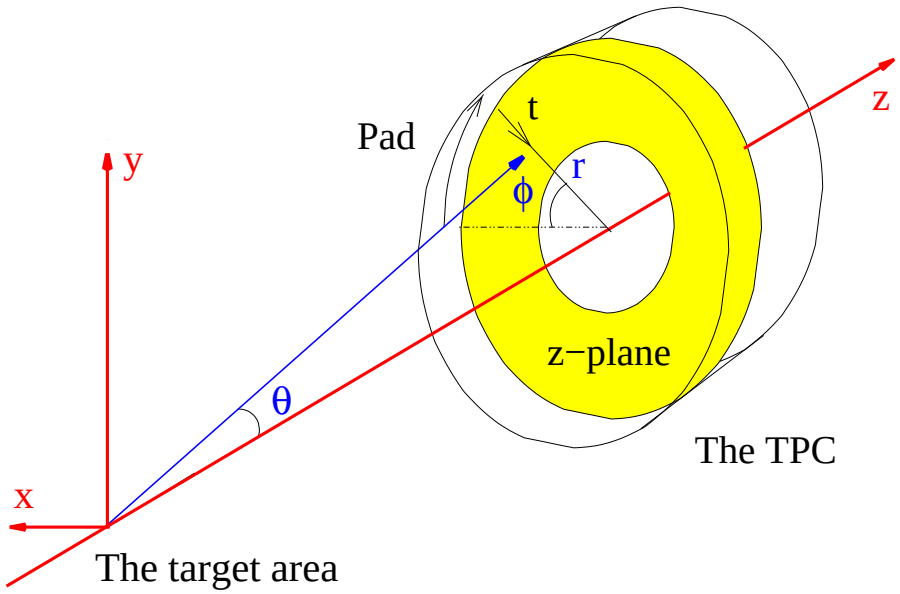

Figure 2.18: The TPC coordinate system.

2.8 Particle identification using specific energy loss (dE/dx)

Using the TPC, specific identification of charged particles can be achieved by measuring their energy loss (dE/dx). This works very well for particles having low momentum, however in the opposite case, when their energy rises, the energy loss of a particle become less mass-dependent and since it is a function of its velocity, it will be hard to separate particles with velocities $\upsilon > 0.7c$. The dE/dx of particles is described by the Bethe-Bloch formula given in equation (2.18). The energy loss of a particle with charge Z and speed $\beta = \frac{\upsilon}{c}$ passing through a medium with the density ρ is given by:

$$dE/dx = Kq^2 \frac{Z}{A} \frac{1}{\beta} \left(\frac{1}{2} \frac{2m_e c^2 \beta^2 \gamma^2 T_{max}}{I^2} - \beta^2 - \frac{\delta}{2} \right) \tag{2.18}$$

where $K = 4\pi N_A r_e c^2$, N_A is the Avogadro number, r_e is the electron radius, Z the atomic number of the absorber, A the atomic weight of the absorber,$\gamma = 1/\sqrt{1-\beta^2}$, T_{max} the maximum kinetic energy in a single collisions, I the mean excitation energy and δ is the Bethe-Bloch correction factor.
Figure 2.19 shows the energy loss of the observed charged particles in the CERES TPC as a function of the momentum of the particles and compared with the Bethe-Bloch formula described above.

2.9 Photon interactions in matter

Photons are electromagnetic radiation with zero mass, electrically neutral and traveling with a constant velocity that is always the speed of light c. A photon passing through material interacts in different ways.
There are four important mechanisms of interactions between the photon and matter. In all these mechanisms of the process, the photon gives up a part or all its energy to a matter particle. This is usually happening in the vicinity of an atomic nucleus. The Compton effect where the photon can be scattered by an electron (or a nucleus) and loose some of its energy. Note that the photon does not slowdown. It is still traveling with the velocity c, but its frequency is reduced. At lower energies the dominant process is the photoelectric effect. The photon collide with the electron and ionizes the atom of the matterial by kicking out one electron.
Other process equivalent to the previous one but in this case the photon energy is not enough to free the electron. Thereby, the photon is captured by the atom and excites the state of the hitted electron in the shell to higher energy level. Again,

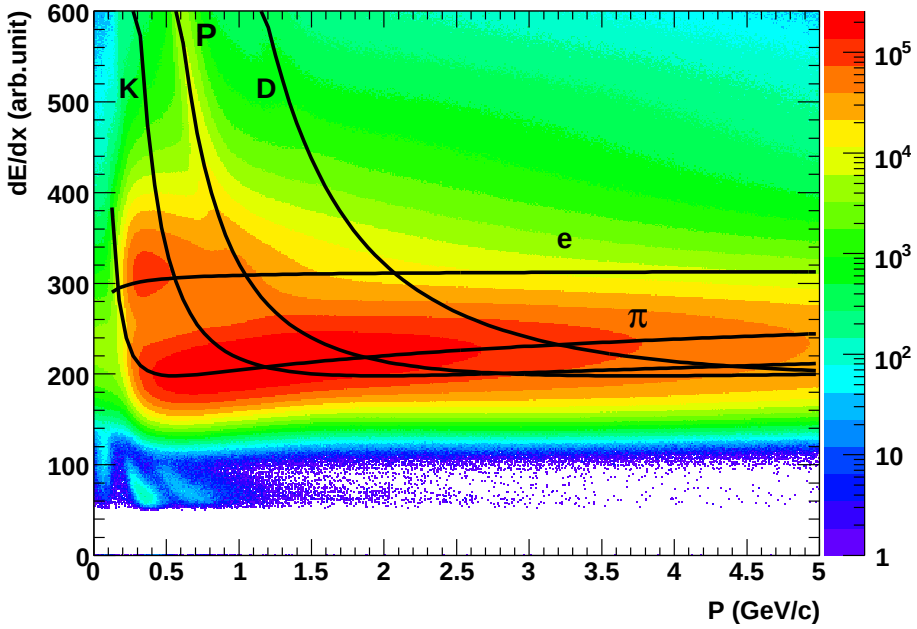

Figure 2.19: The energy loss of charged particles as a function of their momentum.The lines indicate the predicted dE/dx areas by the Bethe-Bloch formula for π, K, P, d and e

the photon disappears and transmits all its energy to the atom. The last common process, which is the formation or the materialization of two electrons, one negative (electron) and the other one positive (positron). This process is called *Pair production*. It is a direct conversion of radiant energy to matter. This process makes the detection of photons in the CERES experiment possible.

2.9.1 Photon conversions ($\gamma Z \longrightarrow e^+e^-Z$)

The CERES/NA45 experiment measures photon by conversion method. For Pair Production to occur, the electromagnetic energy, or the photon energy, must be at least equivalent to the mass of the two electrons. When the photon energy is greater than $2m_ec^2$, which corresponds to 1.022 MeV, the photon can be materialized by the creation of electron-positron pair. For photon energies above the threshold energy, the surplus energy appears as kinetic energy of the two electrons. An additional condition which must be satisfied during the Pair Production process because it can not occur in the vacuum. The energy and the momentum can not be simultaneousley conserved. Something must participate in the interaction

and absorb the momentum of the initial photon to balance the equations. The presence of a charged particle like an atomic nucleus, which is more massive than the electron/positron, during the interaction can absorb a fraction of the photon momentum. The Pair Production is the dominant process at high energies and a very small opening angle between the electron and the positron is expected on the average $2m_ec^2/E_\gamma$ [83].
Since the photons are massless, they are not detected directly. Their states are displaced as "neutral vertex". The converted electrons are identified by the searching for oppositely charged track near the electron track, then we do the extrapolatation to a common target point. Tracks found in this way are subsequently used as starting point for track combinations and a converted photon is created for each valid pair. We have to remember that our our goal is to reconstruct the photons through conversions happening mainly in the $RICH2$ mirror location.

2.9.2 Radiation length

The passage of photons through matter were governed by the processes described in the previous sections. The average length in a specific material in which the created electrons will lose an amount of their energy by bremsstrahlung or pair production is called the radiation length [84, 85]. The radiation length is usually measured in g/cm^2 and can be expressed by the following equation:

$$\frac{1}{X_0} = 4\alpha r_e^2 \frac{N_A}{A}(Z^2[L_{rad} - f(Z)] + ZL'_{rad}) \tag{2.19}$$

here α is the fine-structure constant $(1/137.035)$, $r_e = 2.817.10^{-15}m$ the classic electron radius, A is the atomic mass and Z is the atomic number which characterizes the traversed material. N_A is the Avogadro number $(6.022.10^{23}/mole)$.

The distance traveled by the high energy photon before it produces electron pair is related to the radiation length by $(7/9)\ X_0$. This distance is called the mean free path for pair production. The pair creation happens with a probability of:

$$P = 1 - exp(\frac{-7}{9}\frac{x}{X_0}) \tag{2.20}$$

We are using the second RICH mirror as converter. It is assembled from 10 individual pieces and it is conventional a $6mm$ glass mirror which corresponds to 4.5% radiation length. The geometrical acceptance of the RICH2 mirror is in the θ range 0.14-0.24 within the pseudorapidity range 2.1-2.65.

Science creates more science, like a fire; and the conditions for nursing it and keeping it burning are much the same...
It is like climbing a tree. At the first fork, we choose-or, in this case, "nature" or the experimental outcome chooses-to go to the right branch or the left; at the next fork, to go left or right; and so on.

John R. Platt

3 The Data Analysis

This chapter describes in greater details the neutral pion analysis with emphasis on the proof and on the justification for making various cuts. Applying a set of electron/positron track selection criteria in order to reject combinatorial background. These choices and the obtained results will be used for the photon reconstruction. The reconstruction of the neutral pion from the converted photons in the RICH2 mirror will be discussed in this chapter.

3.1 Event data sample

The data analyzed in this Thesis were taken in the year 2000. The CERES/NA45 experiment has recorded on tape a large data sample consisting of 30 million good event in Pb-Au collisions at beam energy 158 GeV/c having a centrality of the top 7%(20%) of the total geometric cross section with an average multiplicity of $< dN_{ch}/dy >= 321$ [68] and the pseudorapidity range $\eta = 2.1 - 2.65$. The typical Pb beam intensities delivered to CERES from the SPS was $\sim 1 \times 10^6$ ions per burst corresponding to a total interaction rate of 300 to 500 event/ burst. The highly compressed raw data on tape coming from the detectors and written by the Data Acquisition System (DAQ) have to be unpacked and converted into a suitable format for the subsequent data analysis. The events are grouped into 415 units, each unit consisting of about 200 bursts.
The analysis is performed in the framework of the C++ software package COOL (Ceres Object Oriented Library) with all the functionality needed to handle and to analyse a large amount of data in a very efficient way. The data are defined

as ROOT Tree format specialized storage methods which are used to get direct access and process. A complete particle trajectories reconstructed once all data has been processed into meaningful physical information is stored (i.e. for each particle track a necessary information from each detector is stored like hit amplitudes and number of hits).

3.2 The reconstruction chain

The different steps of the reconstruction chain in order to get the π^0 signal are listed below. In describing this, we shall keep the chronological order of the analysis program which can be represented by the following scheme:

1. Hit reconstruction and tracking.
2. Electron identification.
3. Pairing $e^+e^- \longrightarrow \gamma$.
4. Identification of γ conversions.
5. Invariant mass $\gamma\gamma$ in the same event as function of p_t and y.
6. Invariant mass of $\gamma\gamma$ in mixed event as function of p_t and y.
7. Background subtraction and raw π^0 yield determination as function of p_t and y.
8. Efficiency and acceptance determination.
9. Efficiency and acceptance correction of π^0 yields.
10. Transverse momentum spectrum of π^0.

The first point that was described in Section 2.7.1 is common to all physics analysis done with the 2000 CERES data. The other steps are specific for the analysis presented here. Therefore, they will be described in much more details in this Chapter (points 2 to 7) and the Chapter 4 (point 8) and Chapter 5 (points 9 and 10).

3.3 The Electron and Positron selection

The charged particle multiplicity distribution determined by the Silicon Detector (SD) and the TPC for the events of the year 2000 data set is shown in figure (3.1). In our analysis, we use only events with a TPC multiplicity larger than 10.

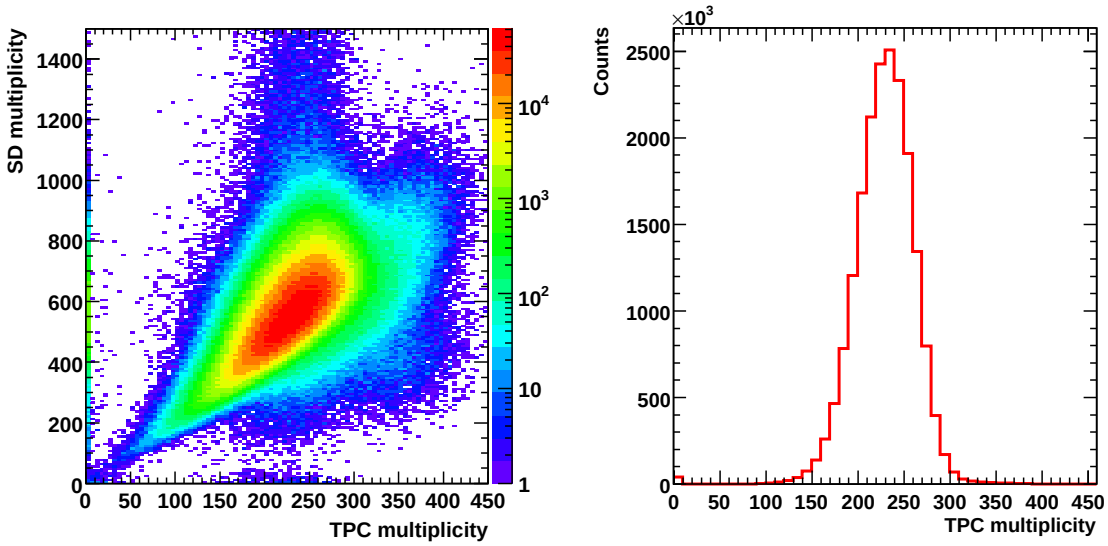

Figure 3.1: Left, The charged particle multiplicity as measured tracks by the SD and TPC detectors. Right, the reconstructed charged particle multiplicity with the TPC detector.

The particle identification (PID) in the TPC using the specific energy loss dE/dx provides a powerful tool to select electrons, positrons and to separate them from kaons, pions and protons. The energy loss (dE/dx) described in the previous chapter (see section 2.8) is a function of the mass and the momentum of the charged particle which passes through the medium. The momentum is determined by the curvature of the track due to the magnetic field.

Figure (3.2) shows evident points concentration distribution (bands), each corresponding to a specific mass of particle. This function that was expressed within the equation (2.18) gives a curve as a function of the particle energy that is characterized by a decrease leading to a minimum which is then followed by a rapid increase. This means that the resolution is good at low momentum and it becomes gradually deteriorated when the momentum is increasing. In order to reduce the background and optimize the significance, selection criteria are imposed to select

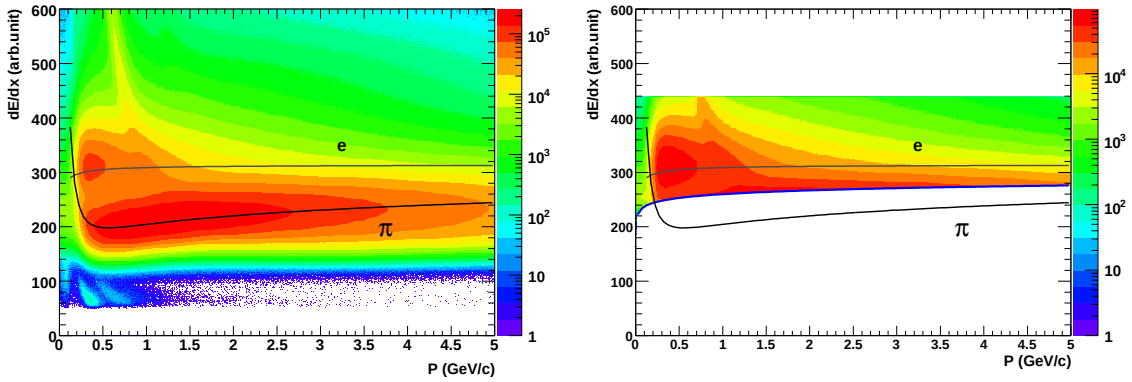

Figure 3.2: Left: Specific energy loss of charged particles versus its momentum. The lines shows the expected dE/dx for electrons and of charged pions. Right, Specific energy loss versus momentum after the applied cuts to select electrons (positrons) among charged particles.

only the provided dE/dx information for the electron and the positrons tracks. The right of the figure (3.2) represents all the accepted charged particles after taking the dE/dx band in the region $308 - 2\sigma_{dE/dx} < dE/dx < 440$ and along the momentum interval. However, this cut does not prevent the contamination of the charged pions when theirs energy loss overlap. This contamination is clearly visible on the left of the figure. An extra dE/dx condition depending on the momentum is then needed. The additional cut $dE/dx > 260 + 10logp$ is included and represented by the blue incline line (figure (3.2) right) which allows the suppression of the $\pi^{\pm}$ contaminations.
The distribution of the electron (positron) multiplicity per event after the selection by using dE/dx information is shown in figure (3.3). A mean number of electrons (positrons) of 30(32) event is observed. The larger mean number of positrons might be due to proton contamination.

3.4 The standard quality cut

The track quality criteria is used to accept only the well defined tracks and to reject the fake tracks. The track quality cuts is essentially a cut on the number of the hits on the track. The distribution of number of TPC hits is shown in figure (3.4). The main requirement is that the track must have a minimum number of associated hits. The reason of this requirement is that the tracks should have a good momentum resolution and also good dE/dx resolution. Both the momentum and dE/dx resolutions are improved by the number of hits.

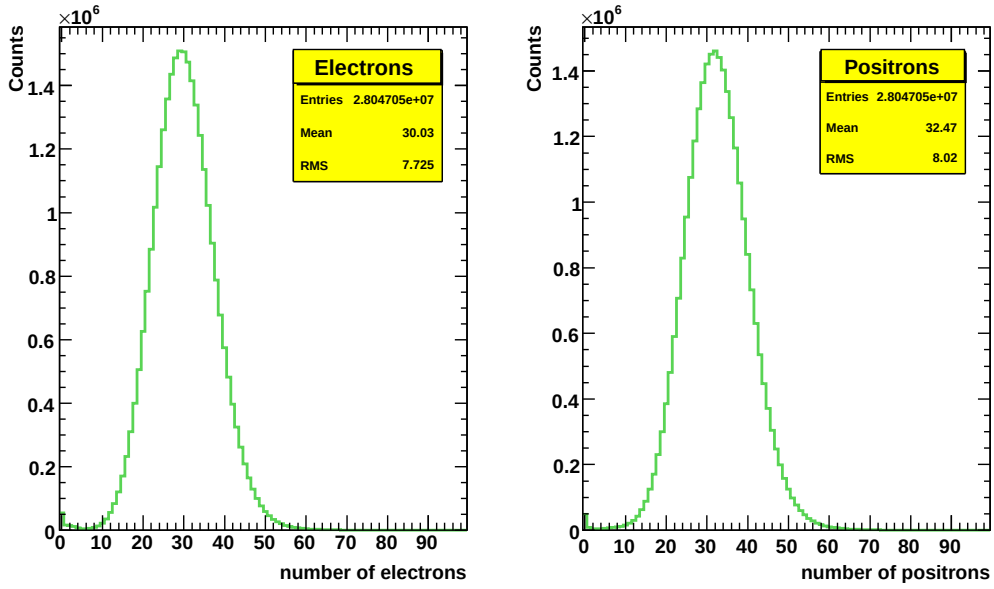

Figure 3.3: The multiplicities of electrons and positrons in each event. The selection was obtained by using the specific energy loss information provided by the TPC detector.

The distribution of the recorded number of hits on the TPC segment versus the theta angle is shown in figure (3.5). Only the tracks which they have more than 10 hits will be kept for the analysis performed later. Tracks at large theta leave the TPC before reaching the end therefore they have less number of hits. Similar effect happens at low theta, where the tracks enter the TPC later. A cut that follows this dependence (black line in figure (3.5)) is applied.

3.5 The study of the unlike (e^+e^-) and like sign e^+e^+, e^-e^- pairs

In our case, as first step from the reconstruction scheme, we start firstly by the electron/positron combinations. The associated phase space of the *electron-positron* combination will define the photon. This latter ensemble of the opposed signs represents the signal of a *"good"* photon.
Before going to discuss the photon reconstruction part, we have to keep in mind that we are concerned with the reconstruction of photons that convert (shortly) before the TPC spectrometer into e^+e^- via the measurement of the electron pair

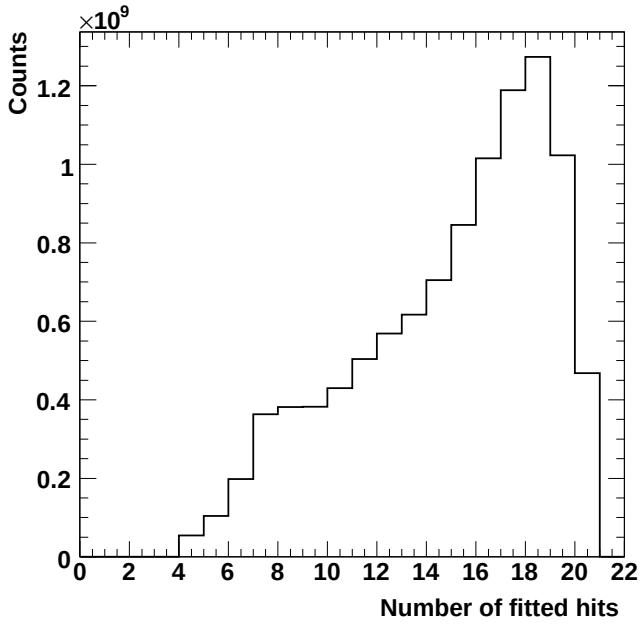

Figure 3.4: The distribution of the number of the TPC fitted hits

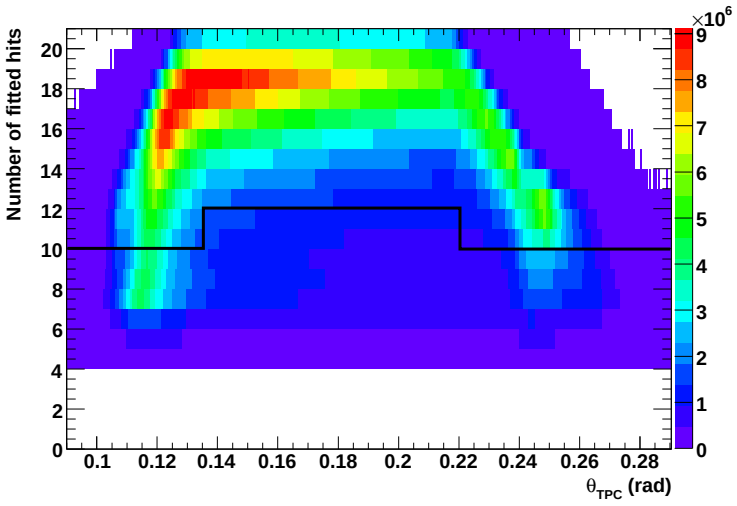

Figure 3.5: Dependence of the number of hits per track versus the theta angle. The black line indicates the theta dependent cut applied to the tracks.

in the TPC.
The e^+e^- pairs from the photon conversion are characterized by a very small opening angle. Therefore by inspecting the opening angle distributions of e^+e^- pairs and comparing them to like sign combinations where no signal is expected, one should be able to find out the photon conversion signal.
The opening angle (θ_{12}) between the electron and the positron can be expressed by the equation:

$$\cos\theta = \frac{p_{x1}p_{x2} + p_{y1}p_{y2} + p_{z1}p_{z2}}{|p_1||p_2|} \tag{3.1}$$

where the p_1 and p_2 are the momentum vectors for the electron and the positron respectively.
The opening angle distribution of the unlike sign pairs (e^+e^-) and the like signs pairs ($e^+e^+ + e^-e^-$) for different p_t have been investigated in order to optimize the definition of the photon for efficiency and significance.
The momentum variation of the opening angle between the unlike sign pairs (e^+e^-) and the like-sign pairs ($e^+e^+ + e^-e^-$) is shown in figure (3.6). No extra normalization factor is applied in the like-sign distributions.
The peak in each momenta window at small opening angles indicates clearly the existence of photons converted before the Time Projection Chamber. The peak becomes narrower and the number of the photons is decreasing when one goes to the high momentum regions.

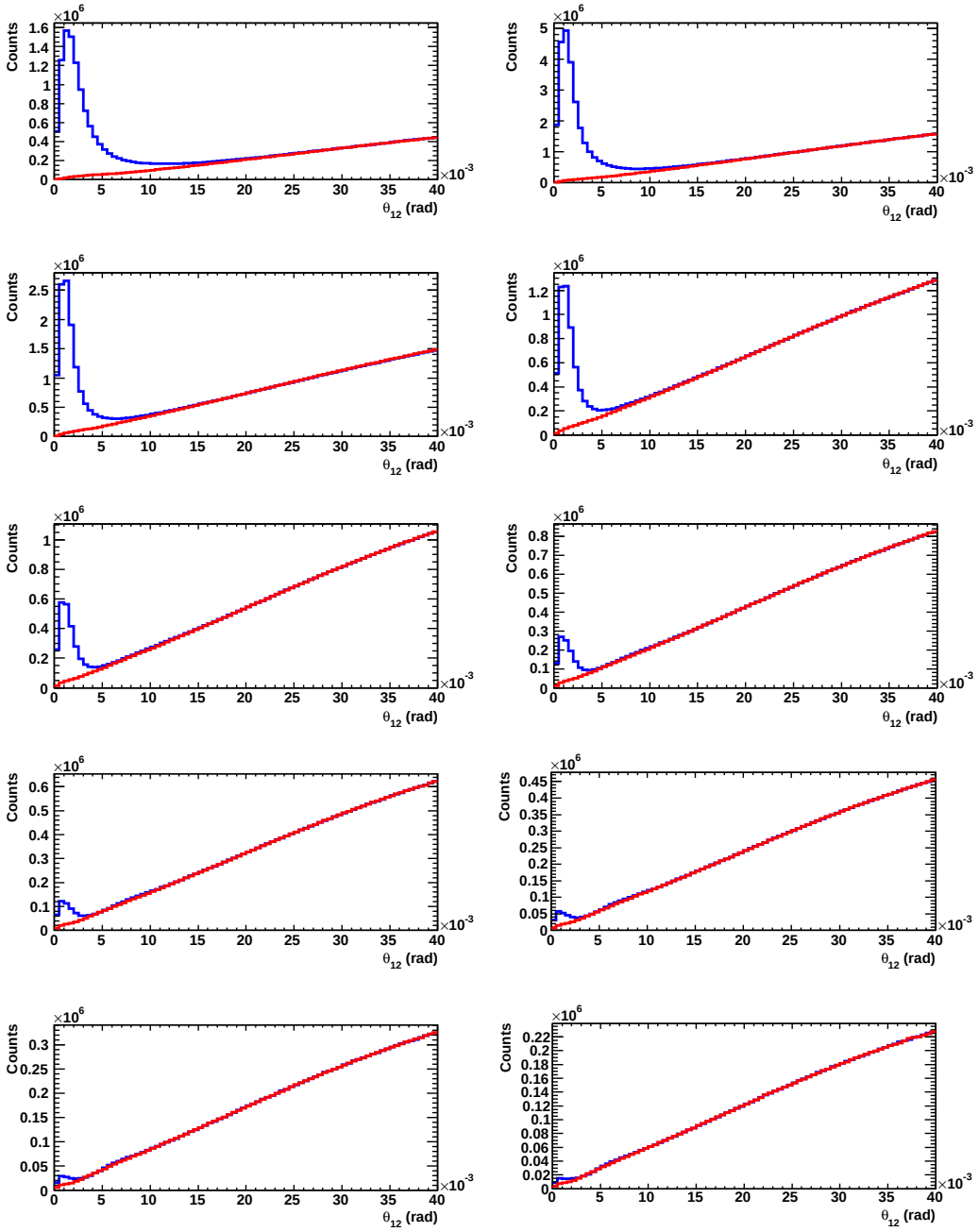

Figure 3.6: The distribution of the opening angle between the unlike sign e^+e^- (blue line) and the like sign $e^+e^+ + e^-e^-$ (red line) pairs in pair momentum bins from 0 to 10 GeV/c, each window represents 1 GeV/c.

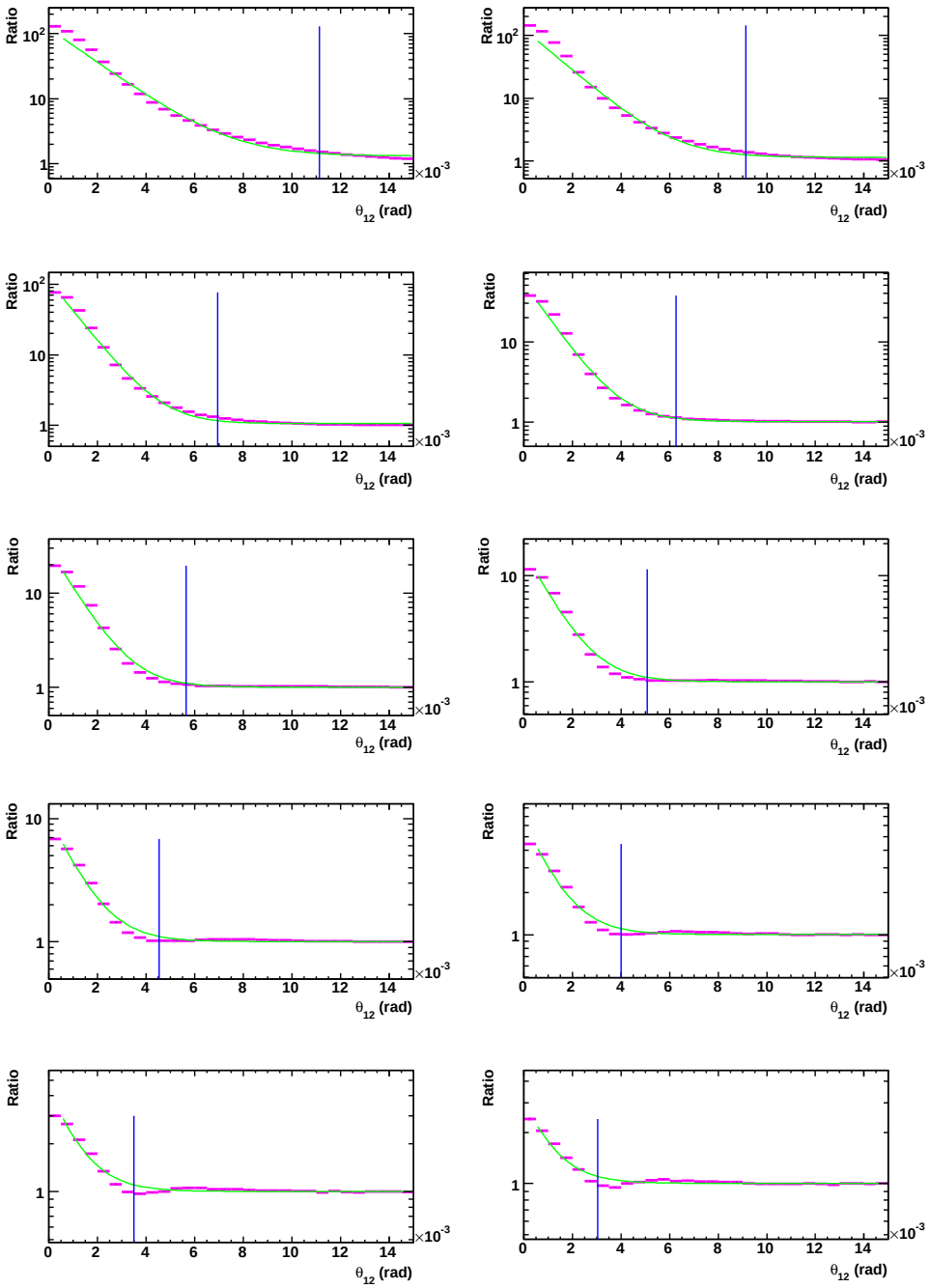

Figure 3.7: The ratio of the unlike sign e^+e^- and the like sign $e^+e^+ + e^-e^-$ pairs vs the opening angle in pair momentum slices from 0 to 10 GeV/c, each window represents 1 GeV/c. The vertical line in each momentum bin indicates the cross-point angular cut.

In order to determine more precisely up to which opening angle the converted photon signal extends, the ratio of the unlike sign and like sign distributions has been studied for different momentum bins (figure (3.7)). Each distribution is fitted by a sum of a constant and an exponential function which take the form:

$$\text{ratio} = \text{p}_0 + \exp(\text{p}_1 + \text{p}_2\theta_{12}) \tag{3.2}$$

The vertical lines in each momentum bin were calculated as the opening angle points where the ratio is 10% higher than the constant level (p_0). This leads us to what we call the *cross-point*. The cross-point definition can be expressed by the following parameterization:

$$\text{crosspoint}(\theta_{12}) = 1/\text{p}_2 \cdot (\ln(0.1 \cdot \text{p}_1) - \text{p}_1) \tag{3.3}$$

where p_1 and p_2 refer to the fit function parameters mentioned previously in the equation (3.2). The photon conversion signal sits below the cross-point. The dependence of the cross-point with the pair momentum is shown in figure (3.8).
We can define the $ThetaEP$ cut function as:

$$\text{ThetaEP(p)} = \begin{cases} f_1, & \text{if}: \quad \text{p} \in [0, 8.5](\text{GeV/c}) \\ \\ f_2, & \text{if}: \quad \text{p} \in [8.5, \infty](\text{GeV/c}) \end{cases} \tag{3.4}$$

where:

$$\text{f}_1 = \exp(\text{a}_0 + \text{a}_1\text{p} + \text{a}_2\text{p}^2 + \text{a}_3\text{p}^3) \quad \text{with} \quad \text{p} \in [0, 8.5] \tag{3.5}$$

The value of the different parameters are indicated in table 3.1.

$$\text{f}_2 = 3.5 \quad (\text{mrad}) \tag{3.6}$$

a_0 (rad)	a_1 (rad/GeV)	a_2 (rad/GeV^2)	a_3 (rad/GeV^3)
-4.325 ± 0.0018	-0.3548 ± 0.0015	0.04698 ± 0.0004	0.002763 ± 3.5e-5

Table 3.1: The parameter values of the ThetaEP cut function in the momentum interval 0-8.5 GeV/c.

f_1 function corresponds to the curved line and f_2 is the horizontal line at the opening angle 3.5 mrad for p larger than 8.5 GeV/c. In what follows, the $ThetaEP$ cut function will kept during the whole analysis described later and it defines the signature of conversions.

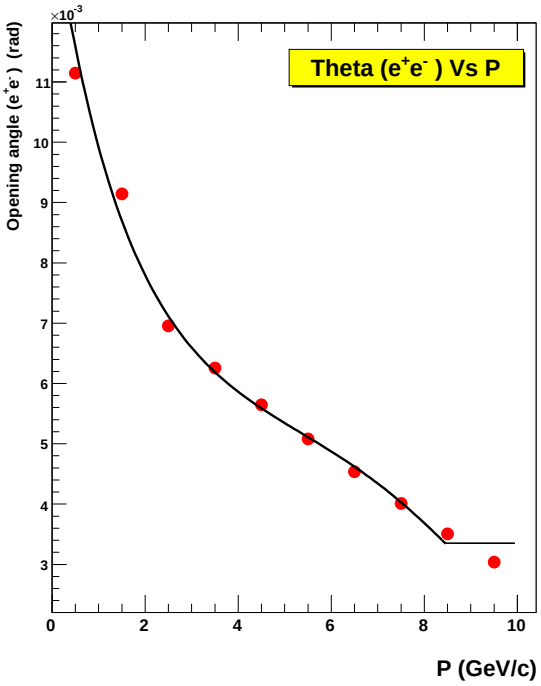

Figure 3.8: The electron-positron opening angle (cross-point) vs the momentum, the curved and the horizontal line indicates the applied cut values to define photons.

3.6 The photon reconstruction

3.6.1 Map of reconstructed photon conversions

So far we have concentrated on the description of the unlike and like sign pairs opening angle distributions as building blocks for the photon by using the TPC information. The number of photons per each event is displayed in figure (3.9).

The measured transverse momentum of the reconstructed primary photon and of the background from the unlike and like sign pairs is shown in figure (3.10). Photons are measured from a transverse momentum of 0.1 GeV/c up to 1 GeV/c.

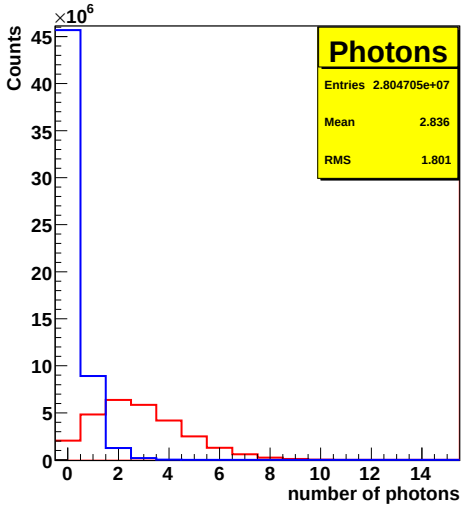

Figure 3.9: The number of the reconstructed photons (red) in each event by using the dE/dx information provided from TPC detector and after the ThetaEP cut function.

Figure (3.11) illustrates the azimuthal and the polar angles distributions for the primary photon selection based on the data collected previously. In the X-Y plane, the photons are measured for the whole azimuthal acceptance. The reconstructed conversion point map has two clear structures, one uniform comming from conversions in the RICH2 mirror and γ-fold structure comming from a support structure in the entrance of the TPC. However, a cut in photon angle $0.135 \leq \theta \leq 0.24$ was used to select only the phase-space where the photons have good momentum resolution. Thus, by applying this polar angle cut we exclude the photons affected strongly from the multiple scattering or the Bremsstralung processes which are mainly happening at lower polar angles where there is a lot of material. The transverse momentum distribution has sharp peak near zero and broader peak at high transverse momentum. This behavior can be understood from the fact that the photon conversion is characterized by very small electron-positron opening angle.

3.7 The Secondary Vertex (SV) fit algorithm

The Secondary vertex technique provide a very clean and well measured position of the photon conversion point. Opposite charged tracks are combined to obey the physical process $\gamma Z \longrightarrow e^+e^-Z$ candidates. Each of the two tracks is assumed to point out to a common position. Consequently, an implicit *"zero mass"* on the invariant mass for the displaced vertices is yielded at the $RICH2M$ region.

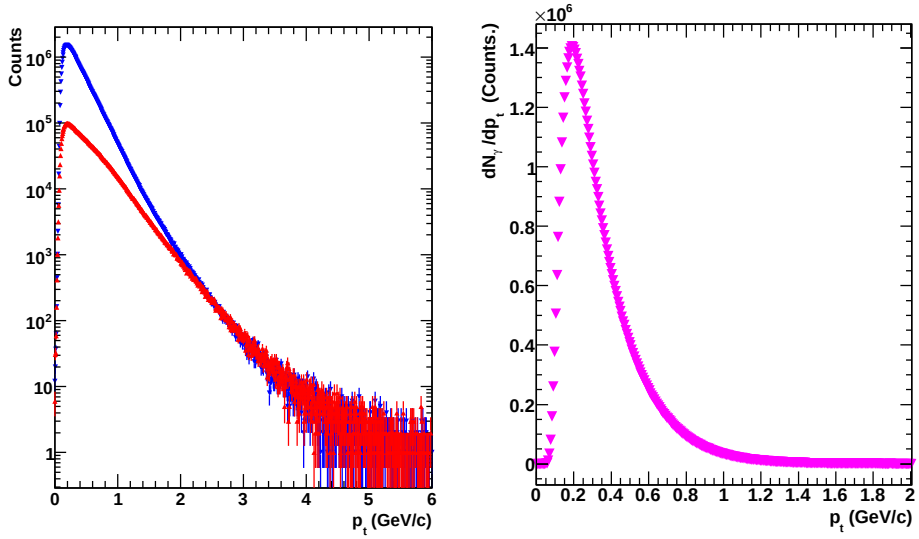

Figure 3.10: Left: Momentum distribution of the reconstructed photons from the unlike sign pairs (blue) and of the background (red) from like signs. Right: the photon transverse momentum spectrum after the subtraction of the background.

The principle of the Secondary Vertex fit algorithm is to calculate the 3D distance between the two tracks. The used algorithm calculates the point of closest approach assigned to the electron and to the positron. This method is performed on the Least Square Method. It was used by HADES [86] and CERES [78] collaborations. For the complete details and all the characteristic features of this method the reader is advised to consult [87].
The study of the vertexing and kinematic fitting within the Secondary Vertex algorithm will be divided into two subsections. The first part will be intended to provide the mathematical framework of the vertex fitting. This is handled generally by solving analytically the closest approach point equations of the two opposite sign tracks. Then, we will examine in more details and explicitly make the practice calculation of the closet approach point occurring from the latter subsection.

3.7.1 The mathematics of the Secondary Vertex fit

The general way of the finding the Secondary Vertex is based by the following prescription. All the tracks are parameterized as straight lines and used as input to the algorithm. Assuming that there are N detected tracks that means for each input candidate $i \in [1, N]$ and from the linearity hypothesis, we write the definition

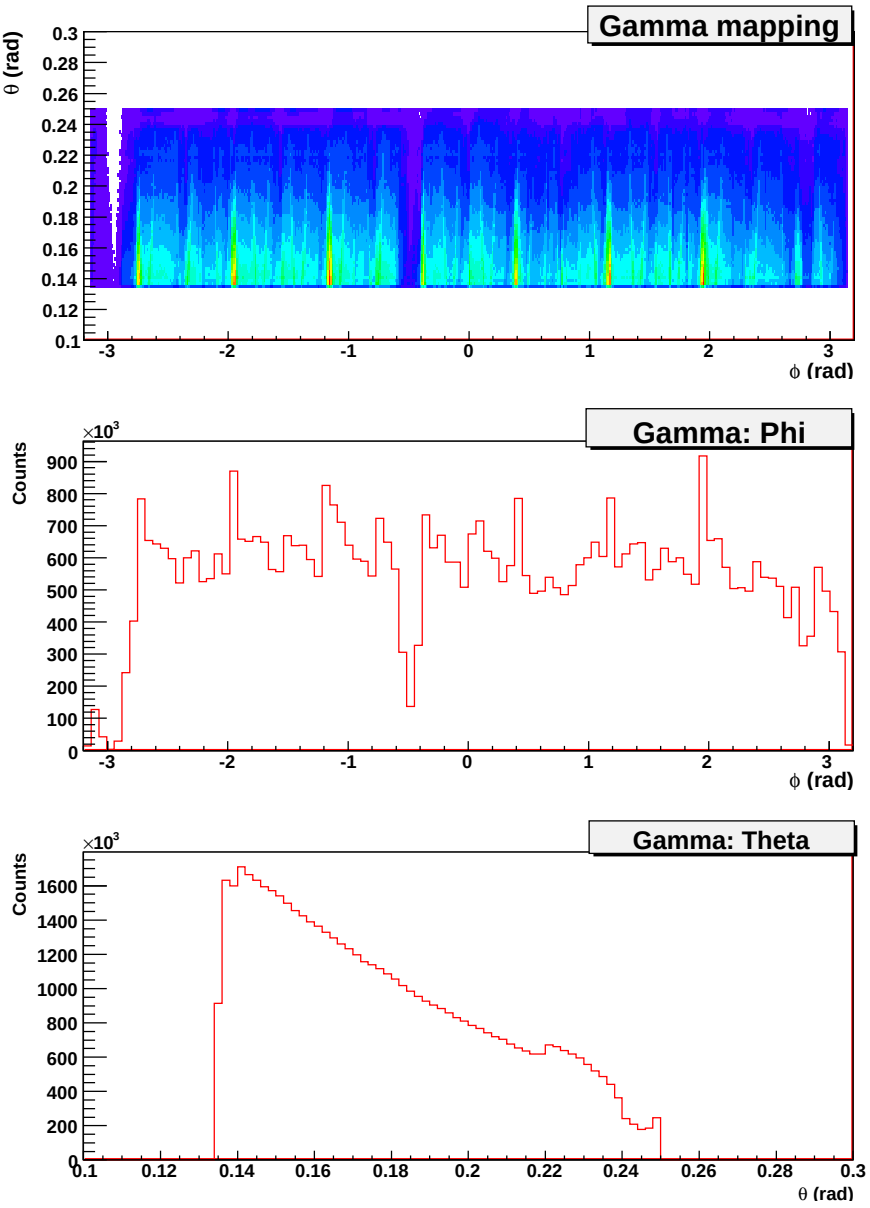

Figure 3.11: The mapping of the reconstructed photons in the phase-space. The top window represents the bidimentional distribution of the azimuthal and polar angles for the reconstructed photons. The middle and the bottom windows shows the projection of the $theta_\gamma$ and the ϕ angles, respectively.

of the i^{th} track in the form:

$$\vec{x_i} = \vec{r_i} + \vec{u_i}.t, \quad t \in \Re \tag{3.7}$$

such that $\vec{r_i}$ refers to the position vector, $\vec{u_i}$ its direction vector,i.e. $\vec{u_i} = \vec{r_i}/|\vec{r_i}|$ and t is the track parameter or the so-called controlled variable. We will attempt to determine the unknown coordinates is space of the position vector $\vec{r_{sv}}$ which is assigned to the point of conversion. The distance of the conversion point to a given i^{th} track which is basically expressed in the equation (3.7) can be calculated as:

$$D_i = |(\vec{r_i} - \vec{r_{sv}}) \times \vec{u_i}| \tag{3.8}$$

Equation (3.8) is concluded from the fact that $\vec{r_i}$ vectors set are the measured data points and the D_i represents the deviations from the given set of data in the base $|\vec{u_i}|$. According to Least Square method, the fitting proceeds by finding the sum of the squares of the deviations D_i for all the detected tracks. For all the measured data points, there are given uncertainties; for that reason these points can be weighted differently in order to give the high-quality points more weight. Based on this, the squares deviations are therefore summed and minimized to find the best fit line. This can yields the following:

$$M^2 = \sum_{i=1}^{N} \frac{D_i^2}{\sigma_i^2} = \sum_{i=1}^{N} |(\vec{r_i} - \vec{r_{sv}}) \otimes \vec{u_i}| \tag{3.9}$$

By taking the uncertainties σ_i^2 constant, the minimization of M^2 is thus equivalent to the determination of the space coordinates of the closest approach between the N tracks. The minimization of M^2 is simply done by making the partial derivatives of M^2 with respect to the unknown parameters and set these values to zero. The M quantity defined in equation (3.9) has a property which can be used to carry out a χ^2 test. We now write this consequence ,the analogous expression of 3, in the form:

$$\chi^2 = \sum_{i=1}^{N} \frac{D_i^2}{\sigma_i^2} \tag{3.10}$$

The condition for the χ^2 to be minimum is that:

$$\frac{\partial \chi^2}{\partial x_{sv}} = 0, \quad \frac{\partial \chi^2}{\partial y_{sv}} = 0, \quad \frac{\partial \chi^2}{\partial z_{sv}} = 0 \tag{3.11}$$

To determine the equation(3.11), we first have to get the distance between the two selected charged tracks D_i^2.i.e.:

$$\begin{aligned} D_i^2 &= [(y_i - y_{sv})a_{zi} - (z_i - z_{sv})a_{yi}]^2 \\ &\quad +[(z_i - z_{sv})a_{xi} - (x_i - x_{sv})a_{zi}]^2 \\ &\quad +[(x_i - x_{sv})a_{yi} - (y_i - y_{sv})a_{xi}]^2 \end{aligned} \tag{3.12}$$

Expanding the equation system (3.11), this leads to:

$$\begin{aligned}
\frac{\partial\chi^2}{\partial x_{sv}} &= \sum W_i \{[(z_i - z_{sv})a_{xi} - (x_i - x_{sv})a_{zi}]a_{zi} - [(x_i - x_{sv})a_{yi} - (y_i - y_{sv})a_{xi}]a_{yi}\} = 0 \\
\frac{\partial\chi^2}{\partial y_{sv}} &= \sum W_i \{[(x_i - x_{sv})a_{yi} - (y_i - y_{sv})a_{xi}]a_{xi} - [(y_i - y_{sv})a_{zi} - (z_i - z_{sv})a_{yi}]a_{zi}\} = 0 \\
\frac{\partial\chi^2}{\partial z_{sv}} &= \sum W_i \{[(y_i - y_{sv})a_{zi} - (z_i - z_{sv})a_{yi}]a_{yi} - [(z_i - z_{sv})a_{xi} - (x_i - x_{sv})a_{zi}]a_{xi}\} = 0
\end{aligned} \tag{3.13}$$

where the W_i is the weighting factor $2/\sigma_i^2$ The equation (3.13) is linearized in the unknown parameters of the space coordinates. Involving matrix manipulations and especially matrix inversions, the equation system in (3.13) can be summarized in three main matrices labeled as A, B and C which satisfy the equation:

$$\mathbf{C} = \mathbf{A}^{-1}\mathbf{B} \tag{3.14}$$

The expressions of these specific matrices are written in the matricial form and obtained as follow:

$$\mathbf{A} = \sum_{i=1}^{N} W_i \begin{pmatrix} a_{yi}^2 + a_{zi}^2 & -a_{xi}a_{yi} & -a_{xi}a_{zi} \\ -a_{yi}a_{xi} & a_{xi}^2 + a_{zi}^2 & -a_{yi}a_{zi} \\ -a_{zi}a_{xi} & -a_{zi}a_{yi} & a_{yi}^2 + a_{xi}^2 \end{pmatrix} \tag{3.15}$$

$$\mathbf{B} = \mathbf{A} \begin{pmatrix} x_i \\ y_i \\ z_i \end{pmatrix}, \tag{3.16}$$

and the wanted matrix:

$$\mathbf{C} = \begin{pmatrix} x_{sv} \\ y_{sv} \\ z_{sv} \end{pmatrix}, \tag{3.17}$$

Once this problem is handled by solving analytically the point of closest approach of the two charged tracks (the two candidates), we could then determine the A,B and C matrices. The latter C matrix is $1-$column matrix which offers the space coordinates values of the conversion point..
It may be, however, that the uncertainties σ_i are not normally distributed. and theirs expectation values are different from zero. This constraint implies dependency of the σ_i uncertainties on the D_i distances(i.e. $\sigma_i^2 = \sigma_i^2(D_i)$). In this case special care on the calculation of σ_i's values because we are dealing with non-negligible values of errors. It can be redefine and one gets the alternative expression as:

$$\sigma_i^2(D_i) = \left(\frac{\partial D_i}{\partial x_1}, \frac{\partial D_i}{\partial y_1}, \frac{\partial D_i}{\partial x_2}, \frac{\partial D_i}{\partial y_2}\right) \begin{pmatrix} \sigma_{x_1x_1} & 0 & \sigma_{x_1x_2} & 0 \\ 0 & \sigma_{y_1y_1} & 0 & \sigma_{y_1y_2} \\ \sigma_{x_2x_1} & 0 & \sigma_{x_2x_2} & 0 \\ 0 & \sigma_{y_2y_1} & 0 & \sigma_{y_2y_2} \end{pmatrix} \begin{pmatrix} \frac{\partial D_i}{\partial x_1} \\ \frac{\partial D_i}{\partial y_1} \\ \frac{\partial D_i}{\partial x_1} \\ \frac{\partial D_i}{\partial y_2} \end{pmatrix} \tag{3.18}$$

With the definition written in equation (3.18), (x_1, y_1) refers to the track space coordinates by requiring $z = 0$. (x_2, y_2) are the corresponding slopes in the X-Z plane (for x_2) and Y-Z plane (for y_2). Thus, that reads:

$$\begin{cases} x_2 = \dfrac{u_x}{u_z} \\ \\ y_2 = \dfrac{u_y}{u_z} \end{cases} \tag{3.19}$$

where (u_x, u_y, u_z) are the coordinates of the unit direction vector $\vec{u}$. The σ_{mn} refers to covariance if $m \neq n$ and in the opposite case $m = n$ it corresponds to the variance of the m and n parameters. In what follows, we will use a short notations to simplify the complication of the equations. Let:

$$\vec{\Delta}_i = \Delta_x \vec{i} + \Delta_y \vec{j} + \Delta_z \vec{k}. \tag{3.20}$$

and

$$\vec{\Delta}_i = \vec{r}_i - \vec{r}_{sv}. \tag{3.21}$$

from the equations (3.20) and (3.21) one can gets:

$$\begin{cases} \Delta_x = x_i - x_{sv} \\ \Delta_y = y_i - y_{sv} \\ \Delta_z = z_i - z_{sv} \end{cases} \tag{3.22}$$

Furthermore, the unit vector property provide us:

$$u_z^2 = 1 - u_x^2 - u_y^2 \tag{3.23}$$

which leads to:

$$\begin{cases} \dfrac{\partial u_z}{\partial u_x} = -\dfrac{u_x}{u_z}, \\ \dfrac{\partial u_z}{\partial u_y} = -\dfrac{u_y}{u_z} \end{cases} \tag{3.24}$$

From these formulas, the equation 3.12 can be re-written in the following compact form:

$$\begin{aligned} D_i^2 &= (\Delta_{zi}^2 - \Delta_{xi}^2)u_{xi}^2 + (\Delta_{zi}^2 - \Delta_{yi}^2)u_{yi}^2 - 2(\Delta_{yi}\Delta_{zi}u_{yi}u_{zi}) \\ &\quad +\Delta_{xi}\Delta_{zi}u_{xi}u_{zi} + \Delta_{xi}\Delta_{yi}u_{xi}u_{yi}. + \Delta_{xi}^2 + \Delta_{yi}^2 \end{aligned} \tag{3.25}$$

and the partial derivatives in equation 3.18 will be computed with respect to u_x and u_y and not for the x_2 and y_2 cases (this step will be done later). Thus, the results of the updated partial derivatives of the distance D_i are and obtained as:

$$\begin{aligned} \frac{\partial D_i}{\partial x_1} &= \frac{(1-u_{xi}^2)\Delta_{xi} - u_{xi}(\Delta_{zi}u_{zi} + \Delta_{yi}u_{yi})}{D_i} \\ \frac{\partial D_i}{\partial y_1} &= \frac{(1-u_{yi}^2)\Delta_{yi} - u_{yi}(\Delta_{zi}u_{zi} + \Delta_{xi}u_{xi})}{D_i} \\ \frac{\partial D_i}{\partial u_{xi}} &= \frac{(\Delta_{zi}^2 - \Delta_{xi}^2)u_{xi} + \frac{\Delta_{yi}\Delta_{zi}u_{yi}u_{xi}}{u_{zi}} + \frac{\Delta_{xi}\Delta_{zi}u_{xi}^2}{u_{zi}} - \Delta_{xi}\Delta_{zi}u_{zi} - \Delta_{xi}\Delta_{yi}u_{yi}}{D_i} \\ \frac{\partial D_i}{\partial u_{yi}} &= \frac{(\Delta_{zi}^2 - \Delta_{yi}^2)u_{yi} - \Delta_{yi}\Delta_{zi}u_{zi} + \Delta_{yi}\Delta_{zi}\frac{u_{yi}^2}{u_{zi}} + \Delta_{xi}\Delta_{zi}\frac{u_{xi}u_{yi}}{u_{zi}} - \Delta_{xi}\Delta_{yi}u_{xi}}{u_i}. \end{aligned} \tag{3.26}$$

The remaining partial derivatives values of $(\partial D_i/\partial x_2)$ and $(\partial D_i/\partial y_2)$ are then straightforward obtained from the previous step. This yields:

$$\frac{\partial D_i}{\partial x_2} = \frac{\partial D_i}{\partial u_{xi}}.\frac{\partial u_{xi}}{\partial x_2} + \frac{\partial D_i}{\partial u_{yi}}\frac{\partial u_{yi}}{\partial x_2} = \frac{\partial D_i}{\partial u_{xi}}.\frac{1-u_{xi}^2}{Q} - \frac{\partial D_i}{\partial u_{yi}}.\frac{x_2 y_2}{Q^3} \tag{3.27}$$

$$\frac{\partial D_i}{\partial y_2} = \frac{\partial D_i}{\partial u_{xi}}.\frac{\partial u_{xi}}{\partial y_2} + \frac{\partial D_i}{\partial u_{yi}}.\frac{\partial D_{yi}}{\partial y_2} = -\frac{\partial D_i}{\partial u_{xi}}.\frac{x_2 y_2}{Q^3} + \frac{\partial D_i}{\partial u_{yi}}.\frac{1-u_{yi}^2}{Q}, \tag{3.28}$$

with

$$Q = x_2^2 + y_2^2 + 1 \tag{3.29}$$

Using the equations in 3.19, Q can be expressed in the form:

$$Q = \frac{1}{u_z^2} \tag{3.30}$$

Finally, once all the parameters have been found, the error propagation with the no-negligible values of σ_i is obtained by simply implementing all of them in the

equation (3.18).
The complete procedure is re-iterated until convergence is reached. Before each iteration track parameters and error matrices are translated to current vector position. It should be noted that the procedure of the charged track selection for the conversion criteria is iterated till a displacement of the order $0.01\mu m$ or less is seen on the computed slope of the secondary vertex position.
As a conclusion, the method is based on maximizing the Secondary vertex probability (or minimizing the χ^2) derived from the vertex fits for a permutation of possible two track associations. Within the mathematical framework, the position of the conversion point is then given by the equation (3.14).

3.7.2 Application of the SV method to the reconstruction of the conversion point

The determination of the Secondary vertex point manifest through the mathematical configuration presented in the previous section. In all what follows, we will consider the uncertainties as constant variables. As a consequence, here we make a direct application for the photon conversion point which is identified by the following sequence.

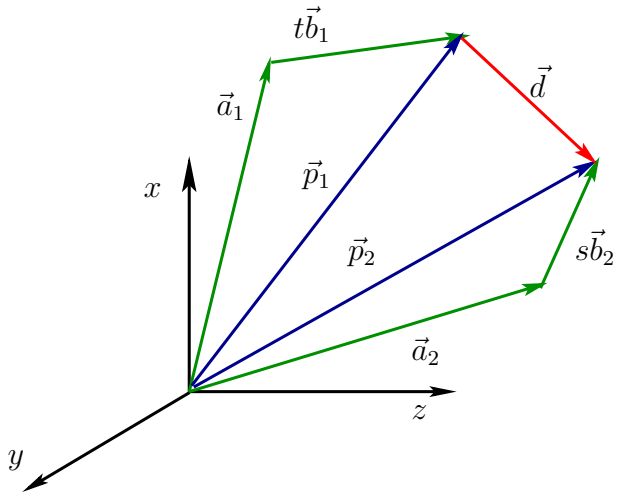

Figure 3.12: Scheme of the method to reconstruct the conversion point.

Assume we have the two electrons vectors expressed as:

$$\begin{cases} \vec{p_1} = \vec{a}_1 + t.\vec{b}_1 \\ \vec{p_2} = \vec{a}_2 + s.\vec{b}_2 \end{cases} \tag{3.31}$$

we consider the distance vector $\vec{d_i}$ between $\vec{p_1}$ and $\vec{p_2}$, that means:

$$\vec{d_i} = u(\vec{b}_1 \times \vec{b}_2) \Leftrightarrow \vec{d_i} \perp \vec{b}_1 \quad \text{and} \quad \vec{d_i} \perp \vec{b}_2 \tag{3.32}$$

In addition one can get (see figure 3.12):

$$\vec{p_1} + \vec{d_i} = \vec{p_2} \tag{3.33}$$

$$\vec{a}_1 + t.\vec{b}_1 + u(\vec{b}_1 \times \vec{b}_2) = \vec{a}_2 + s.\vec{b}_2 \tag{3.34}$$

which yields:

$$\vec{a}_1 - \vec{a}_2 = s\vec{b}_2 - t\vec{b}_1 + u(\vec{b}_2 \times \vec{b}_1) \tag{3.35}$$

By re-writting the equation (3.35) in the matricial form:

$$\begin{pmatrix} b_{2x} & -b_{1x} & (\vec{b}_2 \times \vec{b}_1)_x \\ b_{2y} & -b_{1y} & (\vec{b}_2 \times \vec{b}_1)_y \\ b_{2x} & -b_{1z} & (\vec{b}_2 \times \vec{b}_1)_z \end{pmatrix} \begin{pmatrix} s \\ t \\ u \end{pmatrix} = \begin{pmatrix} a_{1x} - a_{2x} \\ a_{1y} - a_{2y} \\ a_{1z} - a_{2z} \end{pmatrix} \tag{3.36}$$

The goal is to determine (s, t, u) vector components. The system of linear equations in (3.36) can be solved by using Cramer's rule in terms of determinants. That read,

$$s = \frac{det\mathbf{S}}{det\mathbf{A}}, \quad t = \frac{det\mathbf{T}}{det\mathbf{A}}, \quad u = \frac{det\mathbf{U}}{det\mathbf{A}} \tag{3.37}$$

with:

$$det\mathbf{A} = \begin{vmatrix} b_{2x} & -b_{1x} & (\vec{b}_2 \times \vec{b}_1)_x \\ b_{2y} & -b_{1y} & (\vec{b}_2 \times \vec{b}_1)_y \\ b_{2x} & -b_{1z} & (\vec{b}_2 \times \vec{b}_1)_z \end{vmatrix} \tag{3.38}$$

$$det\mathbf{S} = \begin{vmatrix} a_{1x} - a_{2x} & -b_{1x} & (\vec{b}_2 \times \vec{b}_1)_x \\ a_{1y} - a_{2y} & -b_{1y} & (\vec{b}_2 \times \vec{b}_1)_y \\ a_{1z} - a_{2z} & -b_{1z} & (\vec{b}_2 \times \vec{b}_1)_z \end{vmatrix} \tag{3.39}$$

$$det\mathbf{T} = \begin{vmatrix} b_{2x} & a_{1x} - a_{2x} & (\vec{b}_2 \times \vec{b}_1)_x \\ b_{2y} & a_{1y} - a_{2y} & (\vec{b}_2 \times \vec{b}_1)_y \\ b_{2z} & a_{1z} - a_{2z} & (\vec{b}_2 \times \vec{b}_1)_z \end{vmatrix} \tag{3.40}$$

$$det\mathbf{U} = \begin{vmatrix} b_{2x} & -b_{1x} & a_{1x} - a_{2x} \\ b_{2y} & -b_{1y} & a_{1y} - a_{2y} \\ b_{2z} & -b_{1z} & a_{1z} - a_{2z} \end{vmatrix} \tag{3.41}$$

Consequently, the Secondary vertex point is just pointed out by the vector $\vec{p}_{12}$ expressed by the following equation:

$$\vec{p}_{12} = \vec{p}_1 + \frac{1}{2}\vec{d}_i \tag{3.42}$$

$$= \vec{p}_1 + \frac{1}{2}(\vec{p}_1 - \vec{p}_2). \tag{3.43}$$

Any vector of the electron/postiron detected by the TPC and expressed by the equation (3.31) is then computed by the coordinates ($Xline0$,$Yline0, 0$).
The (x_2, y_2) slopes that are defined in the previous section with $z = 0$ are equivalent to the $\vec{s}$ slope in the X-Z plane (for x_2) and Y-Z plan (for y_2). They are obtained by the $Xline1$ and $Yline1$ values of the TPC track. The latter two parameteres are used to measure the local angles defined in the equations (2.13) and (2.14).

3.7.3 Selection of γ conversions in the RICH2 mirror

Since our concern is to reconstruct the photons that converts in the RICH2 mirror position, we select them by making a cut on reconstructed conversion point. It was possible to enhance the extracted photon signal by the *ThetaEP* cut described in Section (3.5). It has a powerful support to reduce the background and to improve the significance.

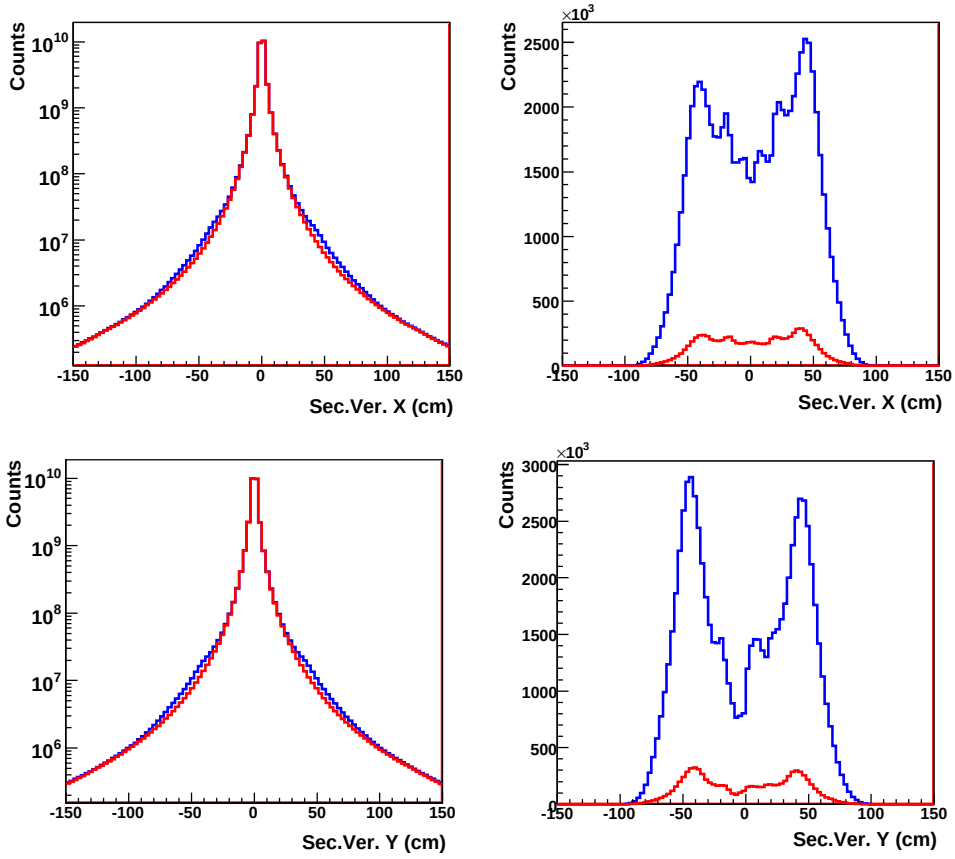

Figure 3.13: The Secondary Vertex distributions of the photons candidates. The reconstructed photons from the unlike sign pairs (e^-e^+) are in blue and the like sign pairs (e^-e^- + (e^+e^+) in red. The top two plots correspond to the X coordinates of the Secondary Vertices distributions before (left) and after (right) the ThetaEP cut function while on the bottom two plots, the same distributions for the Y coordinates before and after the ThetaEP cut function.

This can be seen by checking the reconstructed secondary vertices distributions

in the X,Y and Z axis. It is explicitly verified on the X and Y axis shown in figure (3.13) after and before the *ThetaEP* cut. Additionally, more check can be performed corresponding the projection of the distribution on the X-Y plane illustrated in figure (3.14). The highly concentrated distribution represents the location of the photon conversion point in the phase-space.

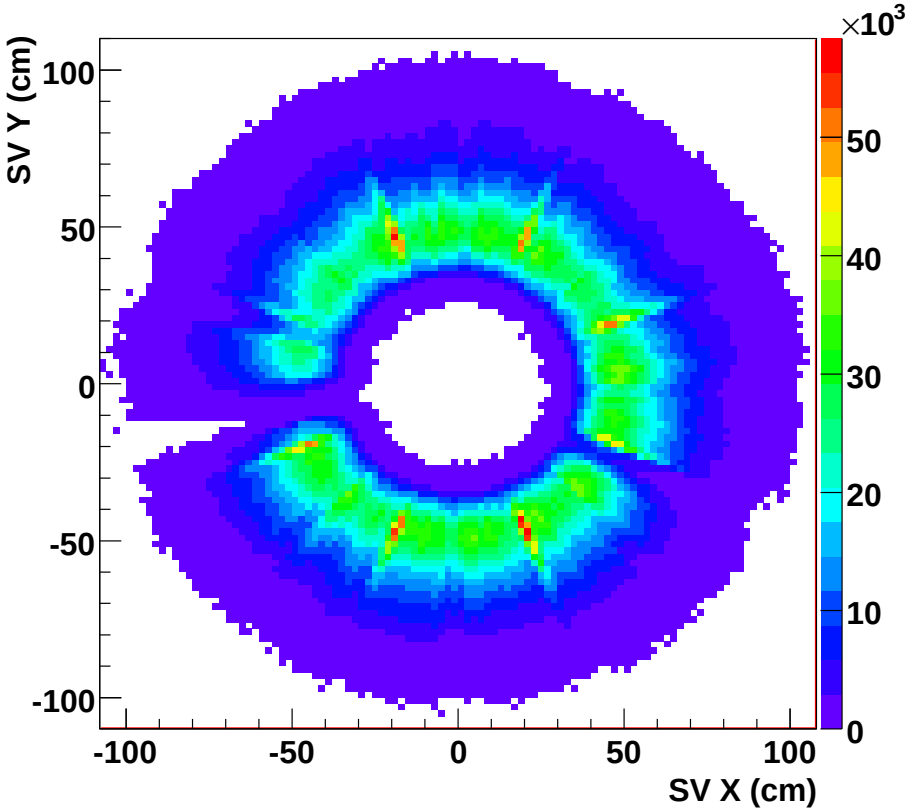

Figure 3.14: The distribution of X vs Y position of the reconstructed conversion point. On top of the homogeneous distribution comming from the RICH2 mirror, the γ-fold structure from the TPC entrance window is clearly visible.

A similar situation along the Z axis is presented separately, where the most significantly photons distribution are very clear. This is shown in figure (3.15). From this one finds that reconstructed photons are concentrated in the RICH2 mirror region. This is expected since the RICH2 mirror is main converter.

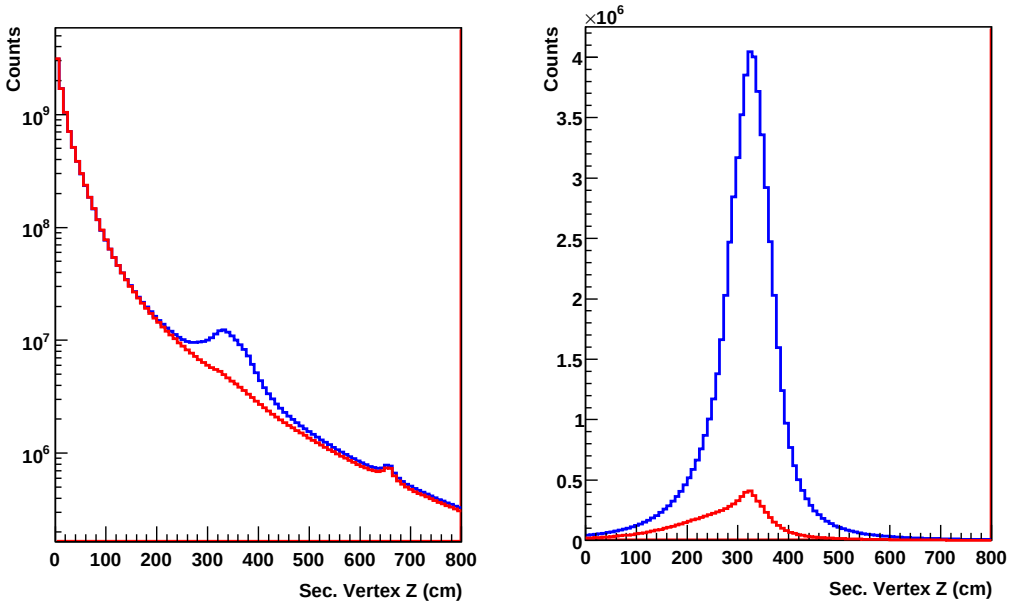

Figure 3.15: The Z direction of the Secondary Vertex distributions of the photon candidates before (left) and after (right) imposing the ThetaEP cut for unlike-sign pairs (blue) and like-sign pairs (red).

By following the previous steps discussed above, More precise tuning is now needed and may give further improvement to select the photons at the RICH2M position. The Secondary Vertex cut (SV) can be comfortably performed at $\mu \pm 2\sigma$. After extensive verification that no photons information was being originated from other locations, by keeping the SV cut in all the accumulated analysis, the Secondary Vertex distributions from the contributions of the unlike and like sign pairs investigated as function of the photon momentum (see figure (3.18)). The used requirement is a major benefit from the SV cut which has been studied depending on the momentum of the photons. This study can be explored in figure (3.17). The location of the extracted photon signal is substantially present at the RICH2 converter and fitted with Gaussian function. This confirms that the used technique to determine the conversion point of the photons is equivalent to our expectations where they should be occurring.

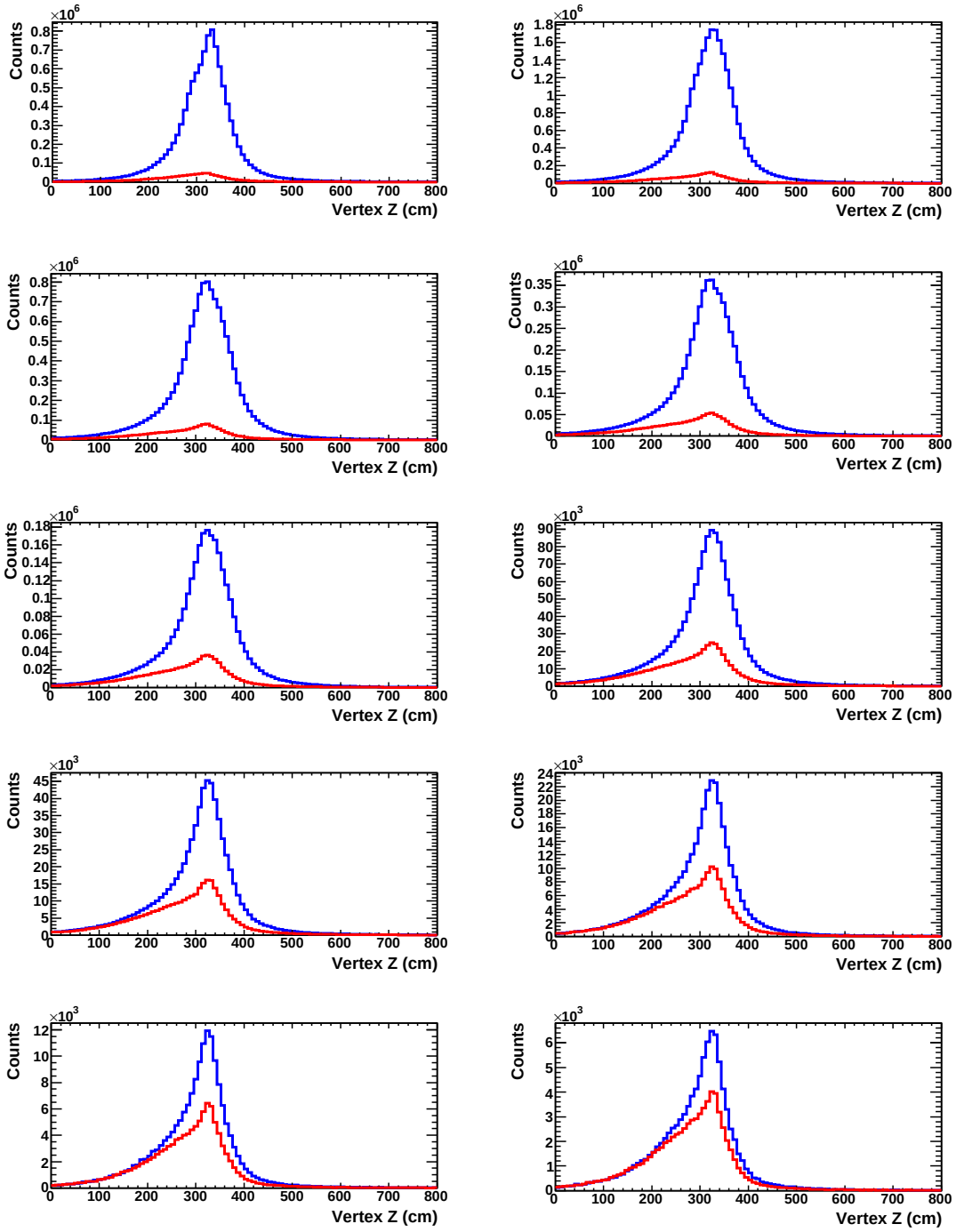

Figure 3.16: The measured Z position of the Secondary Vertex distributions after the ThetaEP cut function as function of the photon momentum for unlike-sign pairs (blue) and like-sign pairs (red).

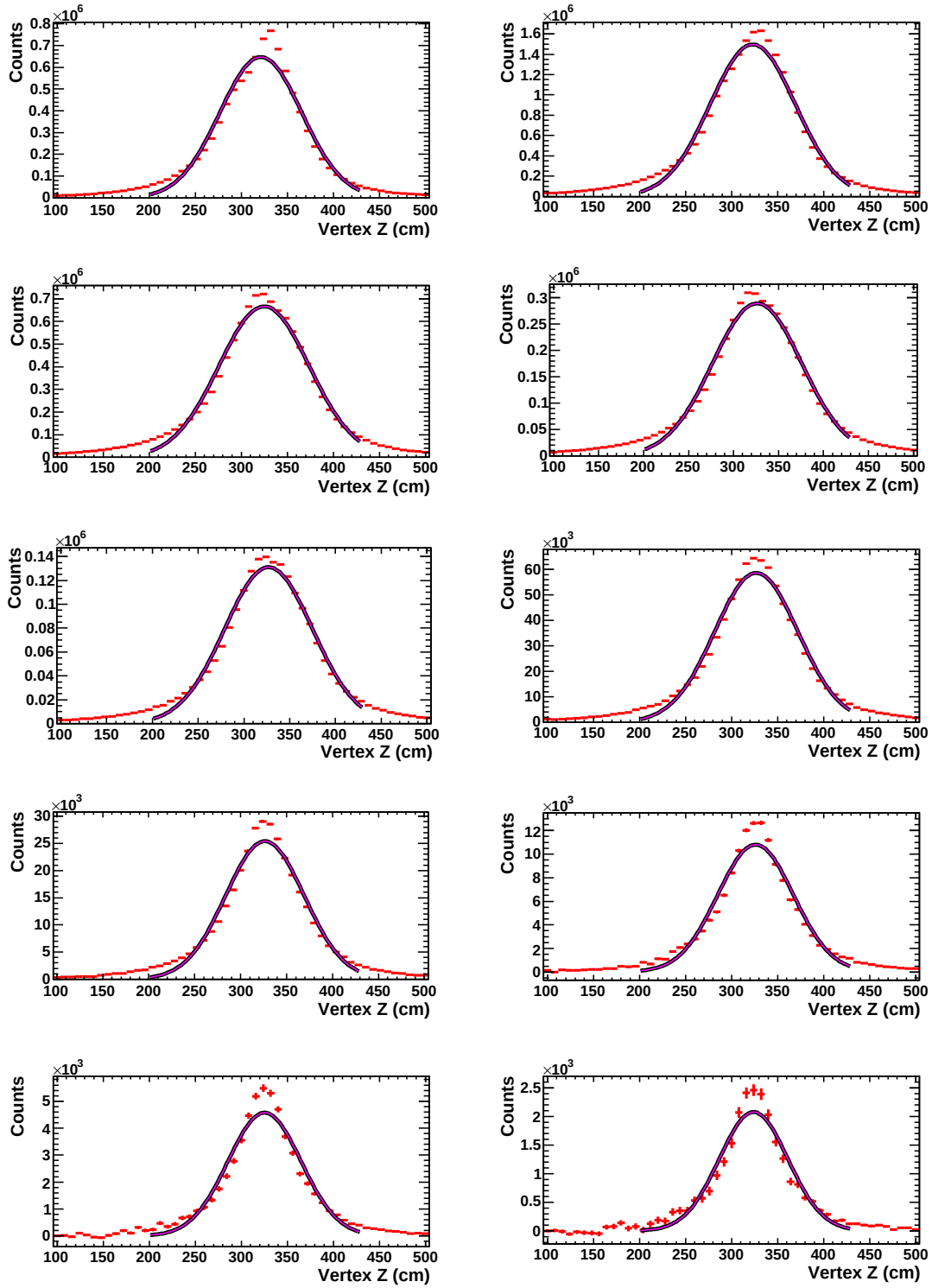

Figure 3.17: The extracted signal Z position distribution of the photon conversion point Vs the momentum of the photon fitted with a Gaussian.

The mean of the Gaussian fit refers to the photon conversion point as function of their momentum. The stability of the mean values indicates the well reconstructed photons candidates which will be used next to the neutral pion reconstruction. The width of the distributions is dominated by the angular resolution of the opposed charged tracks. A detailed study of the photon conversion point for both the position and the width as a function of the theta angle is shown in figure (3.18). These values are used for the secondary vertex cut in the analysis.

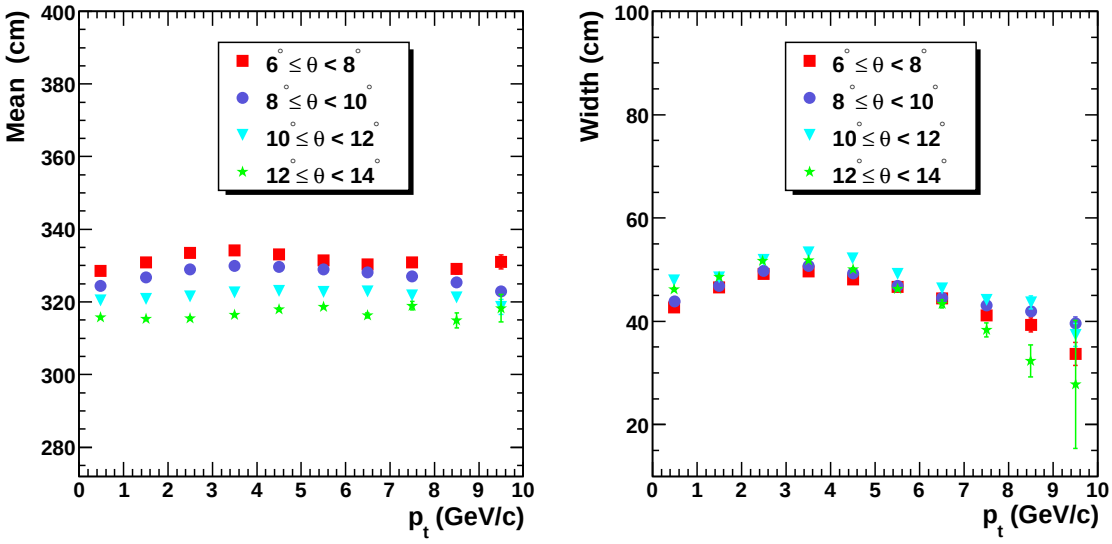

Figure 3.18: The mean (left) and the width (right) of the fitted Secondary vertex distribution Vs the photon momentum.

3.8 The π^0 reconstruction

This section is dedicated to describe the reconstruction of π^0 from $\gamma\gamma$ decay. The produced π^0 decays into a pair of photons with branching ratio 98.8% making it the most convenient decay channel for π^0 reconstruction.

3.9 The mixing event method

Experimentally we are dealing some times with instable particles which have a very short life time, or discussing the statistical analysis of data which direct to the final event analysis, in these cases we are beyond multiple paths that lead from the detection digitizing to physics information.
During the an ultra-relativistic collision, a pair of electrons/positrons (i.e the same signs) do not come from the same photon, however they might issued from a coincidence events. Each electron (positron) combines with positron (electron) of opposite charge to form one photon. However the extraction of photon signal is reproduced by using the distribution of electrons and positrons taken from different event of similar multiplicity.
The obtained photons distributions after subtracting the background are then used to build the neutral pion mesons distribution. This approach of the subtraction of combinatorial background is called the mixed event method [88, 89]. The idea of mixed event method is based on the combination of the uncorrelated two different photons. The superposition of the two photon pairs from the same and mix events is what define to us the signal and the combinatorial background [90].

Figure (3.19) shows the principle of the mixed event technique. The applied track selection is the same for all the recorded events in order to reproduce correctly the combinatorial background. Each combination for a certain event i between X_i and Y_i is taken into account after passing all the global criteria cuts. The yield will form the real distributions needed later to extract the signal. This step is repeated over all the number of events(n).
Another correlation of X and Y particles which can be happened numerically but it will not be taken into account physically since it is considered as background. All the combinations X_i and Y_i, Y_{i-1}, Y_{i-2}, ...,Y_{i-n} or Y_i and X_i, X_{i-1}, X_{i-2}, ...,X_{i-n} are counted by the mixing between the different events.
Chronologically, after each event, the selected $X-Y$ combinations are stored in an array.

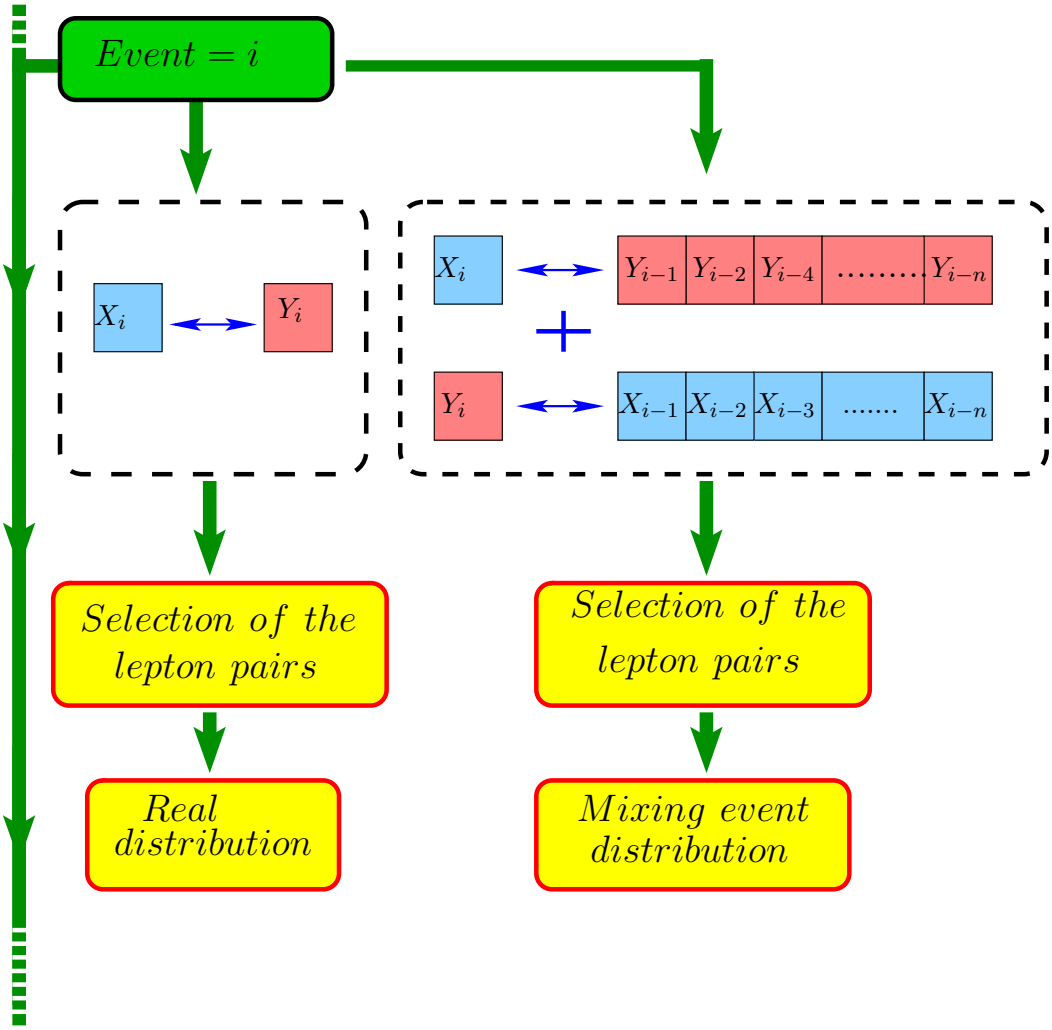

Figure 3.19: Principle of operation of the event mixing method.

3.9.1 Invariant mass analysis

The $\gamma\gamma$ invariant mass is defined by the 4-momentum absolute value. The energy and the opening angle of the two photons (zero mass) are the main kinematic variables to perform the invariant mass analysis. The invariant mass of the two photons originating from the neutral pion decay is identical to the neutral pion rest mass of 134.9766 MeV/c^2 [84]. The reconstruction of π^0 is twofold problem. The first one was the reconstruction of the γ already described. For this analysis only photons with p^t larger than 0.150 GeV/c were used. Then π^0's are found. The invariant mass of particle pair is expressed by the momentum as .

$$p_{12} = p_{\gamma 1} + p_{\gamma 2} \tag{3.44}$$

The invariant mass expression of $\pi^0 \longrightarrow \gamma\gamma$ is found by taking the $p = (p_0, p_1, p_2, p_3) = (E, p_x p_y p_z)$ and taking the metric base $diag\ g_{\mu\nu} = (1, -1, -1, -1)$. The $E = p$ for the photons. This reads:

$$\begin{aligned} M^2_{\pi^0} &= 2E_{\gamma 1}E_{\gamma 2}(1 - \cos\theta) \\ &= 2|\overrightarrow{p_{\gamma 1}}||\overrightarrow{p_{\gamma 2}}|(1 - \cos\theta) \\ \Longrightarrow M_{\pi^0} &= \sqrt{2|\overrightarrow{p_{\gamma 1}}||\overrightarrow{p_{\gamma 2}}|(1 - \cos\theta)} \end{aligned} \tag{3.45}$$

where θ_{12} is the opening angle between the two photons.

The Mixing event

Once the "good" photons are identified, the invariant mass analysis of π^0 cannot be identified uniquely since all possible photon-photon combinations have to be considered. The procedure of event mixing method is widely used to determine the combinatorial background. The mixed event is determined by taking all photon candidates from an event and combining them with the photons from different events. By this way the mixed event distribution is determined in the case of the π^0 invariant mass.

The Armenteros Podolanski plots

In order to verify if there is any cross decay channels with the π^0 peak which can missidentify the mass, we study the Armenteors-Podolanski plot [91].

The variables of the Armenteors-Podolanski technique are the p_{TA} which is the projection of one of the two photon momentum (daughters) on the flight direction of the neutral pion (parent). Considering M as the mother particle mass (π^0) which

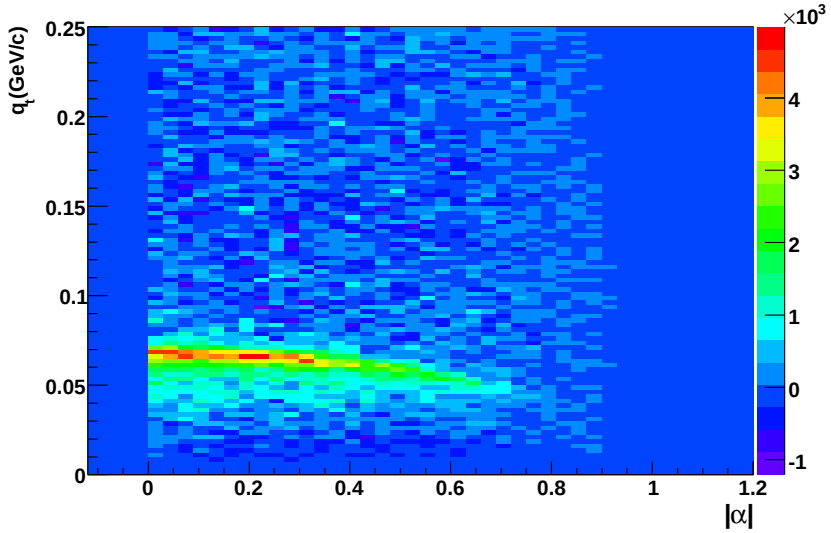

Figure 3.20: The Armenteros-Podolanski distribution of q_t Vs $|\alpha|$ for the π^0 signal for all the π^0 transverse momentum and rapidity range.

decay into two photons. In the center of mass reference frame, we denote all the kinematic quantities with the index $*$. Thus the momentum of each particle (mother or daughter) can be presented as:

$$\vec{p_i^*} = \gamma \vec{p_i^*} + \vec{\beta}\gamma E_i^* \tag{3.46}$$

From the momentum conservation in the center of mass reference frame, we have $\parallel \vec{p_1^*} \parallel = \parallel \vec{p_2^*} \parallel = p^*$. The two vectors $\vec{p_1^*}$ and $\vec{p_2^*}$ refers to the daughters momentum γ_1 and γ_2 respectively. One can write the two momentum components in the flight and transverse direction of the mother particle (π^0) as:

$$\begin{cases} p_{i\parallel}^* = \gamma . p^* . \cos\theta^* + d . \beta\gamma E_i^* \\ p_{i\perp}^* = p^* . \sin\theta^* \end{cases} \tag{3.47}$$

where for $i = 1 \Rightarrow d = 1$ and for $i = 1 \Rightarrow d = -1$. The angle θ^* is define as $\theta^* = (\widehat{\vec{p^*}, \vec{p_1^*}})$ which is the angle between the mother particle and one of the daughter particles. By using another parameter α that can be defined by the momentum projections of the photons on the direction of the π^0 meson. This can be simply expressed as:

$$\alpha = \frac{p^*_{1\parallel} - p^*_{2\parallel}}{p^*_{1\parallel} + p^*_{2\parallel}} \tag{3.48}$$

From the equation (3.47), the α value can be rewritten as:

$$\alpha = \frac{2p^*}{\beta M}.\cos\theta^* + \frac{E^*_1 - E^*_2}{M} \tag{3.49}$$

By putting $a_1 = \frac{2p^*}{\beta M}$ and $a_2 = \frac{E^*_1 - E^*_2}{M}$ and taking $p_{TA} = p^*_{1\perp} = p^*_{1\perp}$ we obtain:

$$\left(\frac{\alpha - a_2}{a_1}\right)^2 + \left(\frac{p_{TA}}{p^*}\right)^2 = 1 \tag{3.50}$$

The equation (3.50) means that for π^0 moving with β velocity a good reconstruction of the neutral pion mass should appears as an elliptic concentration in (p_{TA}, α) plane. This can be seen in figure(3.20). This method reinforces the suppression of the contamination of different hadrons and distinguish between them. A clear signal of the neutral pion mass is seen and there is no decay channel which can misidentify the reconstruction of the π^0 in the $\gamma\gamma$ invariant mass.

The Opening angle cut (OpG1G2)

The opening angle between the two photons has been studied as function of the pair transverse momentum. This is shown in figure (3.21). An opening cut $OpG1G2$ between the two reconstructed photons is implemented in order to reduce the combinatorial background which are coming from small opening angle photons. The magenta line indicates the implemented cut as function of the neutral pion momenta, this can be expressed as: $\mathrm{OpG1G2} = 0.2\exp(-5p_t) + 0.02$. where p_t represents the transverse momentum of the $\gamma\gamma$ pair.

The π^0 signal extraction

The combinatorial background is defined as the background level in mass distributions after imposing all the requirements on the kinematic quantities. Besides the discussed cuts, more stringent requirements are used to observe the π^0 signal. The combinatorial background depends upon the p_T distribution of the reconstructed photons.
The obtained $\gamma\gamma$ invariant mass distributions for the photons yielded from the same event and the mixing event is scanned as function of transverse momentum and rapidity ranges. This has been checked for 8 p_t bins. Each signal templates represents $0.25(GeV/c)$. We expand also the study as function of rapidity splitted in

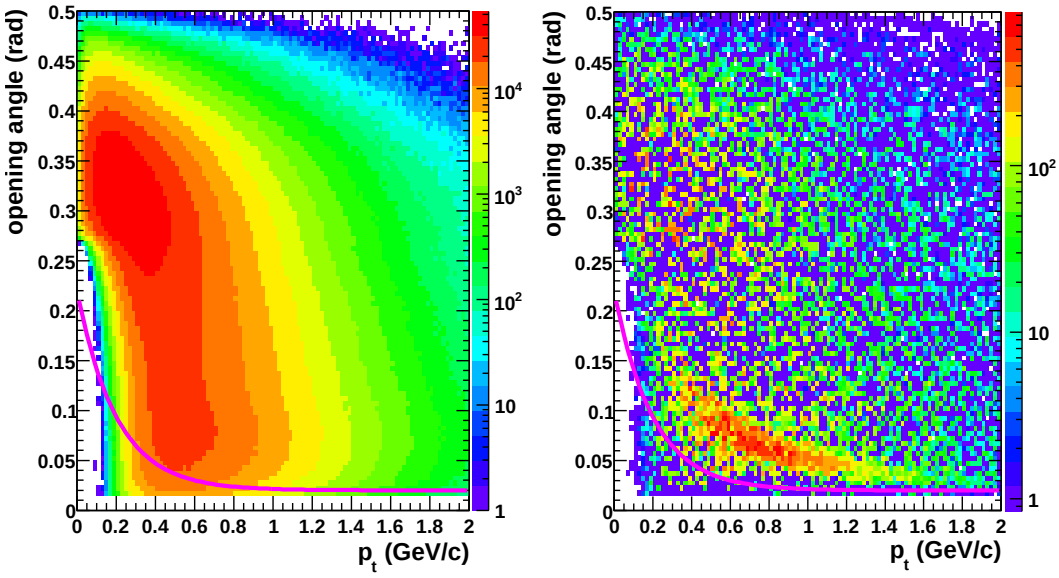

Figure 3.21: The scatter plot of the π^0 transverse momenta vs the opening angle between the two photons. The left panel indicates all the distributions coming from the same events, and right panel illustrates the subtracted distributions. The OpG1G2 cut is indicated by the magenta line in both panels.

three interval, $2.2 \leq y_1 < 2.4$, $2.4 \leq y_2 < 2.6$ and $2.6 \leq y_3 < 2.7$. In all what follows we will measure the $\gamma\gamma$ invariant mass as function of these two variables (p_t,y). An additional constraint on the second p_t bin $0.25 - 0.5$ GeV/c and the third p_t bin $0.5 - 0.75$ GeV/c along all the rapidity intervals have been required. This cut have been imposed where we require for all the photons opening angles to be larger than 0.11 rad and 0.08 rad in the transverse momentum intervals $0.25 - 0.5$ GeV/c and $0.25 - 0.5$ Gev/c respectively for the first rapidity bin y_0. In the second and third rapidity bins (y_1 and y_2) the opening angle between the two photons in $0.25 < p_t < 0.5$ GeV/c is 0.10 rad and in $0.5 < p_t < 0.75$ GeV/c is 0.07 rad. A summary of all these cuts is presented in table 3.2.

All photons that survived the previous cuts were taken in combination with each other. The resulting $\gamma\gamma$ mass distributions was used to define the π^0 signals. As it is illustrated in figures (3.22), (3.23), (3.24) the signal is well separated from the background and the π^0 mass is pointed out by the vertical line. The normalized background in red is below the peak in all the transverse momenta bins and rapidity. In the first p_t window the π^0 reconstruction efficiency is very low and no signal

Rapidity range	**Trans.Mom. (GeV/c)**	**OpAng ($\gamma\gamma$) (rad)**
y_1: 2.2 - 2.4	$0.25 < p_t < 0.5$	≥ 0.11
y_1: 2.2 - 2.4	$0.5 < p_t < 0.75$	≥ 0.08
y_2: 2.4 - 2.6	$0.25 < p_t < 0.5$	≥ 0.10
y_2: 2.4 - 2.6	$0.5 < p_t < 0.75$	≥ 0.07
y_3: 2.6 - 2.7	$0.25 < p_t < 0.5$	≥ 0.10
y_3: 2.6 - 2.7	$0.5 < p_t < 0.75$	≥ 0.07

Table 3.2: Description of the opening angle cut used as function of rapidity and momentum

is obtained for the recorded statistics.
The scale factor obtained from the ratio (real/mixed) of the invariant mass distribution will be used to normalize the mixed event background and subtract it from the real event invariant mass distributions.
The normalization factor for each p_t and rapidity is obtained by fitting the ratio of the $\gamma\gamma$ mass distribution of the real to the mixed events.
The used fit function for this purpose is gaussian function plus a constant. The constant gives the normalization factor for the mixed event background. The range of the fit is $0.08 - 0.25$ GeV/c^2 (see figures (3.25), (3.26), (3.27)).

The distributions of the invariant mass are obtained by the subtraction of the mixed event distributions from the real event distributions. The $\gamma\gamma$ invariant mass spectrum is then investigated as function of the transverse momentum and rapidity. This can be seen for each template fits for the first rapidity range $2.2 - 2.4$ in figure (3.28), for the second rapidity interval $2.4 - 2.6$ in figure (3.29) and for the last rapidity $2.6 - 2.7$ in (3.30). The signal is clearly visible in all rapidity bins and located at the π^0 mass mentioned in [84]. In the last rapidity set, the π^0 yields are too small. The presence of these signals validate the used method of the neutral pion detection. The obtained signals are fitted by a gaussian in the interval $0.05 - 1$ GeV/c.

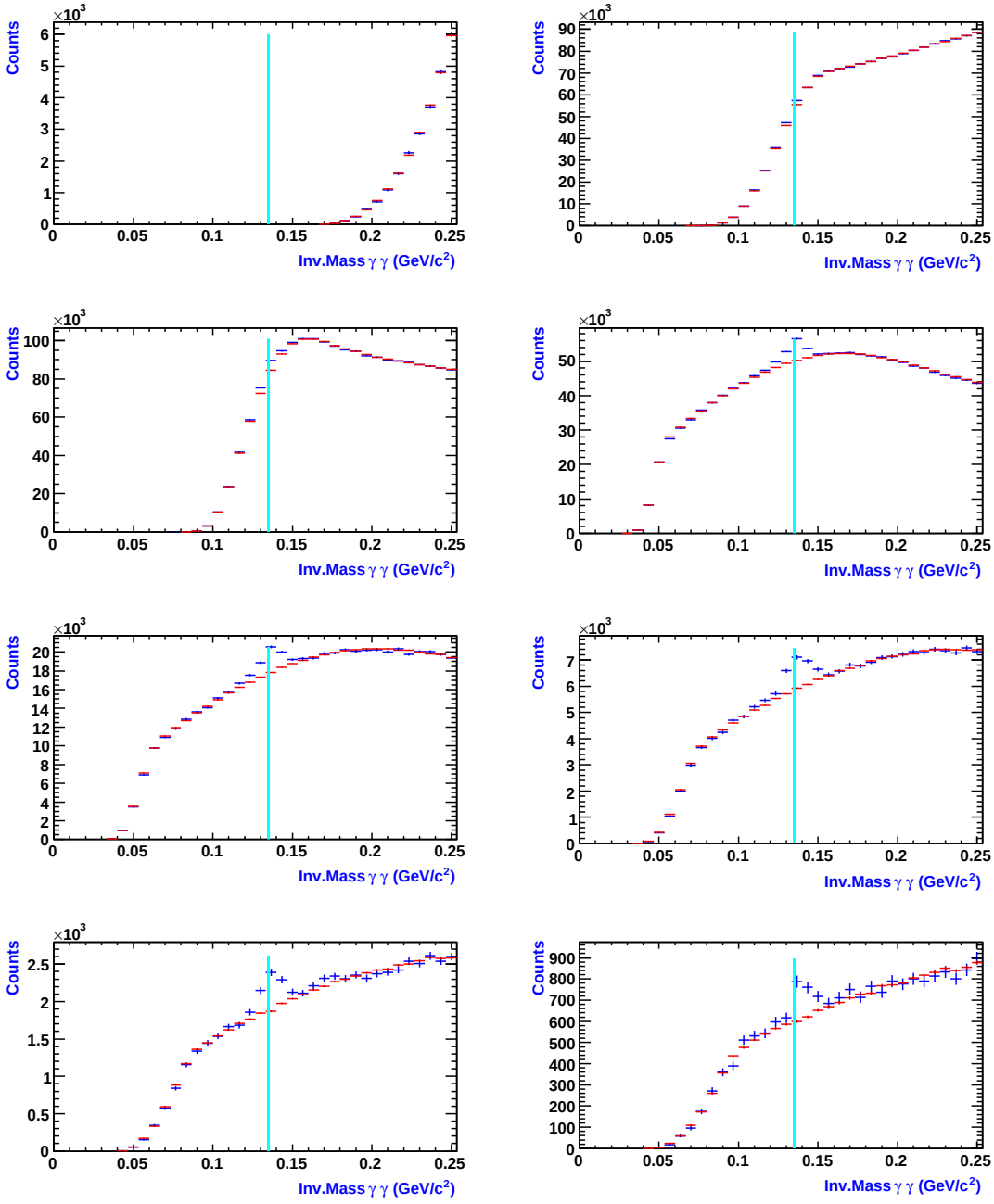

Figure 3.22: The invariant mass distribution for all the photons pairs coming from the same event (blue histogram) and from the mixing event (red histogram) after normalization for the rapidity range $2.2 \leq y < 2.4$ and 8 p_t bins of 0.25 GeV/c width.

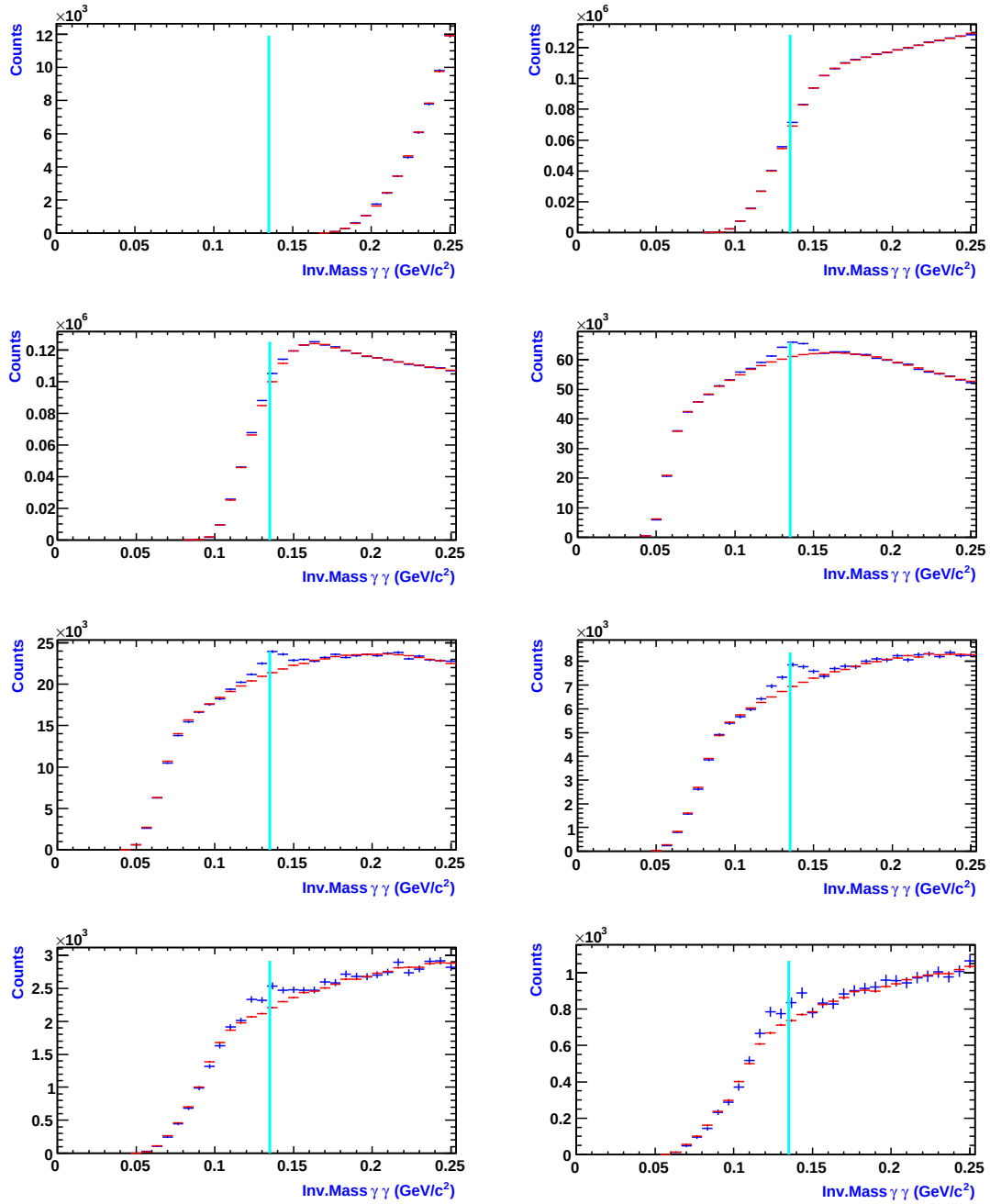

Figure 3.23: The invariant mass distribution for all the photons pairs coming from the same event (blue histogram) and from the mixing event (red histogram) after normalization for the rapidity range $2.4 \leq y < 2.6$ and 8 p_t bins of 0.25 GeV/c width.

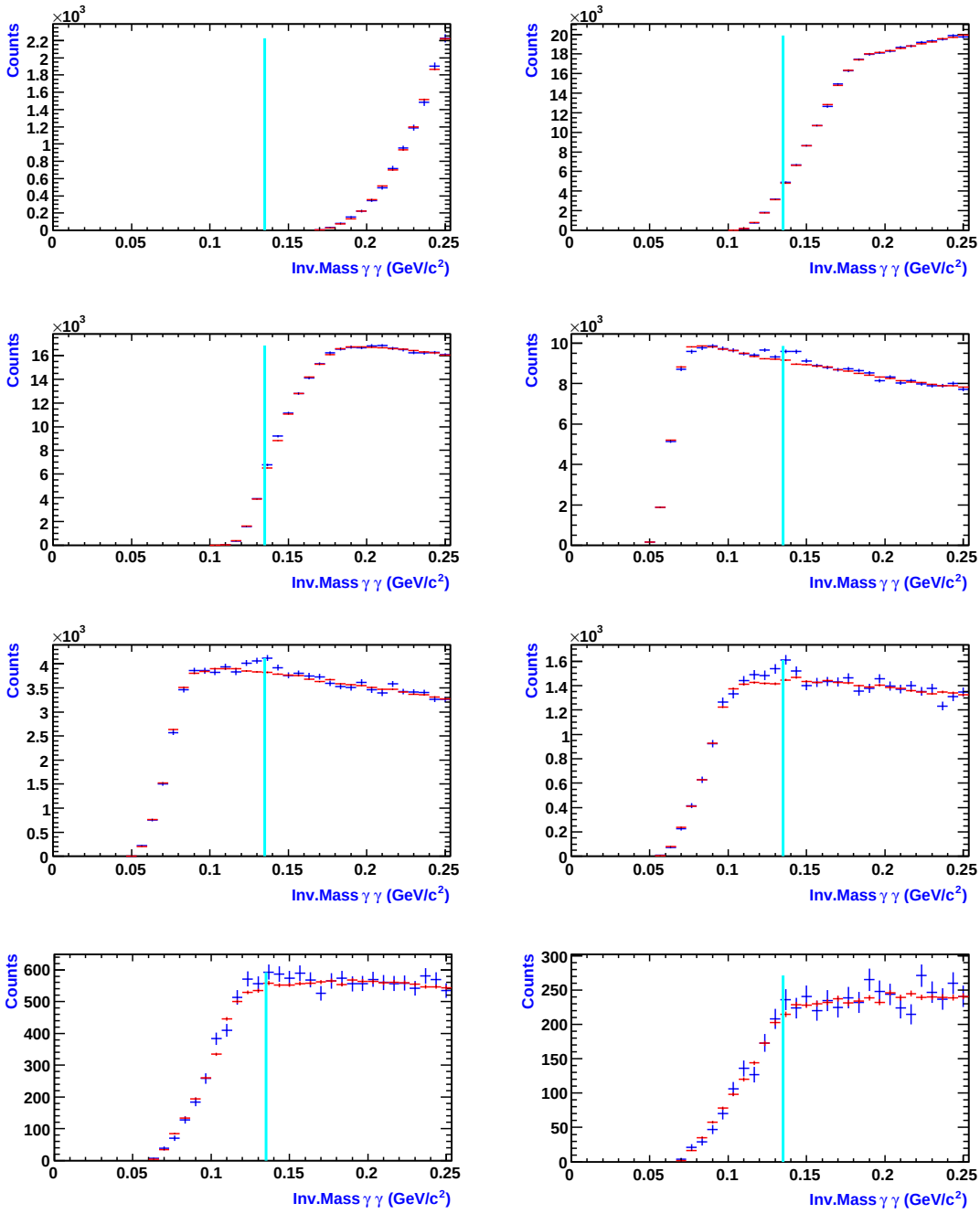

Figure 3.24: The invariant mass distribution for all the photons pairs coming from the same event (blue histogram) and from the mixing event (red histogram) after normalization for the rapidity range $2.6 \leq y < 2.7$ and 8 p_t bins of 0.25 GeV/c width.

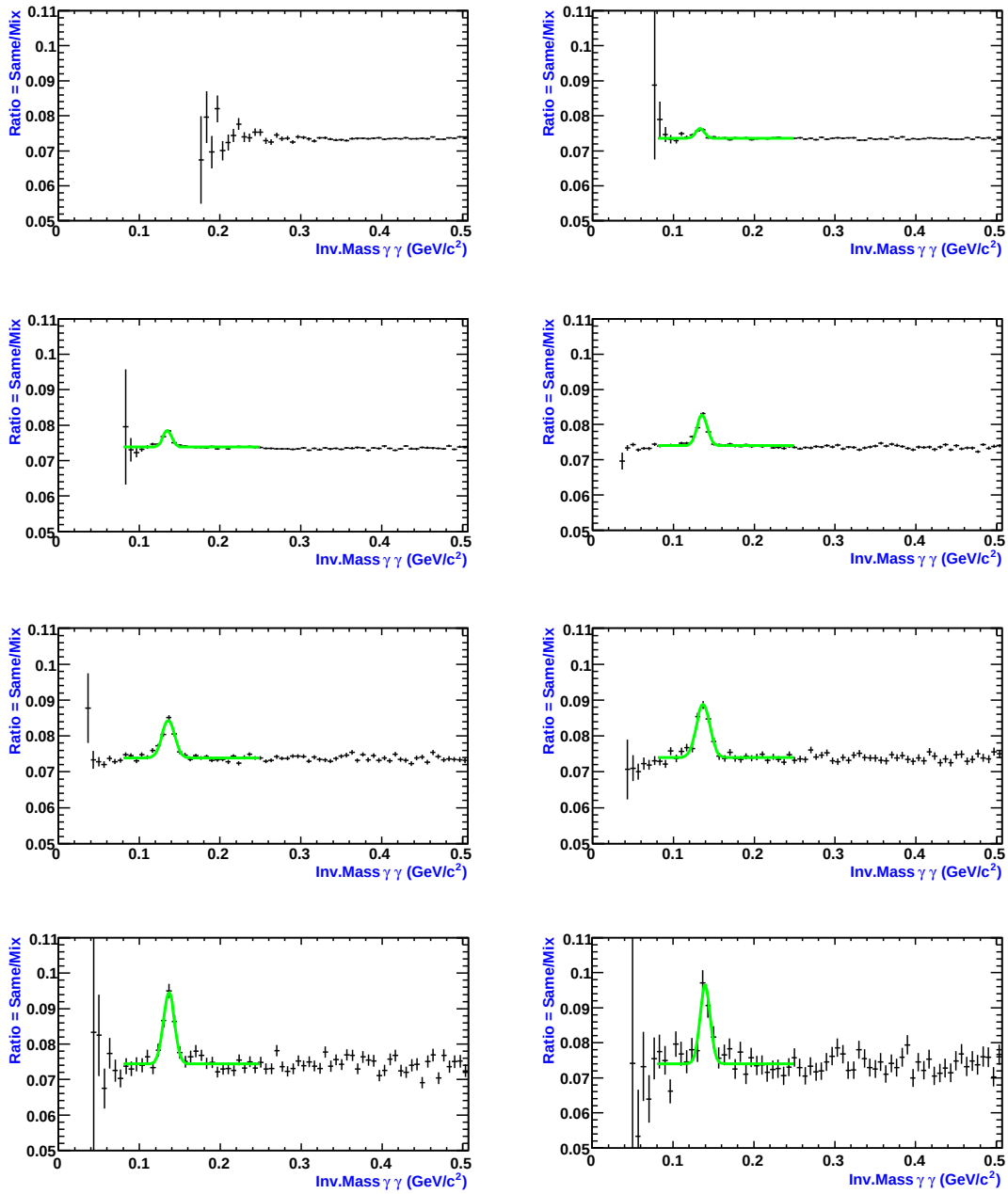

Figure 3.25: The ratio of the same and mixed events $\gamma\gamma$ mass distributions for the rapidity range $2.2 \leq y < 2.4$ and 8 p_t bins of 0.25 GeV/c width.

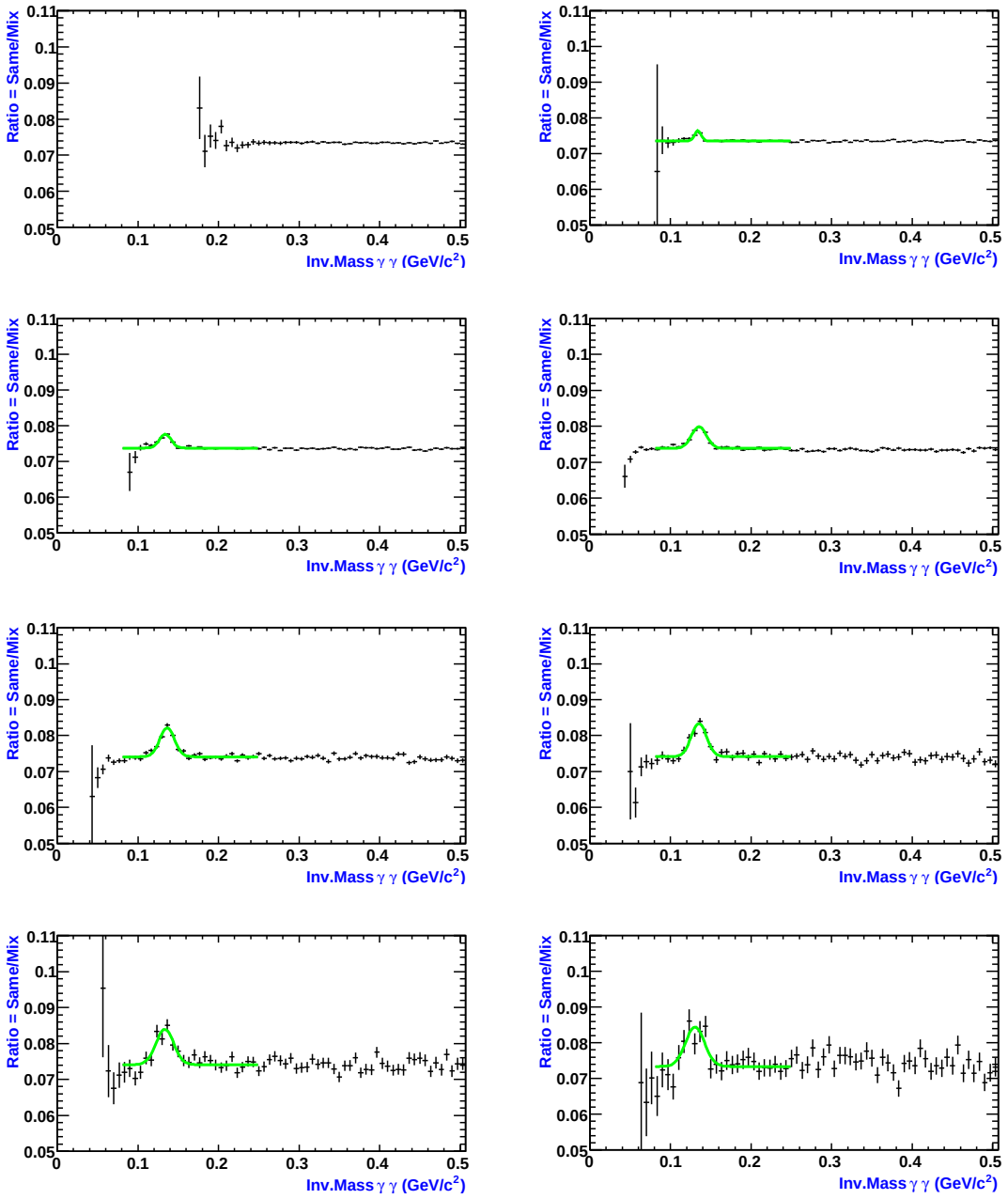

Figure 3.26: The ratio of the same and mixed events $\gamma\gamma$ mass distributions for the rapidity range $2.4 \leq y < 2.6$ and 8 p_t bins of 0.25 GeV/c width.

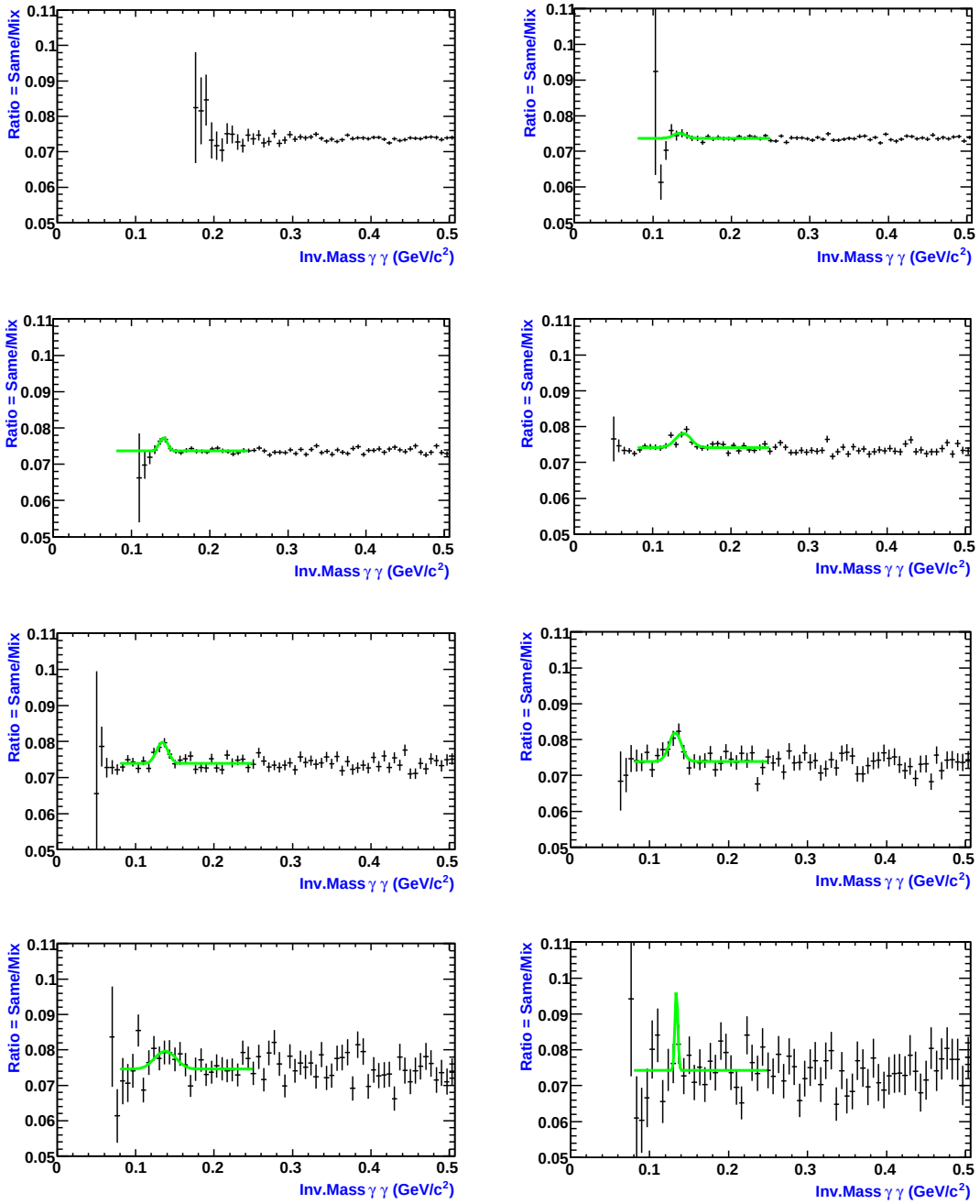

Figure 3.27: The ratio of the same and mixed events $\gamma\gamma$ mass distributions for the rapidity range $2.6 \leq y < 2.7$ and 8 p_t bins of 0.25 GeV/c width.

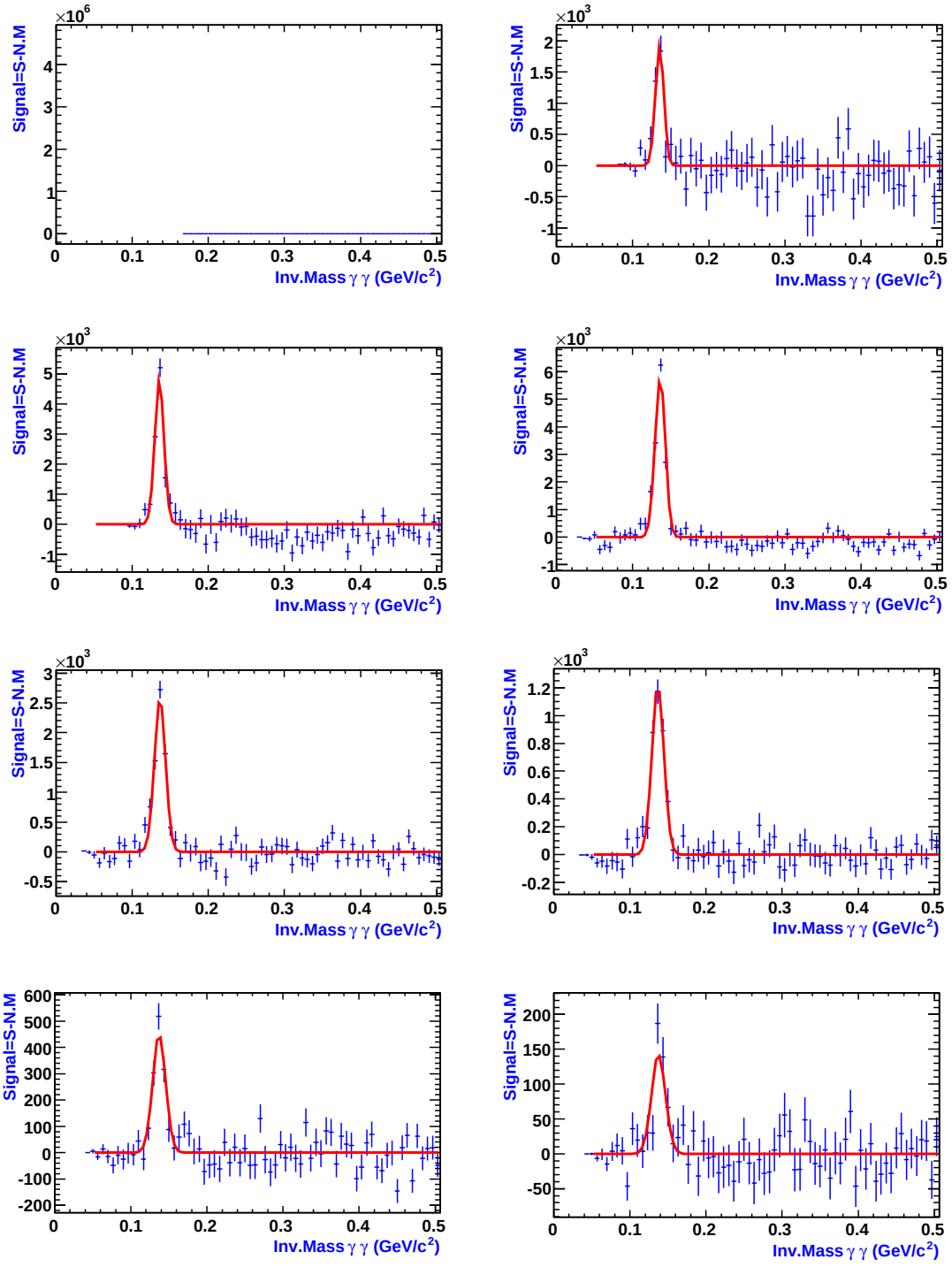

Figure 3.28: The real mass distribution of π^0 after subtracting the normalized mixed event distribution in the range $2.2 < y < 2.4$ and in 8 p_t bins of 0.25 GeV/c width.

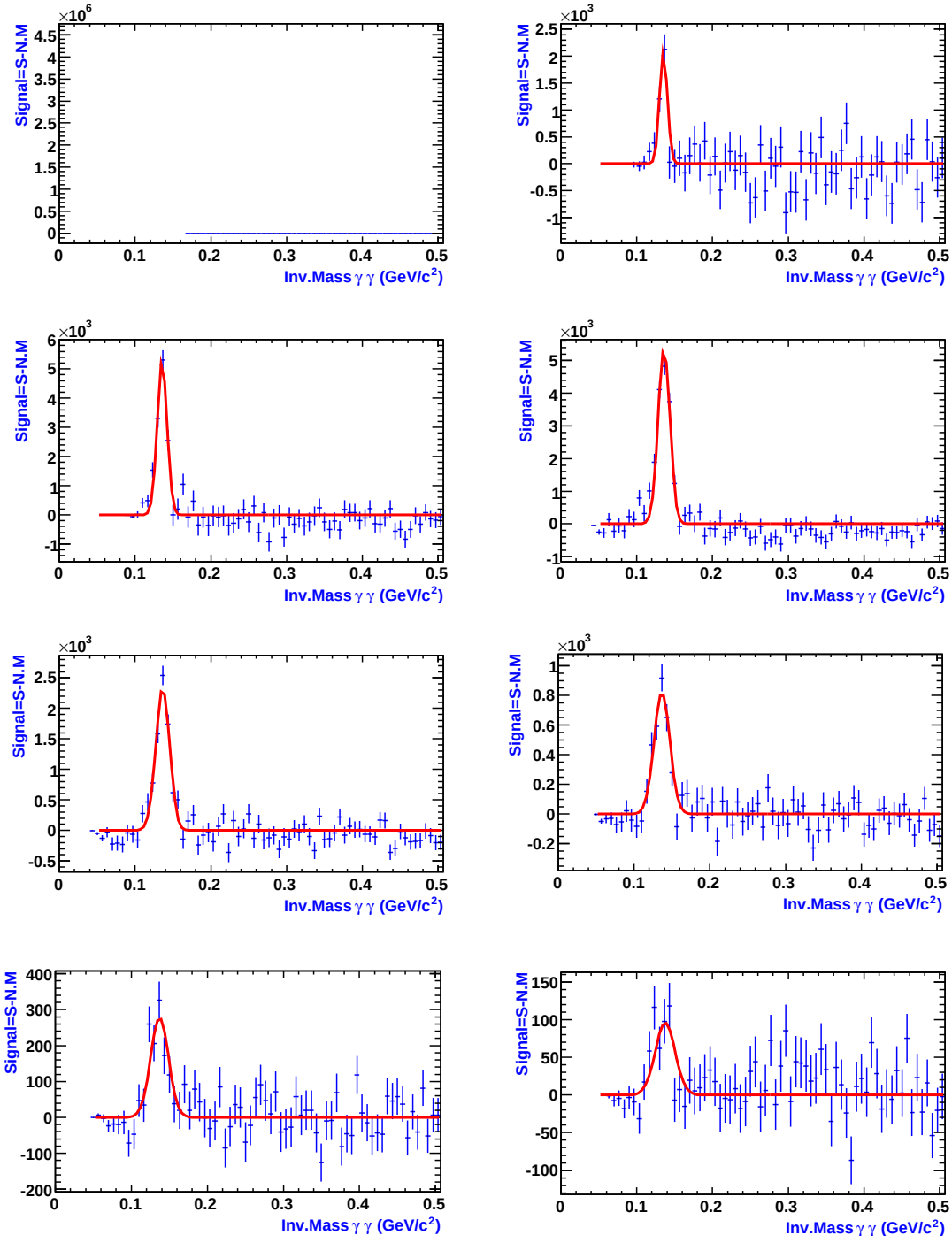

Figure 3.29: The real mass distribution of π^0 after subtracting the normalized mixed event distribution in the range $2.4 < y < 2.6$ and in 8 p_t bins of 0.25 GeV/c width.

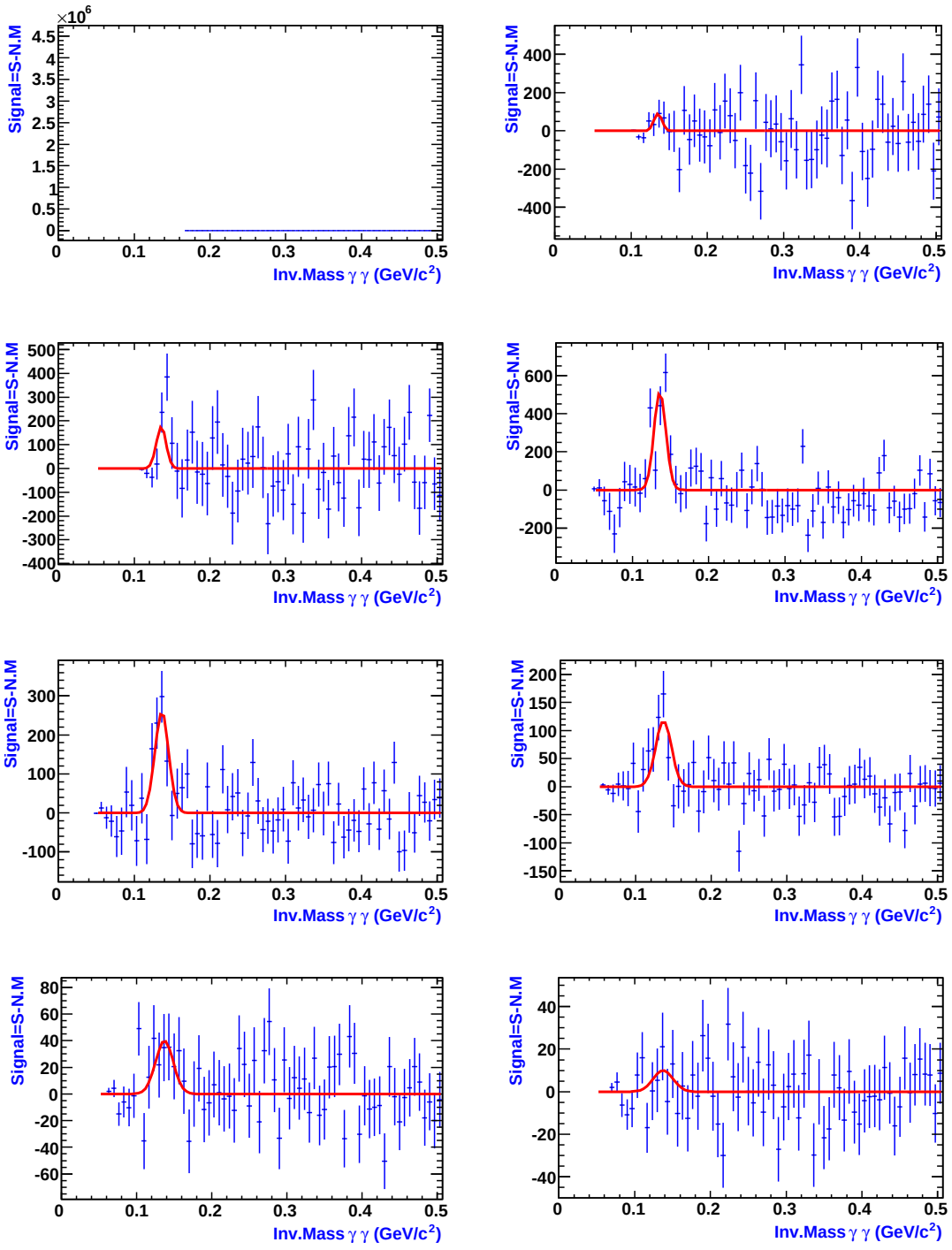

Figure 3.30: The real mass distribution of π^0 after subtracting the normalized mixed event distribution in the range $2.6 < y < 2.7$ and in 8 p_t bins of 0.25 GeV/c width.

Figure (3.31) shows the $\gamma\gamma$ invariant mass for the three rapidity ranges and the sum of them.

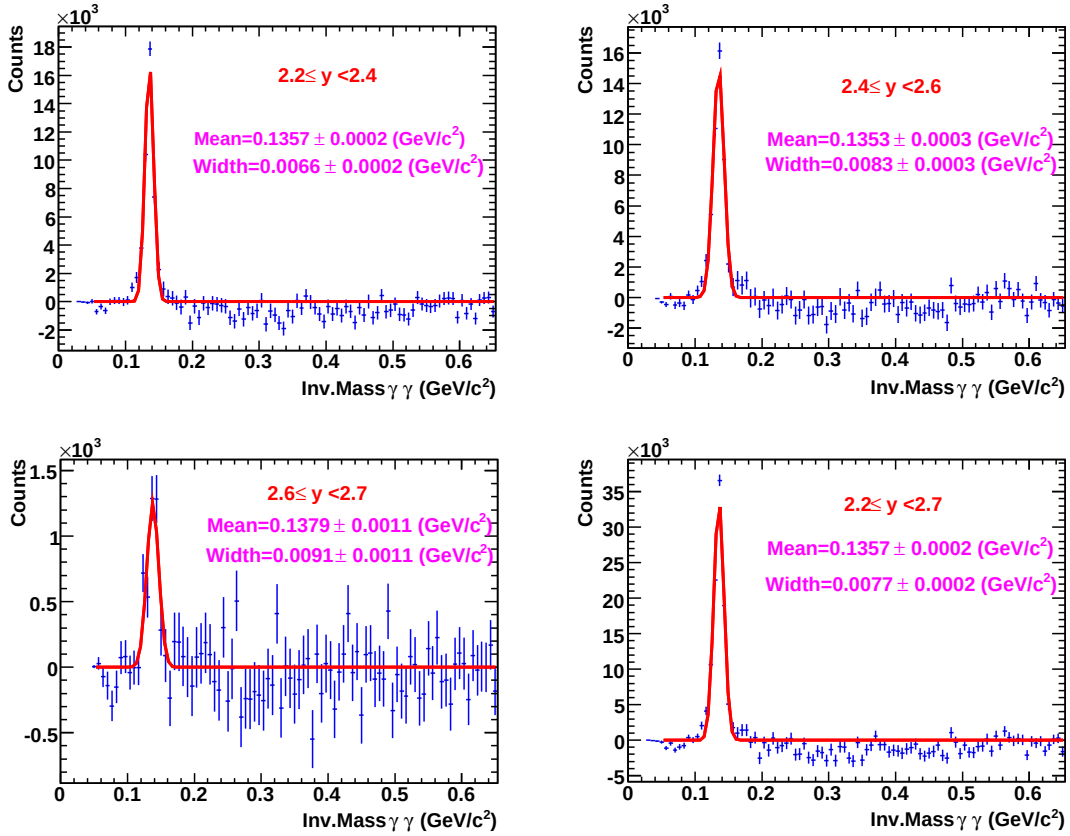

Figure 3.31: The real mass distribution of π^0 after subtracting the normalized mixed event distribution in the three rapidity ranges. In the top, left panel, for $2.2 < y < 2.4$, right panel for $2.4 < y < 2.6$. In the bottom, left panel for $2.6 < y < 2.7$, right panel for $2.2 < y < 2.7$ which corresponds to whole rapidity range taken in this analysis.

The measured peak position and the width for each rapidity range as function of π^0 momentum are illustrated in figure (3.32). The Mean of the Gaussian fit for the first two rapidities is stable along the transverse momentum, however for the last range is not stable. This can been seen also in the width. The statistical uncertainties for the last rapidity is high. This is due to the limited statistics which is not sufficient to maintain a fit with free parameters.

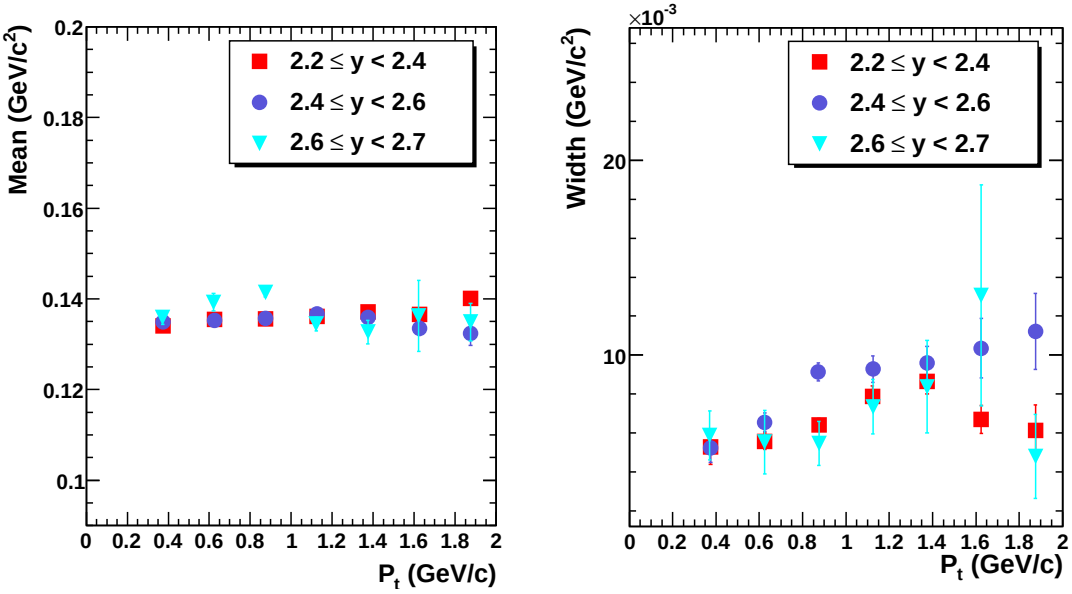

Figure 3.32: Left, the measured position of the π^0 peak as function of the π^0 transverse momentum in three rapidity bins. Right, the measured width of the π^0 peak as a function of the π^0 transverse momentum in three rapidity bins.

As a comparison, the invariant mass distribution of photon pairs for minimum bias Pb-Pb collisions from the WA98 experiment [92, 93] is illustrated in figure (3.33). The WA98 photon spectrometer consist of a large area lead-glass detector array. From the corresponding π^0 peak width as function of p_t illustrated in figure (3.34), we can say that our measurements are approximately a factor 2 better. The improvement is a result of the excellent photon energy resolution obtained with this method of photon reconstruction. The same method has been used is the STAR experiment at RICH and similar width (6 MeV/c^2) was observed [94].

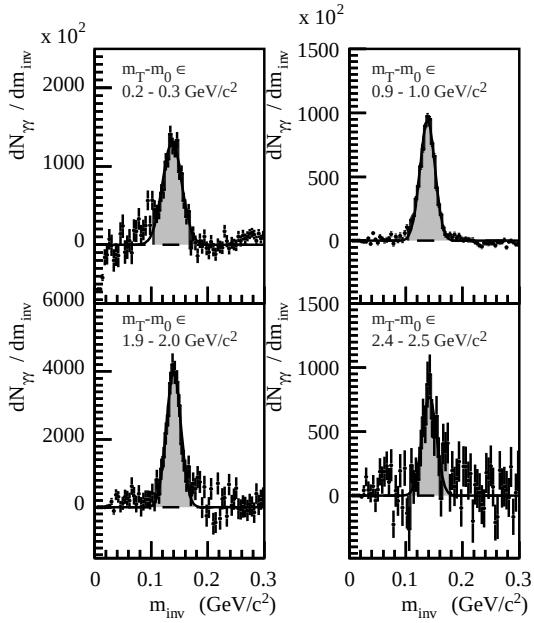

Figure 3.33: The invariant mass distributions of photon pairs for minimum bias Pb+Pb collisions in different intervals of $m_T - m_0$ as measured by the WA98 experiment [93].

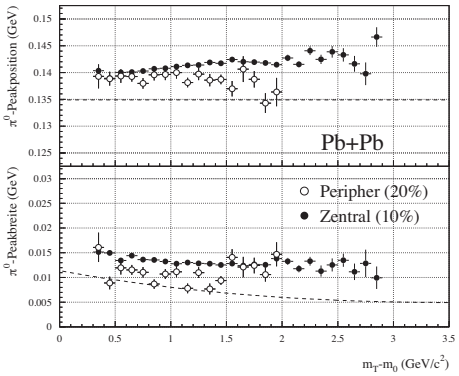

Figure 3.34: π^0 peak position (top) and π^0 peak width as measured by the WA98 experiment [92].

Everything should be made
as simple as possible, but not simpler
A. Einstein

4 Monte Carlo Simulations

4.1 Introduction

A CERES Monte Carlo simulation is used for numerous purposes in particular in this work to determine the detector response for photons and π^0 reconstructed from $\gamma\gamma$ invariant mass analysis. The full Monte Carlo simulation described in this chapter is used for the efficiency evaluation for the neutral pion reconstruction. The CERES Monte Carlo simulation consists of two different levels: at the event generator level (the partons generation) and in the second stage the photons and neutral pions are reconstructed by using the detector simulation. The generated Raw data by the Monte Carlo simulations were processed by the same tracking, vertexing, and filtering programs used for the previous analyzed data. An important aspect of these programs is that they must be applied with same criteria in both Monte Carlo method and data in order to be able to compare the Monte Carlo generation and data. The main Monte Carlo implementations which were used to simulate the CERES spectrometer response are listed below, each step will be discussed in much more details within the next sections.

1. The CERES Event Generator (user-input).
2. The CERES Detector simulation with Geant software..
3. The Conversion from Step2 to Step3c.
4. The reconstruction of the final analysis.

4.2 The physics event generator

This step is called also the **user-input**. A standard physics generator, to generate the partons in the whole phase-space and impose a certain requirements corresponding to the geometry of the detector. The kinematic Event generator generates particle spectra where the main input parameters are particle type, the number of the produced particles per each event and the requested total number in the collision, the momentum distribution, the rapidity distribution, the detector acceptance range. The goal is to define some reasonable cuts to maximize the significance of the results.
To let the π^0's ejectile in the GEANT software (see Section 4.3), the main characteristics of the physical process $\pi^0 \longrightarrow \gamma\gamma$ and those of their decay products are studied via the *TGenPhaseSpace* class found in the ROOT package [95]. The input parameteres of the package are: number of decay particles, masses of particles, betas of decaying particle, total energy in the C.M. minus the total mass, and the kinematics of the generated particles.
The important kinematical parameters which have to be investigated for the generated π^0 and the decayed photons are:

- The phase-space initial parameters.
- The rapidity.
- The transverse momentum p_t.
- Polar and azimuthal angles in the laboratory reference frame.

Owing short mean life time $\tau = (8.4 \pm 0.6) \times 10^{-17}$s [84] which is typically of electromagnetic decays, the π^0's decay before getting free from the collision region. The neutral pions are generated with Boltzmann distribution for the transverse momentum. The corresponding temperature (the inverse slope) of π^0 is 190 MeV/c^2, [96]. The rapidity obey a Gaussian distribution with a mean $y = 2.95$ and width $\sigma_y = 1.2$. [97]. The π^0s are generated isotropically in the center of mass frame, but later the photons which are the decay products are finally boosted using the betas of the π^0 original particle. For the 158 AGeV energies, the beam beta is 2.913 with the rapidity interval [1.5-3.0].

Substantial computations are required to generate high statistics samples for the studied physical process. For that reason the event generation procedure is performed for many steps with same configuration. In each step, 300 files are generated. Each output file contain 9900 events and each event have 50 π^0. That means in any single step we have: $300 \times 9900 \times 50$ π^0. This prescription is the generation stage.

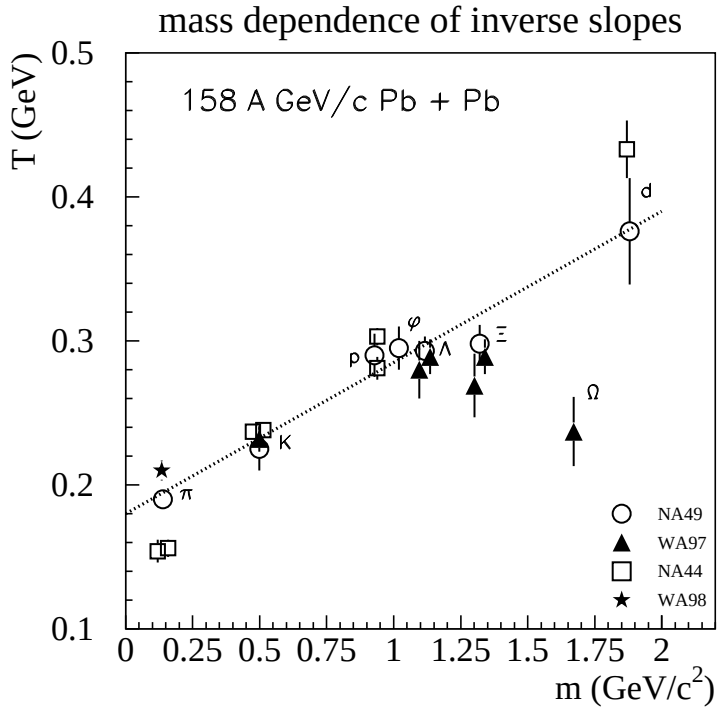

Figure 4.1: The dependence of the m_T spectra inverse slopes T on the particle mass m at CERN-SPS Pb-Pb collisions.

The second stage consists of filtering the photons with the geometrical acceptance cut which is 0.135 (rad)$< \theta(\gamma) <$0.25 (rad). This criteria is chosen to cover the CERES spectrometer.

The scatter plot in figure (4.2) illustrates the generation and acceptance stages of the rapidity versus the transverse momentum distribution of the neutral pion. On the left, before applying the geometrical cut, and on the right side of the figure, after fulfilling the geometrical acceptance requirement. We see clearly that we have large acceptance for the bulk of the π^0 in $0 < p_t < 2$ GeV/c and rapidity of y $\in [2.2 - 2.7]$. The transverse momentum distribution of the neutral pion in figure (4.3).

An additional check is needed and performed to verify the opening angle between the two photons as function of the π^0 transverse momentum. This is

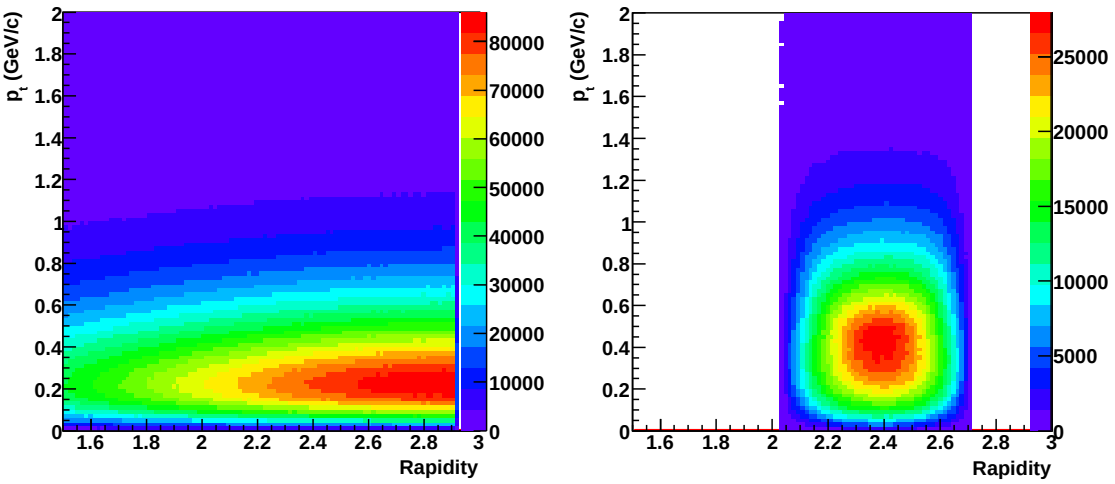

Figure 4.2: The distribution of the neutral pion rapidity versus the transverse momentum. The left panel represents the generated distribution in the whole phase-space while. The right panel, shows the accepted distributions where the two photons are within the CERES spectrometer acceptance.

shown in figure (4.4).

So far, all the kinematic properties of the generated/accepted π^0 and of their decay product, the photons, are known. The 4-momentum vectors of the mother particles (π^0) and the daughters ($\gamma\gamma$) are recorded. The full decay/production history is stored in dat format files. The produced γ's by the Kinematic Event generator were used for studies that required larger statistics. The number of the generated neutral pion used for the complete Monte Carlo simulations is about 7 millions of π^0. A total of 4 TBy is needed to store the MC simulation. An another aspect of using the Event generator can be noticed. It gives an estimation of an insight of how we could achieve the neutral pion reconstruction which is decaying into two photons within the geometrical acceptance.

4.2.1 Expected number of π^0 mesons

As mentioned in Chap.2 the CERES experiment recorded 30 million good events in collisions of heavy nuclei during the running period in the year 2000. Before to perform this analysis, we have use a quantitative method to explore the expected number of π^0 and (η) yields after the analysis to check the feasibility of such analysis.

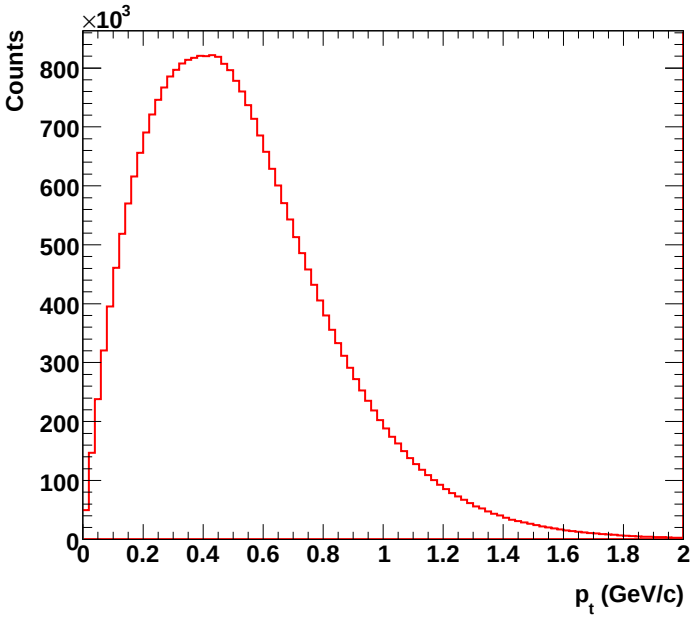

Figure 4.3: The transverse momentum distribution of the neutral pion.

The number of π^0 mesons produced per event is approximately about 500 neutral pion at the CERN-SPS energy of 158 AGeV/c [98] if we take it equal to the number of $\pi^{\pm}$. Getting the output parameters of the π^0 from the kinematic generator described above, we can recapitulate these complete information in order to offer an estimation of the π^0 expected number.

$$N_{\pi^0} = \text{BR}\times 500\pi^0 \times \text{acceptance} \times \text{N}_{\text{event}} \times (\text{conversion probability})^2 \times (\text{single track efficiency})^4. \quad (4.1)$$

where:

- N_{π^0} is the total number of the expected π^0's.
- BR: the branching ratio of $\pi^0 \longrightarrow \gamma\gamma$ (98.8 % [84]).
- The acceptance $= \dfrac{nAcc_{\pi^0}}{nGen_{\pi^0}}. = \dfrac{495000}{3802554} = 0.13$
- N_{event}: the total number of the recorded events (30.10^6 events).
- The efficiency = (conversion probability)$^2\times$ (single track efficiency)^4

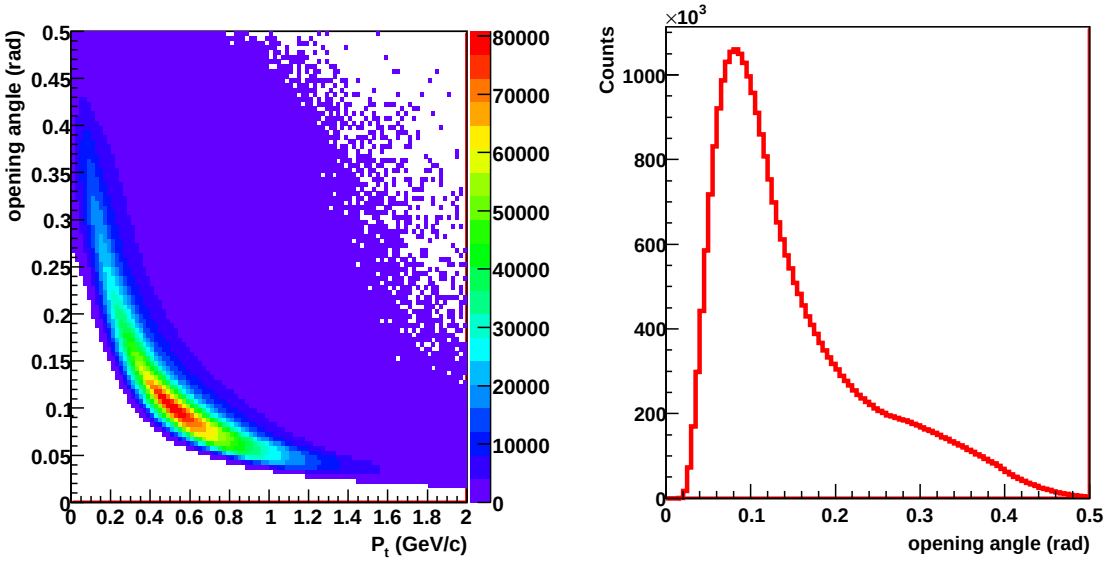

Figure 4.4: The $\gamma\gamma$ opening angle distribution versus the transverse momentum of the neutral pion. The projection of the opening angle is plotted on the right panel.

Given the low conversion probability ($\sim$ 4%) introducing 50 π^0/event does not distort the underlying event. It means a mean of 4 electrons (4 positrons) in addition to the 300 charged tracks per event.
If we take the efficiency for detecting a neutral pion $\approx (0.04)^2$, from the conversion probability as an approximation, this reads :

$$N_{\pi^0} = 3.06 \times 10^6 \pi^0 s \tag{4.2}$$

This number is an upper limit because it assumes that conversions are reconstructed with $(0.9)^4$ but as e^+/e^+ have usually very low momentum, thereby the efficiency will be lower.

In relativistic heavy ion collisions, the analysis performed on the ratios of the produced hadrons shows that they are well described by a statistical model. The hadron production is described using thermal models enabling to encounter the yield particles. In this way, the ratio η/π^0 is obtained from the thermal model [99] which is in very good agreement with the experimental data. It states the particle ratios as they were measured by several experiments at the SPS in Pb-Pb collisions. In figure (4.5), the particle ratios of different hadrons are illustrated. In addition to what has been found in the π^0 case, one can anticipate using the η/π^0 ratio obtained from the thermal model and applying the same previous calculation in order to get

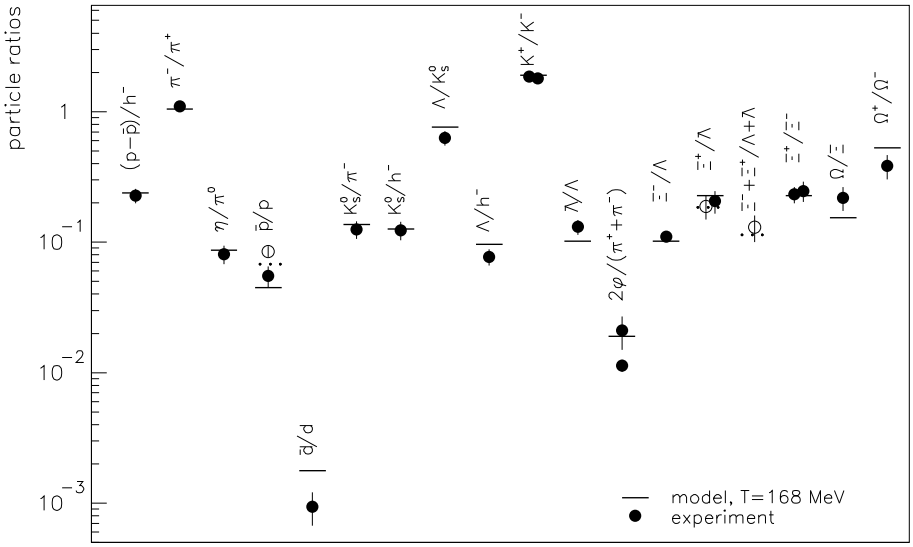

Figure 4.5: The comparison between the Thermal model [99] and the experimental data particle ratios.

the expected number of the η meson. This means:

$$N_\eta = \text{BR}\times 42\eta\times\text{acceptance}\times\text{N}_{\text{event}}\times(\text{conversion probability})^2\times(\text{single track efficiency})^4. \tag{4.3}$$

where:

- N_η is the η expected number.
- BR is the branching ratio of $\eta \longrightarrow \gamma\gamma$ (39 %).
- The acceptance = 5000/116279 = 0.043.

Again taking the same assumption for the efficiency $\approx (0.04)^2$, from the radiation length as an approximation, this gives:

$$N_\eta = 3.4 \times 10^4\eta \tag{4.4}$$

We now may compare the π^0 measurement and the η measurement which is difficult due to the smaller production rate and the smaller 2γ decay branching ratio.

4.3 The detector simulation

The complete simulation of the photons from the π^0 decays in the CERES experiment is described in this section. The CERES detector setup is implemented

in the GEANT simulation [100]. The ouput informations of the Event Generator (user-input) contained in the dat files (see Section 4.2) are propagated through the CERES detector volume. The GEANT software simulates the passage of the generated elementary particles (γ's from the π^0 decays) by the Event generator through the matter. It provides a full data base passage of the standard geometrical shapes and materials used to model the CERES spectrometer.
All the essential physical interactions of the photons with the detector material are computed. Every propagated particle is simulated with GEANT independently. At the final stage the particle trajectory can be traced and thus saved in RAWMC format files. The digits in the RAWMC files include all energy deposits (hits) recorded during the particle trajectory during its passage through the individual elements of the detector. This means each hit is assigned to a track number to where it is originating from.
The digitization framework of the RAWMC output files is performed to build a mapping between the location of sensitive detectors within GEANT, and the subsequent front-end electronics functionality. This step is accomplished by using the CERES *Step2 Analyzer*.
However, before to proceed the digitization process of the simulation output, a *setup.analyzer* file is used to set one of the two options: *Clean Monte Carlo (CMC)* or *Overlay Monte Carlo (OMC)* simulations. The CMC is used basically for fast simulations of the CERES spectrometer. The CMC option allow us to gain additional insights into the detector effects in less computing time with low disk space storage. It allows very flexible runtime configuration once every check have been checked. The OMC operation is done by overlaying the simulated Monte Carlo tracks on top of the real raw data event. The association is made accurately only between the GEANT tracks as an input and the OMC tracks as output.
The output of the Step2 Analyzer during the digitization process are written in ROOT format files. They are accessible and can be checked at any stage of the GEANT simulation engine. This ability is an important aspect to ensure that the Monte Carlo faithfully reproduce the truth detector manifestations. This simulation chain was performed to produce about 7 million π^0 events. This task is time consuming and have to be handled in very large volume of disk space (4 TBy).

4.3.1 The Conversion from Step2 to Step3c

After the Step2 Analyzer simulation chain, the output of this simulation has to be proceeded through the same reconstruction treatment used in the experimental data analysis softwares described in Chapter 3 (Step3c). This means that once this step is reached all the track finding, track fitting operations are applied in the same way as in the data analysis.

The Purity

For each reconstructed track, we associated simulated track with the largest common number of hits. The *purity* of the reconstructed track, defined as the fraction of hits having same MC parent among hits attached to the track is calculated. It can be written for i^{th} track as:

$$Purity = \frac{NHits(MC, (i^{th}track))}{NHits(All, (i^{th}track))} \tag{4.5}$$

where $NHits(MC, (i^{th}track))$ represents the number of hits for the i^{th} Monte Carlo track and $NHits(All, (i^{th}track))$ is the total number of the associated hits of the i^{th} Monte Carlo track. The distribution of the Purity for reconstructed tracks is shown in figure (4.6)

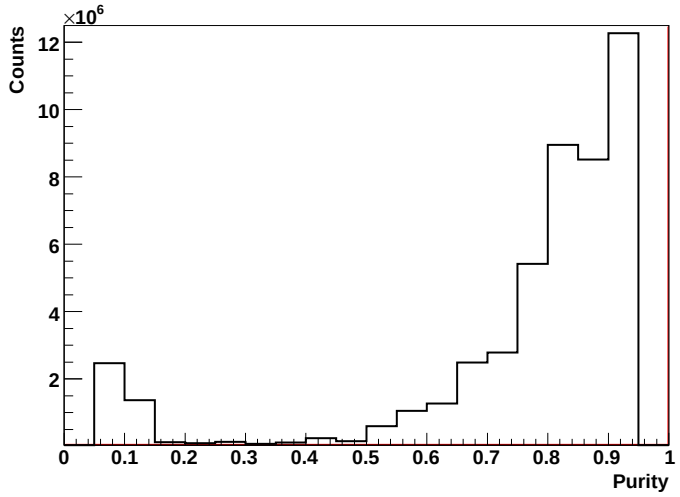

Figure 4.6: The Purity distribution of the reconstructed charged tracks from the assigned Monte Carlo tracks.

The association of a reconstructed track to a simulated track is successful if the Purity exceeded 50%. The reconstructed tracks which are not associated with a simulated tracks are called ghost tracks and they are not taken into account. By using the Purity condition we are rejecting the ghost tracks from the reconstruction chain

Completely reconstructed tracks will be employed to perform the main analysis of the reconstruction efficiency of the neutral pion analysis.

4.3.2 The reconstructed tracks comparison

The reconstructed tracks which survived after the Purity condition, are compared to the true values in order to cross check the reconstruction chain provided by the Overlay Monte Carlo simulations. The phase-space covered by the TPC is shown in figure (4.7).

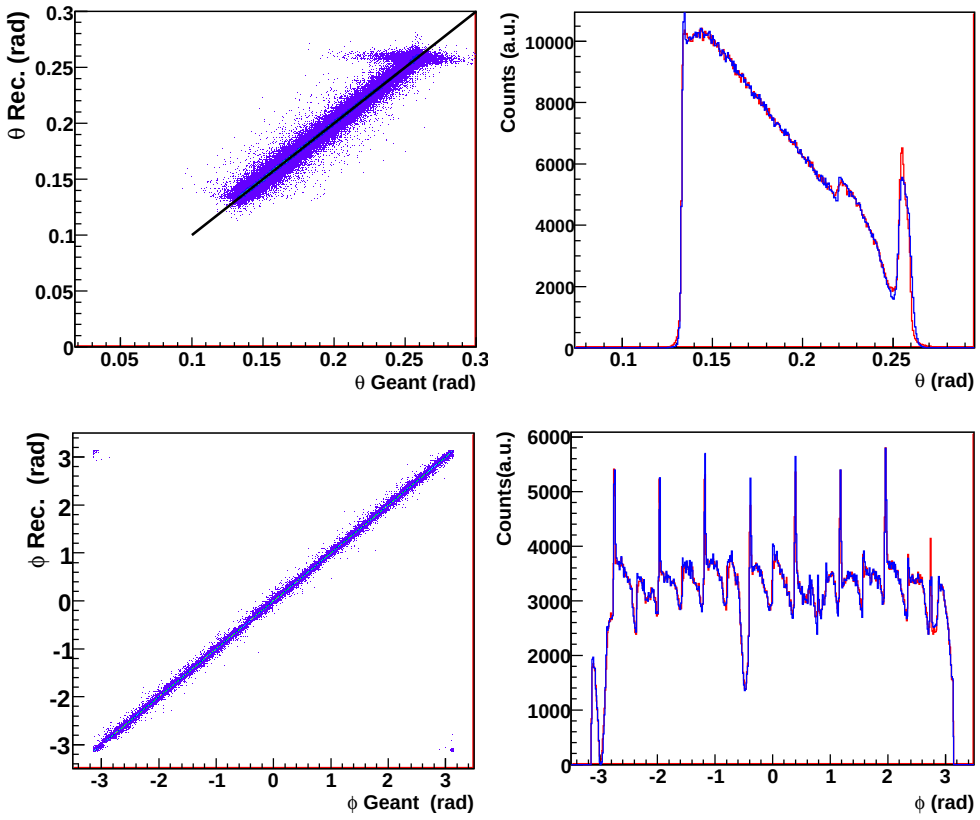

Figure 4.7: The polar and the azimuthal angles distributions from the reconstructed tracks and the the true tracks. Top left panel, correlation between reconstructed theta and Geant θ for electrons/positrons versus the reconstructed θ distributions. The black solid line indicated the normalization region. Top right panel, polar angles distributions, the Geant (true) distribution in blue and the reconstructed distribution in red. The bottom panels indication mentioned before however this case refers to the azimuthal distributions.

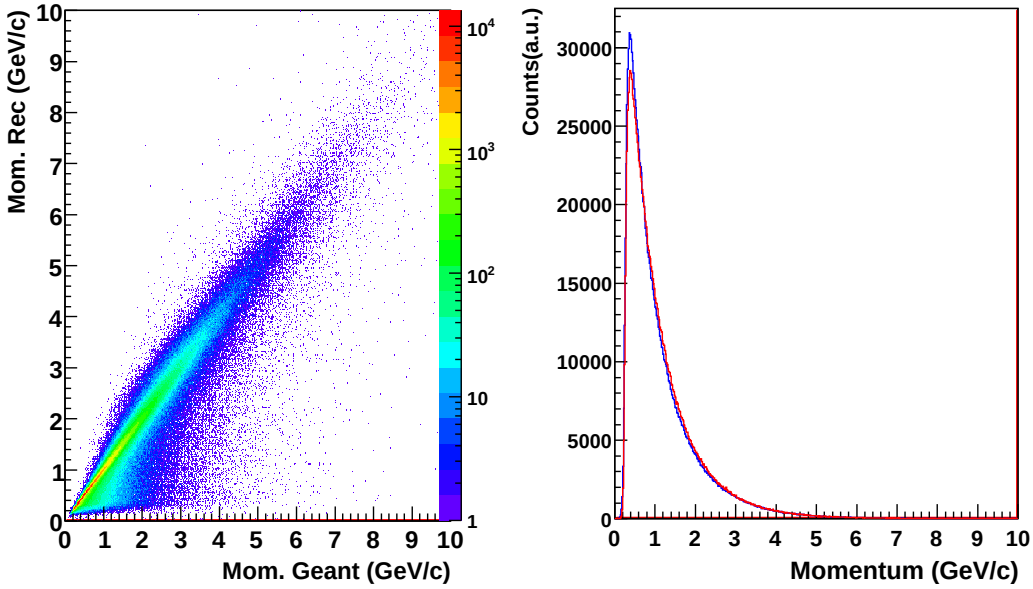

Figure 4.8: Left: distribution of the reconstructed momentum vs the Geant momentum. Right: distribution of the reconstructed momentum (red) and the Geant momentum (blue).

Figure (4.7) illustrates the polar and the azimuthal angles distributions from the reconstructed tracks which were determined by the Overlay Monte Carlo technique (similar the Step3c) and the true tracks which are the output of the Step2 Analyzer. The polar angles are plotted in the range $0 < \theta < 0.3$ rad. The structure at high theta angles are not considered since we cut on $0.135 < \theta < 0.25$ rad. This point will be justified in the analysis section. The azimuthal angles distribution are scanned and plotted in the range $-3.15 < \phi < 3.15$ rad. The structure of the pad chambers and the 8 spokes of the TPC are clearly visible. A visible sign of hole is positioned at $\phi \approx -3$ rad. This behavior refers to a dead region during data taking. The momentum distribution from the reconstructed tracks compared to Geant tracks in shown in figure (4.8). The low distribution on the Geant part reflects the reconstructed energy loss due bremsstrahlung process.
Figure (4.9) shows the number of the TPC fitted hits on the track for Overlay Monte Carlo simulation is plotted in blue and for data in red. One can notice that the taken cut for $NHits$ larger than 10, indicated by the black vertical line, applied in both Overlay Monte Carlo and data is a good estimation.

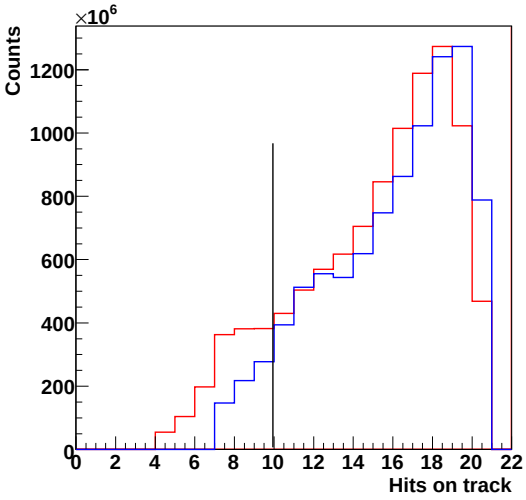

Figure 4.9: The Comparison of the TPC fitted hits on the track for Overlay Monte Carlo simulation plotted in blue and for data in red, the vertical line ta $NHits = 10$ indicates the the minimum value for the reconstructed track taken in both cases.

4.4 The unlike/like sign pairs comparison

As mentioned before, the same reconstruction steps are done for all the MC as for the data. The first step is to reconstruct the photons from the measured electrons and positrons. For that purpose the opening angle distribution of the e^-e^+ pairs and of the like sign pairs is computed (see figure (4.10)). The signature of photon conversion is clearly seen (a peak at small opening angles). The various selection criteria imposed on pair tracks (electrons and positions) events is based on those of data analysis.

The subtracted signal to background distributions is studied in ten momentum bins $0 < p < 10$ GeV/c. Figure (4.10) illustrates a shape comparison of photon signatures (unlike sign - like sign pairs) between the data (in red) and the Overly Monte Carlo (in blue) distributions, each momenta window represents 1 GeV/c. The comparison in each momentum bin was made by the normalization of the maximum of the photon conversion signals in both Overlay Monte Carlo and data. One can see that there is a tiny difference between the opening angle distributions of MC and data. For that reason, we smear the MC angles to match the data by the values $(0.5 - 0.5 \times |p_e|)$ mrad for the polar angles and with $(2.5 - 2.5 \times |p_e|)$ mrad for the azimuthal angles.

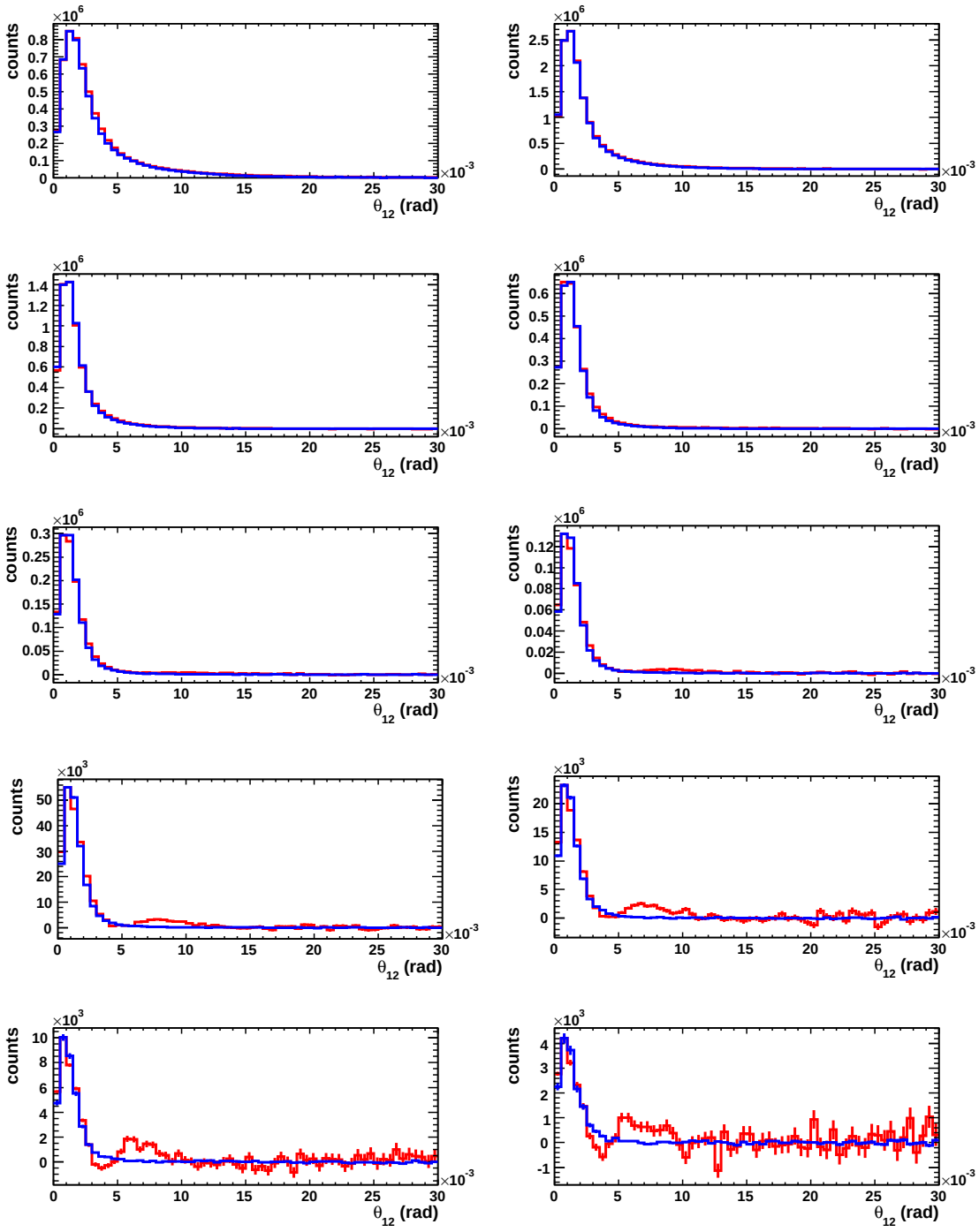

Figure 4.10: The Photon signal distribution comparison between the Overlay Monte Carlo simulations (blue) and data (red). Each momentum window represents 1 GeV/c.

The obtained opening angles for the smeared values compared to those of the data are shown in figure (4.10). The photon conversion signatures are well pronounced in all the momentum bins and became narrower at high momentum. The Overlay Monte Carlo and data distributions reproduces both the same photon signal width. At large momentum, the data distributions exhibits an extra contributions at higher opening angle. It should be mentioned at this point this situation is happening in the region outside the real signal distribution where the photon conversion signature is well defined and known. Furthermore, this misidentified background is not seen in the Overlay Monte Carlo where the input particles to Event Generator are photons within the acceptance range from π^0 decays.

However, the presence of the effect would manifest itself by a question which arises part of the effect and if it has a different origin. It is therefore useful to look at the charged tracks of electrons and positrons selection criteria mentioned in Section 3.6. The observed structures in the signal to background distributions for 7 (GeV/c) $< p <$ 10 (GeV/c) are expected to come from of highly ionizing $\pi^{\pm}$. We optimized the ionization energy loss cuts to reject pions by keeping the upper limit cut $dEdx < 440$ and settled on tight cut values of $dE/dx > 290 + 2.log(p)$ at energy loss low ionizing regions. This highly ionizing tracks which pass the tightened cut are illustrated by figure (4.11, right).

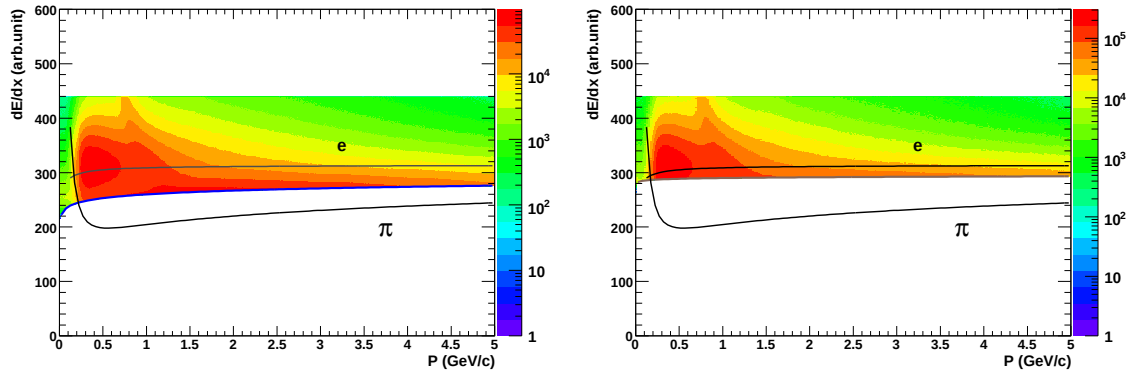

Figure 4.11: The left panel represents the used energy loss of the charged particles measurement within the TPC, the blue incline line and the upper cut at 440 refers to the electron/positron selection. The right panel shows the tighter energy loss in brown in order to cross check the additional structure shown in the photon signal at $\theta(e^-e^+) \sim 7$ (mrad) at high momentum.

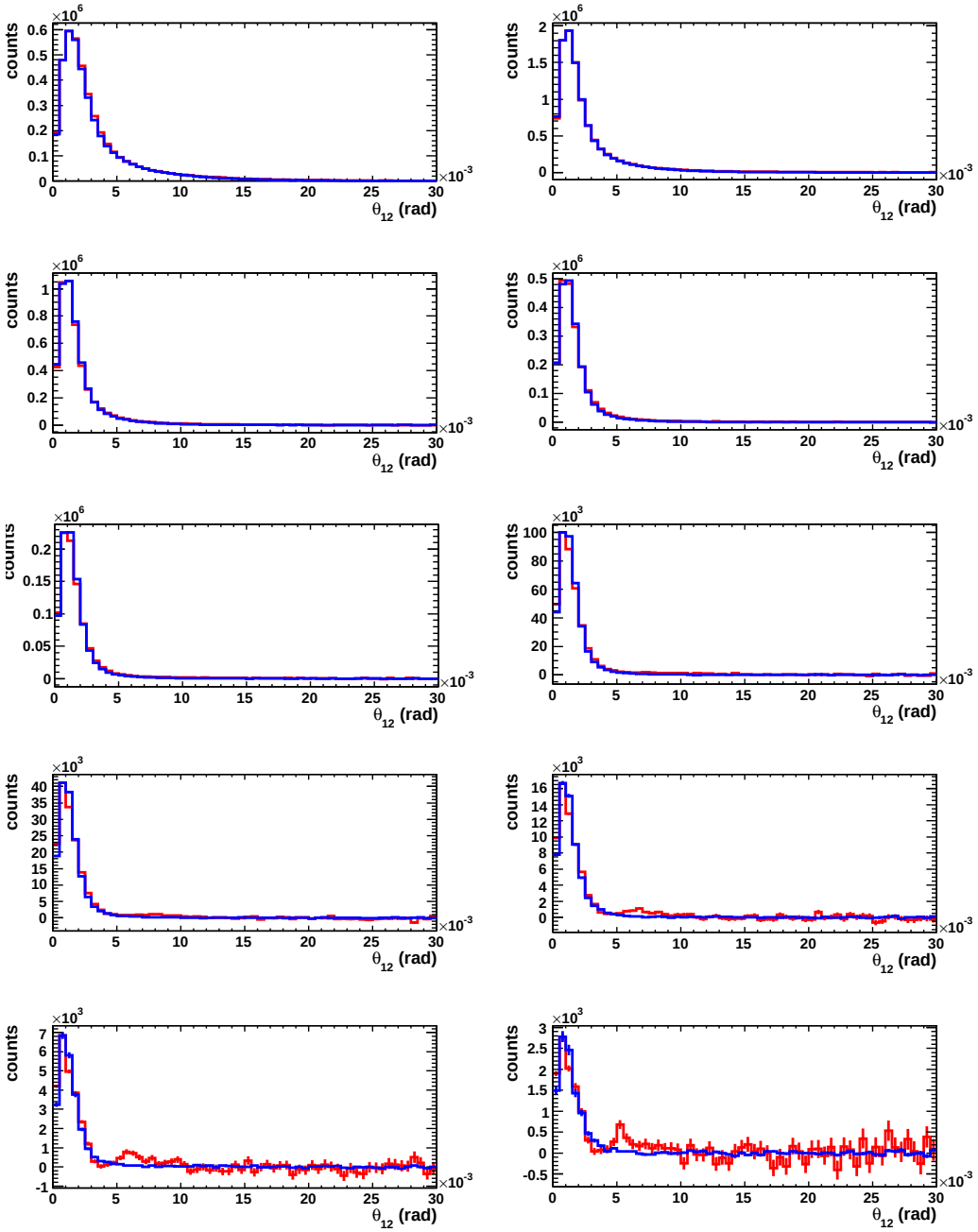

Figure 4.12: The Photon signal distribution comparison between the Overlay Monte Carlo simulations (blue) and data (red) after applying the new dE/dx condition. Each momentum window represents 1 (GeV/c).

The left panel of the figure (4.11) represents the considered energy loss area for the electron/positron selection, and in the right panel, the performed dE/dx check-cut. Thus, in order for a electron/positron leptons to fulfill the loose requirements, it must pass only the dE/dx ionization cuts mentioned above. By inspecting figure (4.12), one can conclude that this approach explicitly minimize the uncertainties related to the suppression of the charged pions contributions. Consequently, these little bumps are originating from the charged pions and not from the electrons and positrons.

4.5 The Photon mapping comparison

The reconstruction procedure of the photons is based on the measured charged tracks of the electrons and the positrons from the Overlay Monte Carlo simulations. The reconstruction of final state photons requires a well measured photon candidate where the combinatorial background is estimated by like sign distributions. The used criteria for the photon reconstruction are the same of those mentioned already in Section 3.6.2. One should, however, keep in mind that the photons has to be within a fiducial volume of $0.135 < \theta_{TPC} < 0.25$ rad and full azimuthal coverage.
The comparison of the reconstructed photons candidates from the Overlay Monte Carlo method and the analyzed data can be done by the integration method. This method can be illustrated by figure (4.13). The integral procedure generally consists by calculating the angular distribution integrals of the reconstructed photons in the Overlay Monte Carlo and in the data, then performing the scaling by using the obtained ratio of the two integrals. The normalized region in θ is 0.14-0.22 (rad) and then we use the ratio of the two integrals within this region to scale the polar and azimuthal MC distributions.
The key test of the Overlay Monte Carlo is its ability to reproduce/describe the different distributions of the reconstructed photons in the detector at the level of RICH2 mirror. Although the Overlay Monte Carlo reproduce the photon distributions and agrees well with the data, a minor problem encountered here is related to small differences between the photon mapping described by Overlay Monte Carlo simulations and data. The difference is slightly seen by looking at the angular distributions comparison provided by the integration method, where in contrast if we consider the comparison performed by the maximum method. Following these investigations, this may affect the reconstruction efficiency by making a geometrical correction factor due to tiny differences between the photon topologies dependence of θ and ϕ in the simulation and data.

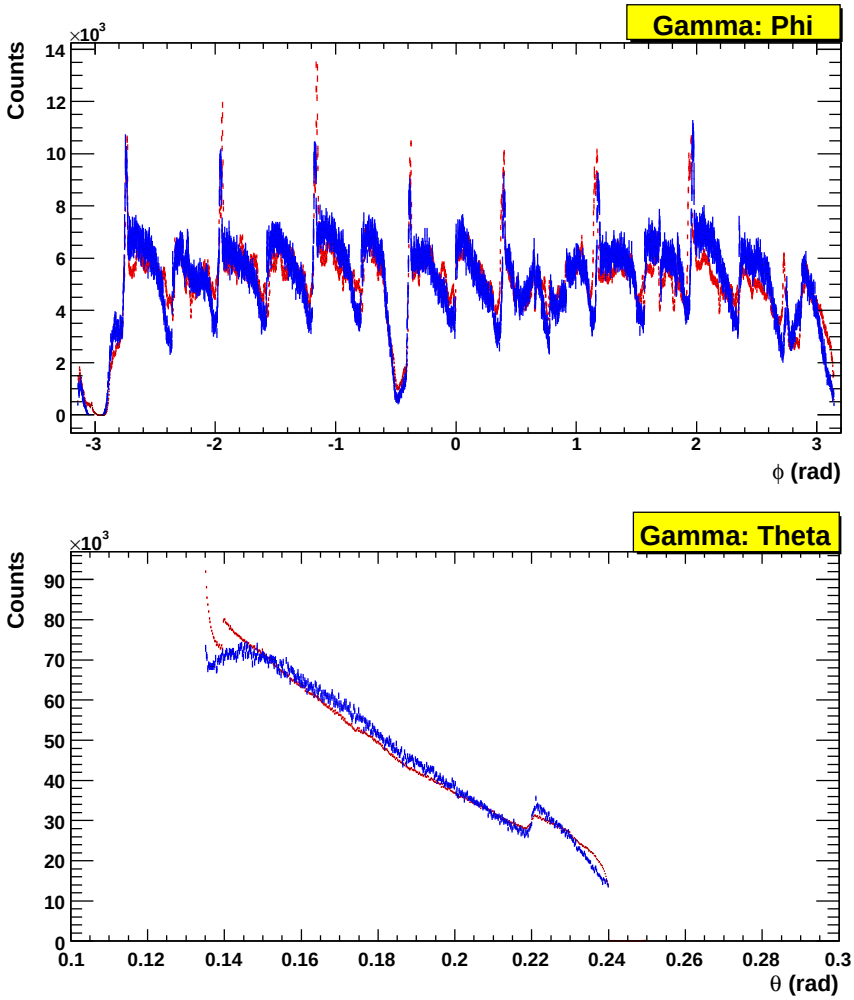

Figure 4.13: The comparison of the subtracted angular distributions of the azimuthal (upper panel) and the polar (bottom panel) distribution in the normalization region $0.14 \leq \theta < 0.22$ rad. The MC distributions are plotted in blue and the data distribution are in red.

4.6 The Secondary Vertex Comparison

The position of the photon decay vertex was reconstructed from opposed charged tracks detected in TPC and originated from the RICH2 mirror area. Th Z-vertex positions were determined using the same algorithm as detailed in our previous study described in Chapter 3. The combinatorial background has been subtracted from the real photon signal for each momentum bin (shown in figure (4.14)).

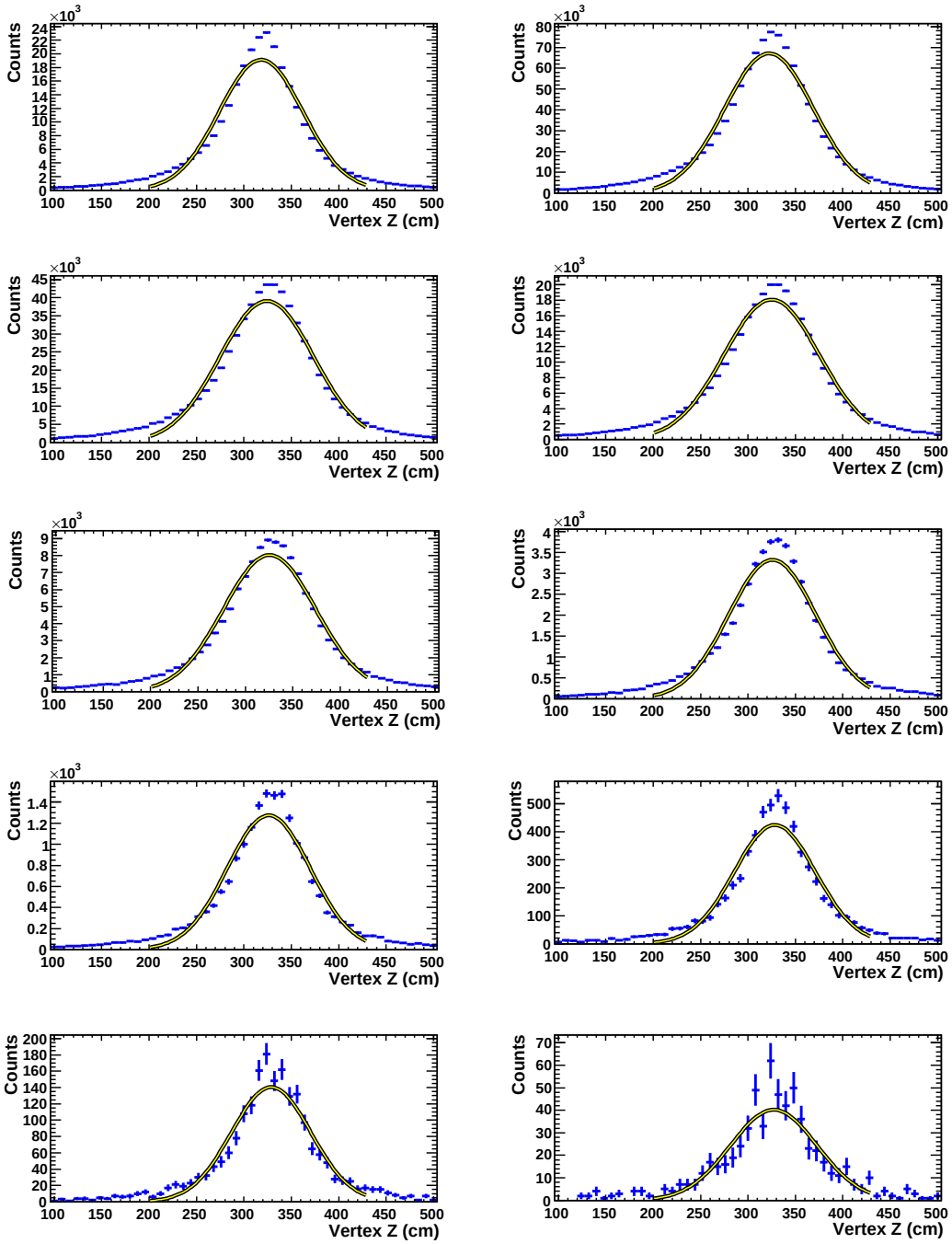

Figure 4.14: The Secondary Vertex distributions of the subtracted signal to background reconstructed in the Overly Monte Carlo simulations. Each window represents 1 GeV/c photon momenta.

Then the next step is performing the Secondary vertex cut in the region the RICH2 converter, i.e. $\mu(Sec.Ver.) - 2\sigma(Sec.Ver.) < Z < \mu(Sec.Ver.) + 2\sigma(Sec.Ver.)$. The obtained Secondary vertex distribution was then fitted with a Gaussian function. All these distributions have been carefully evaluated firstly with an appropriate fast Monte Carlo simulations before performing the Overlay Monte Carlo method. The aim of this step is to cross check the validity of the used Secondary Vertex algorithm.
The photon vertex position in the Overlay Monte Carlo simulations which fulfilling the same requirements as in data is presented in figure (4.15).

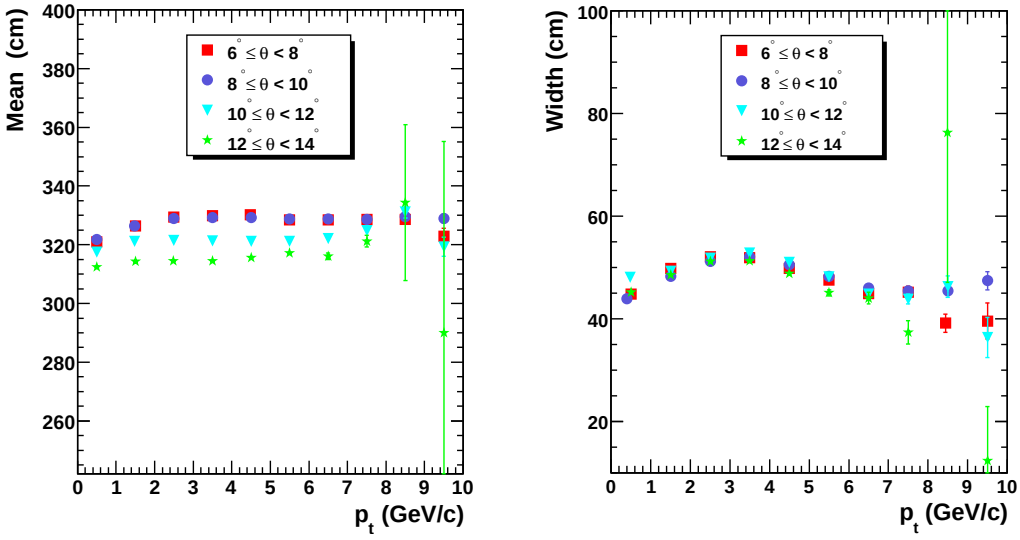

Figure 4.15: Left panel, the position of the photon vertex converting to e^-e^+ for Overly Monte Carlo. On the right panel, the corresponding width of the Secondary vertex distribution.

The Secondary Vertex distributions from the contributions of the unlike and like sign pairs as function of the photon momentum provide the precise position and resolution parameters to define the Secondary Vertex cut. It can be seen that the photon events of the same momentum and the same Z longitudinal distance of the photon decay vertex from the RICH2 converter agrees very well in both data (see figure (3.18)) and Overlay Monte Carlo. As conclusions, the obtained yield photon measurements in the Overlay Monte Carlo simulations validates our used method for the Secondary Vertex fit algorithm, described in Section 3.7. The width in data is larger. In order to evaluate the efficiency the sigma from the MC simulations is

used in MC and in the corresponding from data.

4.7 The $\gamma\gamma$ invariant mass distributions

In order to evaluate the reconstruction efficiency for the neutral pion production, the $\gamma\gamma$ invariant mass distributions are studied and checked. All the following invariant mass distributions are based on the same cut criteria as used in the data analysis. We perform our study as function of transverse momentum in the range $0 < p_t < 2$ GeV/c and rapidity splitted in three ranges expressed as: $2.2 < y_1 < 2.4$, $2.4 < y_2 < 2.6$ and $2.6 < y_3 < 2.7$. We have to keep in mind that we find that signal candidates in the regions: $0.25 < p_t < 0.5$ GeV/c and $0.5 < pt < 0.75$ GeV/c are considerably contaminated by background events along all the taken rapidity ranges (y_1, y_2 and y_3). This effect have been seen in data and Overlay Monte Carlo. Therefore a special opening angles between the two photon candidates is needed. For this purpose we require a tighter conditions as in the data:

$$\begin{cases} y_1 \quad \text{and} \quad 0.25 < \mathrm{p_t} < 0.5(\mathrm{GeV/c}) \Longrightarrow \theta(\gamma\gamma) \geq 0.11(\mathrm{rad}) \\ y_1 \quad \text{and} \quad 0.5 < \mathrm{p_t} < 0.75(\mathrm{GeV/c}) \Longrightarrow \theta(\gamma\gamma) \geq 0.08(\mathrm{rad}) \\ y_2, y_3 \quad \text{and} \quad 0.25 < \mathrm{p_t} < 0.5(\mathrm{GeV/c}) \Longrightarrow \theta(\gamma\gamma) \geq 0.1(\mathrm{rad}) \\ y_2, y_3 \quad \text{and} \quad 0.5 < \mathrm{p_t} < 0.75(\mathrm{GeV/c}) \Longrightarrow \theta(\gamma\gamma) \geq 0.07(\mathrm{rad}) \end{cases} \tag{4.6}$$

As in our MC the complete history from the e^-/e^+ to the π^0 was not properly stored, it was impossible to know which two γ's come from the same π^0. Therefore, the same analysis was done in the data, namely all the γ's in one event are combined in pairs. The signal appears on top of the uncorrelated background.
The different subtracted invariant mass distributions obtained under these requirements are shown in figures (4.16), (4.17) and (4.18). Principally two studies are done using the MC results: in one hand π^0 yield as function of pair transverse momentum in order to obtain the efficiency of the π^0 reconstruction. In the other hand, to study the position and width of the π^0 peak as function of p_t and rapidity to compare them with the analyzed data. This provides us a measurement of how good the MC describes the data.

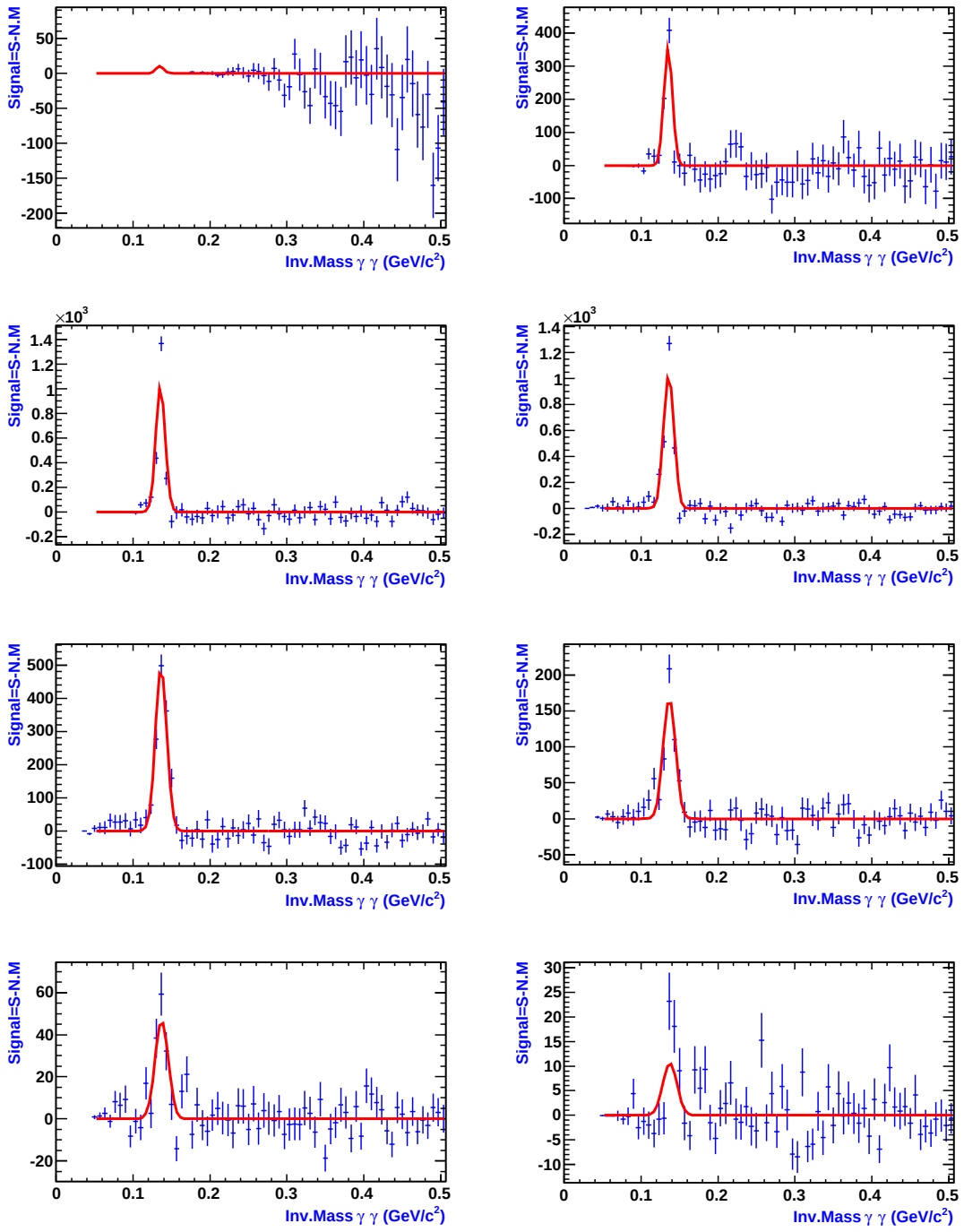

Figure 4.16: The MC real mass distribution of π^0 after subtracting the normalized mixed event distribution in the range $2.2 < y < 2.4$ and in 8 p_t bins of 0.25 GeV/c width.

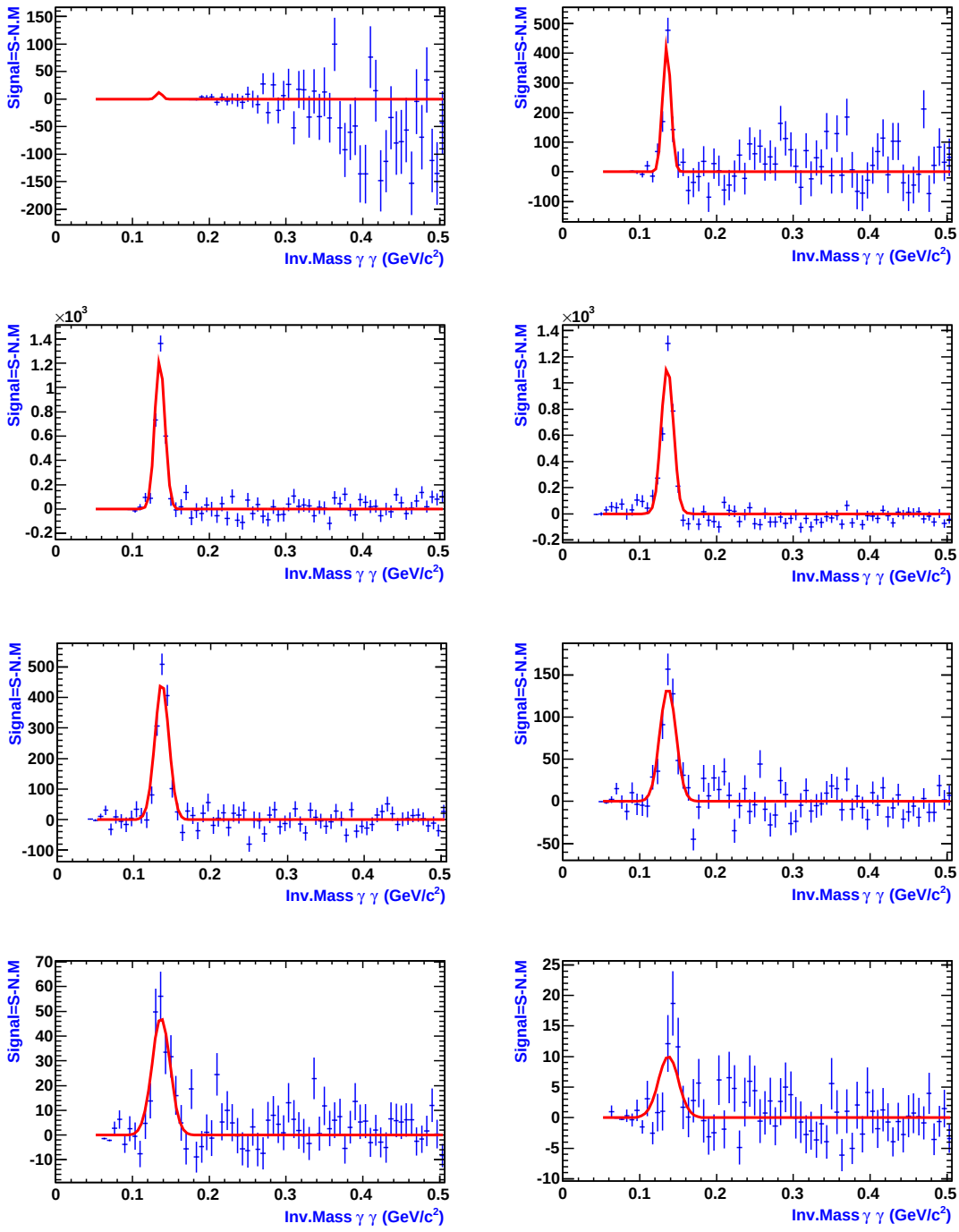

Figure 4.17: The real mass distribuion of π^0 after subtracting the normalized mixed event distribution in the range $2.4 < y < 2.6$ and in 8 p_t bins of 0.25 GeV/c width.

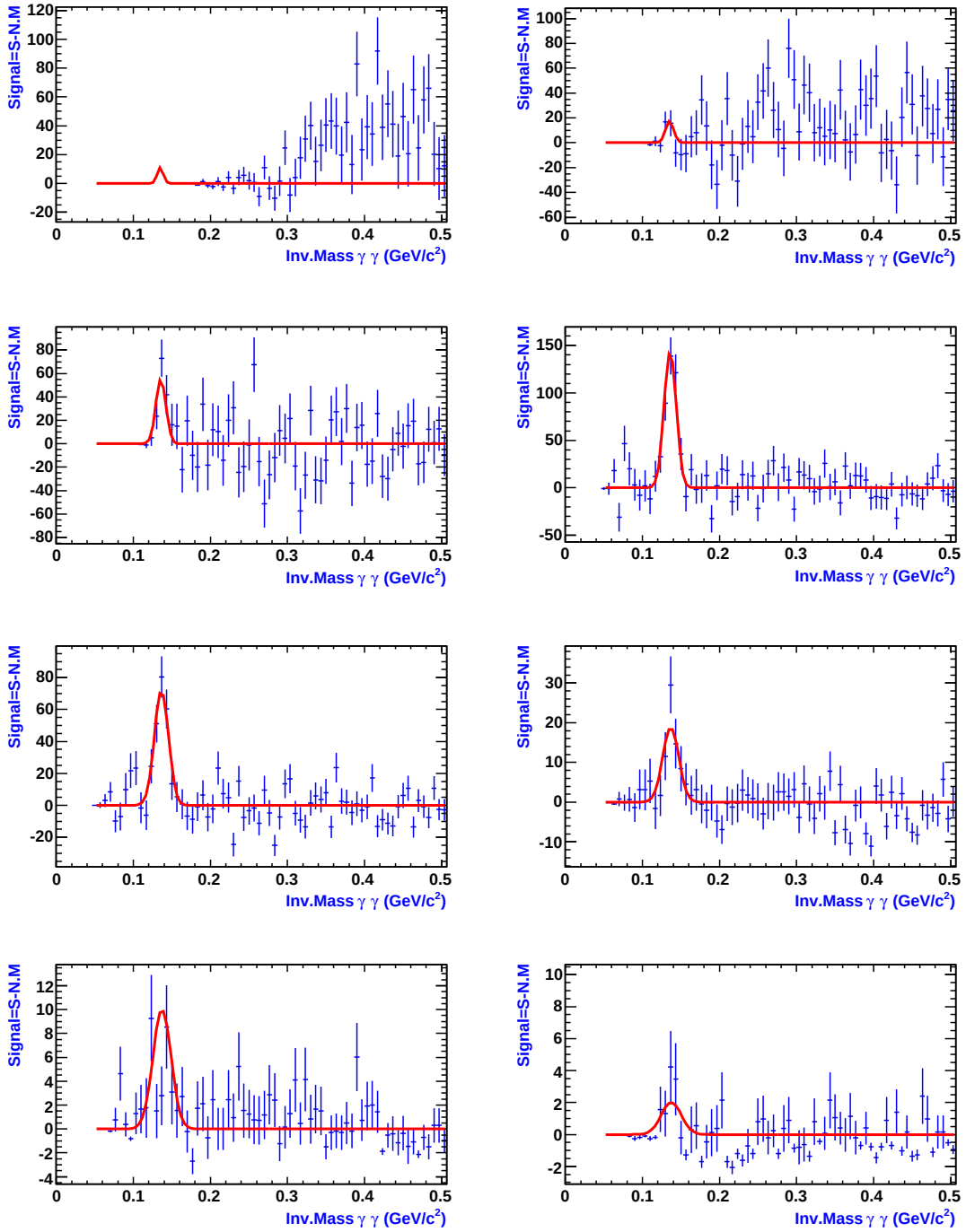

Figure 4.18: The real mass distribuion of π^0 after subtracting the normalized mixed event distribution in the range $2.6 < y < 2.7$ and in 8 p_t bins of 0.25 GeV/c width.

We can summarize these investigation by looking to the mean and the width of the reconstructed $\gamma\gamma$ mass versus the transverse momentum shown in figure (4.19).

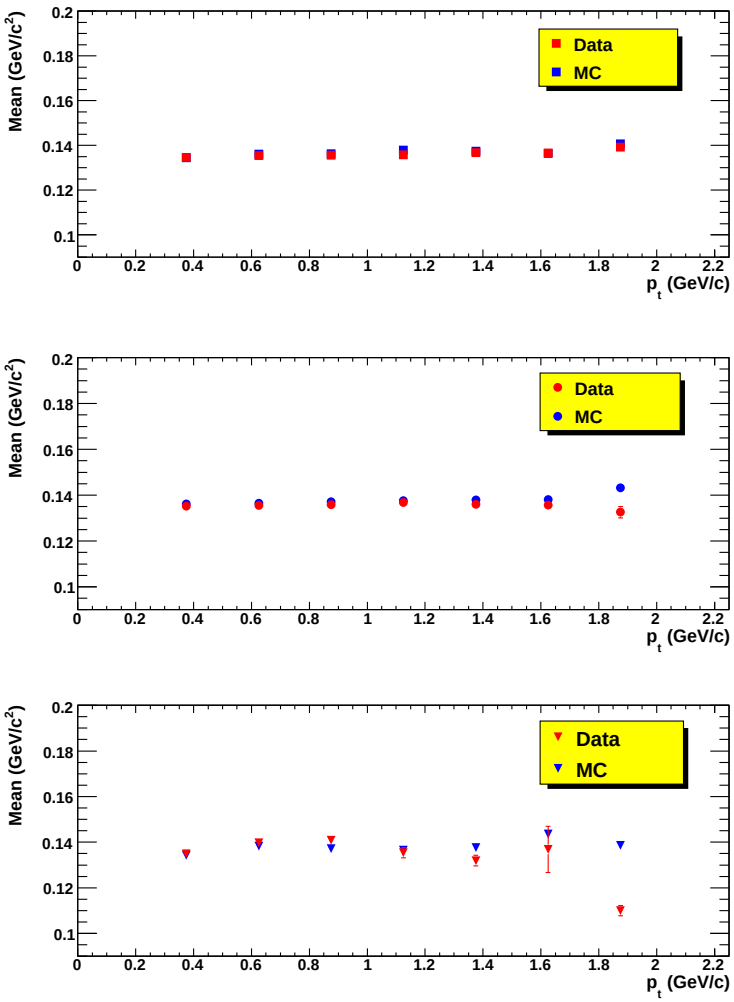

Figure 4.19: The position of π^0 signal obtained from the $\gamma\gamma$ invariant mass distributions in the Overlay Monte Carlo compared to the values obtained in data as function of the π^0 transverse momentum and rapidity. The top panel represents the first rapidity range y_1: 2.2-2.4, the middle panel is for the second rapidity range y_2: 2.4-2.6, and the last panel is for the last rapidity range y_3: 2.6-2.7. The MC distributions are plotted in blue and data in red

.

The mean of real invariant mass distribution of the Overlay Monte Carlo and data agrees very well for the first two rapidity intervals y_1 and y_2, however in the third rapidity interval, due to low statistics and 0.1 rapidity step the invariant mass distribution is slightly different at high momentum. This can inspected also when looking to the width distributions illustrated in figure (4.20).

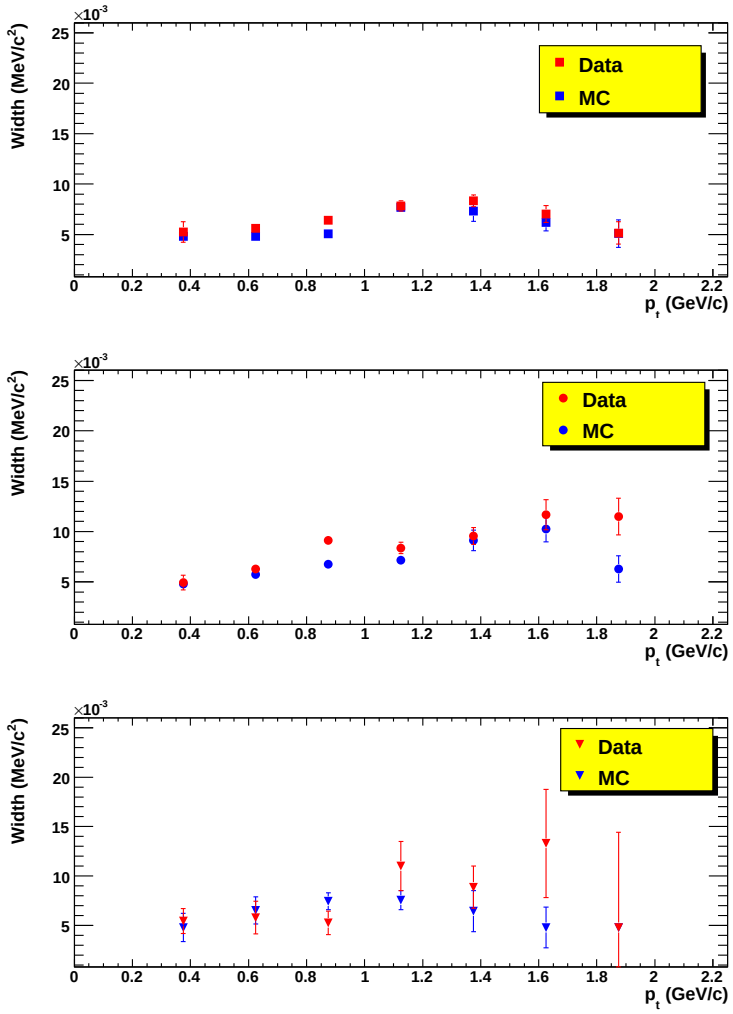

Figure 4.20: The width of π^0 signal obtained from the $\gamma\gamma$ invariant mass distributions in the Overlay Monte Carlo compared to the values obtained in data as function of transverse momentum and rapidity. The top panel represents the first rapidity range y_1: 2.2-2.4, the middle panel is for the second rapidity range y_2: 2.4-2.6, and the last panel is for the last rapidity range y_3: 2.6-2.7. The MC distribution are plotted in blue and data in red.

4.8 Acceptance and efficiency evaluation

The π^0 yields as function of the p_t and rapidity obtained in the invariant mass analysis (see Section 3.8) do not reflect directly the neutral pion production. All the measured quantities must be corrected by certain factors which take into account the geometrical acceptance and efficiency of the CERES detector. Therefore, determining the detector acceptance and the reconstructed efficiency for the selection criteria used in this analysis is essential to obtain quantitative and properly calculated π^0 production yields. The acceptance is the phase-space region covered by the TPC detector. It is related to the detector geometry. However, the efficiency evaluation depends on the reconstruction efficiency of tracks determined by the reconstruction chain listed in Section 3.1.
The multiplicity in the full phase-space is generated within the Boltzmann distribution for the transverse momentum and a Gaussian distribution for the rapidity distribution with a mean $y = 2.95$. The transverse momentum and rapidity distributions were studied in eight p_t bins and in three rapidity intervals. The two first equidistant rapidity bins are $2.2 < y_1 < 2.4$ and $2.4 < y_2 < 2.6$, and the last rapidity bin is $2.6 < y_3 < 2.7$. In all what follows, we will keep this phase-space division as function of transverse momentum and rapidity.

As a first exploratory study, the acceptance calculation of the generated neutral pions which decay into two photons requires a number of conditions including the geometry of detector. These imposed requirements were explained in much more details within the physics Event generator Section (See Section 4.2). The acceptance can be simply define by the ratio between the number of found particles $nAcc$ inside a fiducial geometrical zone which define the detector limit and the number of generated particles $nGen$ in the full phase-space 4π. It can be expressed as:

$$\varepsilon_{acc}(p_t, y) = \frac{nAcc(p_t, y)}{nGen(p_t, y)} \tag{4.7}$$

Under these circumstances the π^0 acceptance is illustrated in figure (4.21). The π^0 acceptance of the first two rapidity intervals y_1 in red squares, y_2 in blue circles and y_3 in light blue triangles. The acceptance is low at lower transverse momentum regions for all the rapidity bins and starts to increase at high momentum. The acceptance of first two rapidity intervals is large (approximately by a factor 2) in comparison with the last rapidity interval.

For more reliable approach, it was important to ensure, as far as possible, that the Monte Carlo simulation reproduces the experimental data correctly. This cross check is needed for the reconstruction efficiency evaluation by using the complete

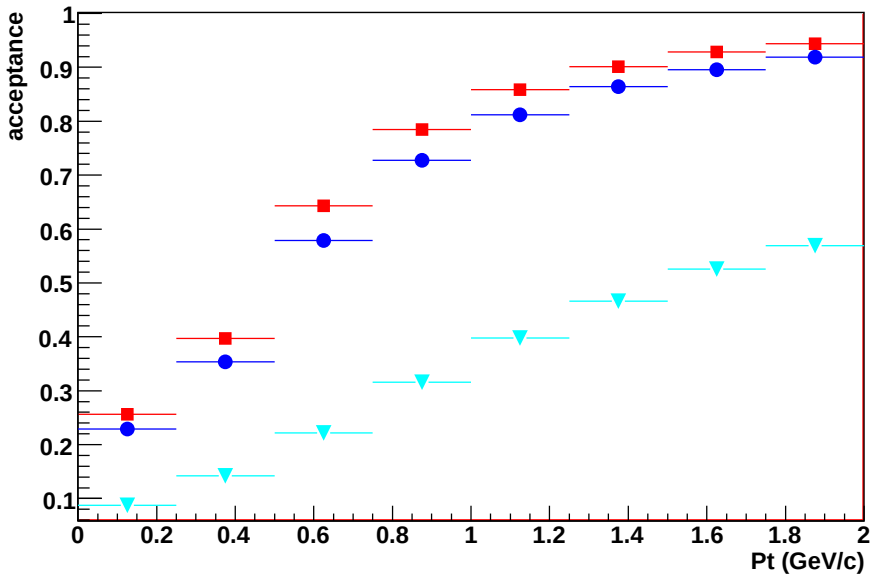

Figure 4.21: The acceptance of the neutral pion in the CERES experiment as function of rapidity and transverse momentum. The red squares are for 2.2< y2.4, the blue circles for 2.4< y2.6 and the light blue triangles refers to the last rapidity range 2.6< y2.7.

Overlay Monte Carlo simulation information.
The reconstruction efficiency can be defined as the ratio of the integrated reconstructed neutral pion yields by the simulated neutral pions which theirs γ's from the decay cross the entire volume of the detector. It can be defined as:

$$\varepsilon_{rec.eff} = \frac{nRec}{nAcc} \tag{4.8}$$

where the numerator ($nRec$) was explained and obtained from the reconstruction part of the Overlay Monte Carlo which is similar to the experimental data analysis, and the denominator ($nAcc$) indicates the number of the neutral pions passed through the detector simulation described by the GEANT software within the acceptance. The evaluated reconstruction efficiency for the three different rapidity bins indicated previously is shown in figure (4.22). It includes the conversion probability for each photon.

The equations (4.7) and (4.8) provide us the geometrical acceptance and the reconstructed efficiency. They are used to determine directly the correction factor. The total or the physical efficiency is then defined as the probability of neutral pion simulated within a geometrical acceptance and produced during 158 AGeV/c Pb-Au

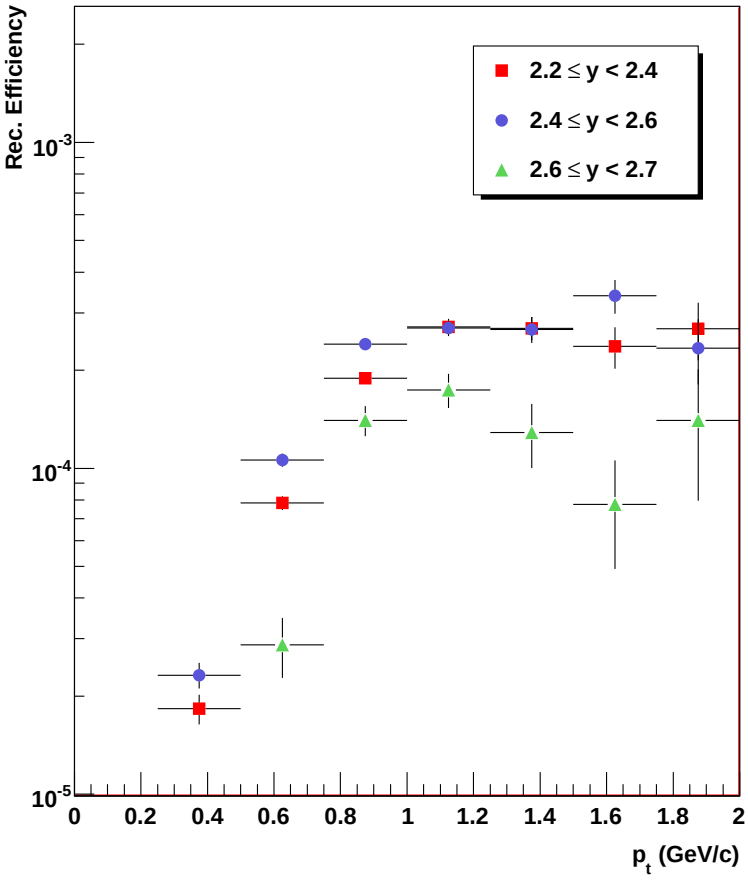

Figure 4.22: Reconstruction efficiency distributions versus the π^0 transverse momentum studied for different rapidity bins.

collisions at 7% centrality in the CERES spectrometer. Consequently, the physical efficiency of the simulated π^0s which cover such available phase-space is then given by the product $\varepsilon_{acc}.\varepsilon_{rec}$. This factor will be used later to correct the production rate of the measured neutral pions obtained from the experimental data analysis. One have to keep in mind that in the low momentum regions, the generation of a large multiplicity is needed in the Overlay Monte Carlo simulations due to the strong dependence of the π^0 detection efficiency with the transverse momentum.

It is in the admission of ignorance and the admission of uncertainty that there is a hope for the continuous motion of human beings in some direction that doesn't get confined, permanently blocked, as it has so many times before in various periods in the history of man.

Richard P. Feynman

5 Results

The results of the measured neutral pion presented in this Chapter have been obtained from an analysis of the data taken in 158 AGeV/c Pb-Au collisions for the most central collisions (7%). They are obtained using the experimental analysis method explained previously. The correction factor $\varepsilon_{acc} \times \varepsilon_{rec} \times BR$ is used to correct the integrated invariant mass distributions. The π^0 signals which have been studied as function of transverse momentum and rapidity are used to obtain the transverse momentum spectra of the neutral pion. A followed comparative study of our measurements with another experimental results as well as theoretical calculations is of great interest.

5.1 The total π^0 yields

The invariant mass distributions for the neutral pion were studied differentially as functions of transverse momentum and rapidity. The physical signals are presented in figures (3.28), (3.29) and (3.30) of the Chapter 3. The analysis of the π^0 measurement was carried out for $28 \cdot 10^6$ events. The phase-space with the production strategy was divided in 8 p_t bins and in three rapidity bins y_1, y_2 and y_3. It has been shown that measurements of the ratio of the $\gamma\gamma$ invariant mass for the same event to the one in mixed events is used to determine the normalization factor of the combinatorial background. The transverse momentum extends within the interval 0.25 GeV/c < p_t <2 GeV/c and equidistant rapidities y_1 and y_2 and in third bin y_3. The yield was calculated by integrating the invariant mass distribution of the two photons in the obtained signal region defined as $\mu \pm 2\sigma$. The uncorrected yields for

each y bins are illustrated in the figure (5.1).

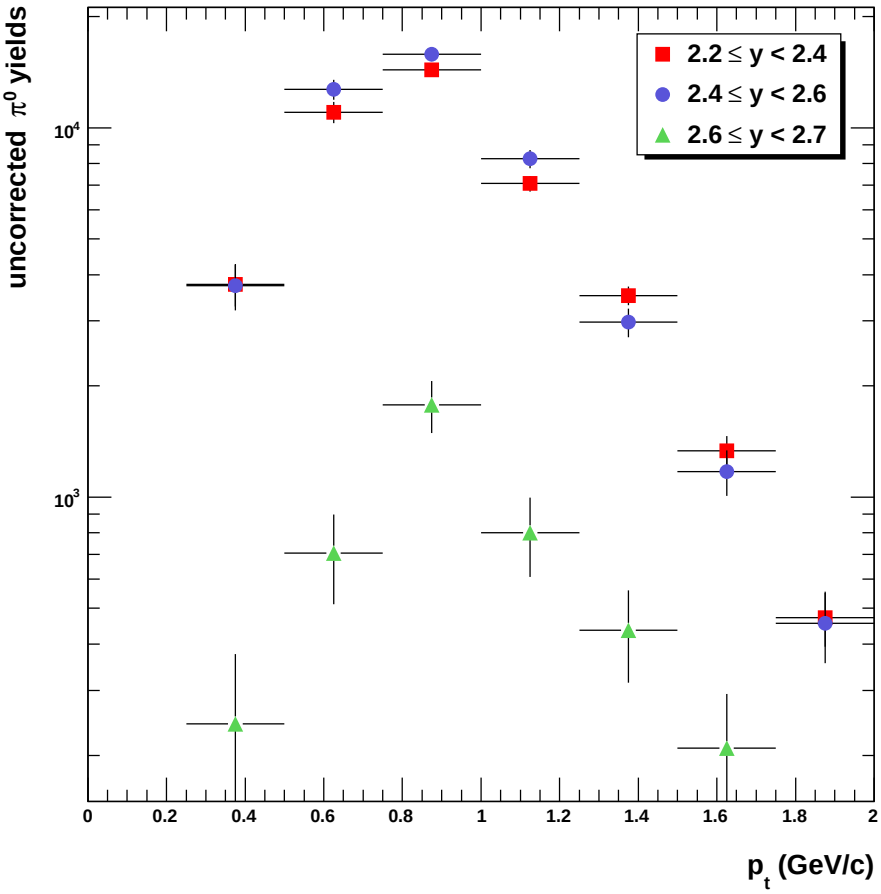

Figure 5.1: The uncorrected neutral pion yields as function of transverse momentum and rapidity.

The errors shown on the histograms are the statistical errors. We integrate the π^0 yields over all p_t interval in each rapidity bin. The performed method of the yield extraction from the invariant mass distributions and the fits works very well in all p_t and rapidity bins with sufficient statistics, except in the first p_t bin where we do not measure the neutral pions, and in y_3 where the statistics is relatively low. Hence according to these trends, one can see clearly that the yields in y_3 range are poor. In order to investigate this effect, the integrated π^0 yields in each rapidity bin are presented in table 5.1.

Rapidity range	Number of π^0
$y_1 : 2.2 - 2.4$	41493
$y_2 : 2.4 - 2.6$	45070
$y_3 : 2.6 - 2.7$	4200

Table 5.1: Total number of π^0 measured in each rapidity bin.

5.2 The Corrected Neutral Pion spectra

The raw yield has to be corrected, and the results depend strongly on the factors which were calculated in Section 4.8. They must then be corrected for the efficiency and the acceptance of the detector as well as for the branching ratio of π^0 to two photons of 98%. We will now give a short general description of the emission of neutral pion meson which is usually conducted in a two dimensions: the rapidity and transverse momentum (mass). Complementary to the goal observables for a produced particle defined with it momentum and energy, there are single particle observables of great importance like the p_t and the differential cross section of the production mechanism. The particle production can be expressed as in the phase space as:

$$\frac{d^3\sigma}{d^3p} = \frac{d^3\sigma}{p_t dp_t d\theta dp_z} \tag{5.1}$$

Where the θ is the emission angle of the particle in request (π^0 meson). Thus this can be re-written by considering the symmetry in the full phase space as:

$$\frac{d^2\sigma}{p_t dp_t dp_z} = \int_0^{2\pi} \frac{d^3\sigma}{p_t dp_t d\theta dp_z} d\theta \tag{5.2}$$

$$= 2\pi \frac{d^3\sigma}{p_t dp_t d\theta dp_z} \tag{5.3}$$

Furthermore, one can conclude from the fact that $dy = dp_z/E$, the following relation:

$$\frac{d^3\sigma}{d^3p} \propto \frac{d^2N}{2\pi p_t dp_t dp_z} \tag{5.4}$$

Thus the Lorentz-invariant differential cross section can be linked to the particle production as:

$$E\frac{d^2\sigma}{d^3p} \propto \frac{d^2N}{2\pi p_t dp_t dy} \tag{5.5}$$

In addition to the efficiency and acceptance correction factors, the number of the analyzed events and the branching ratio of the π^0 $0.988 \pm 0.032\%$ have to be included in the production rate $d^2N/2\pi p_t dp_t dy$. The fully corrected transverse momentum spectra is shown in figure (5.2).

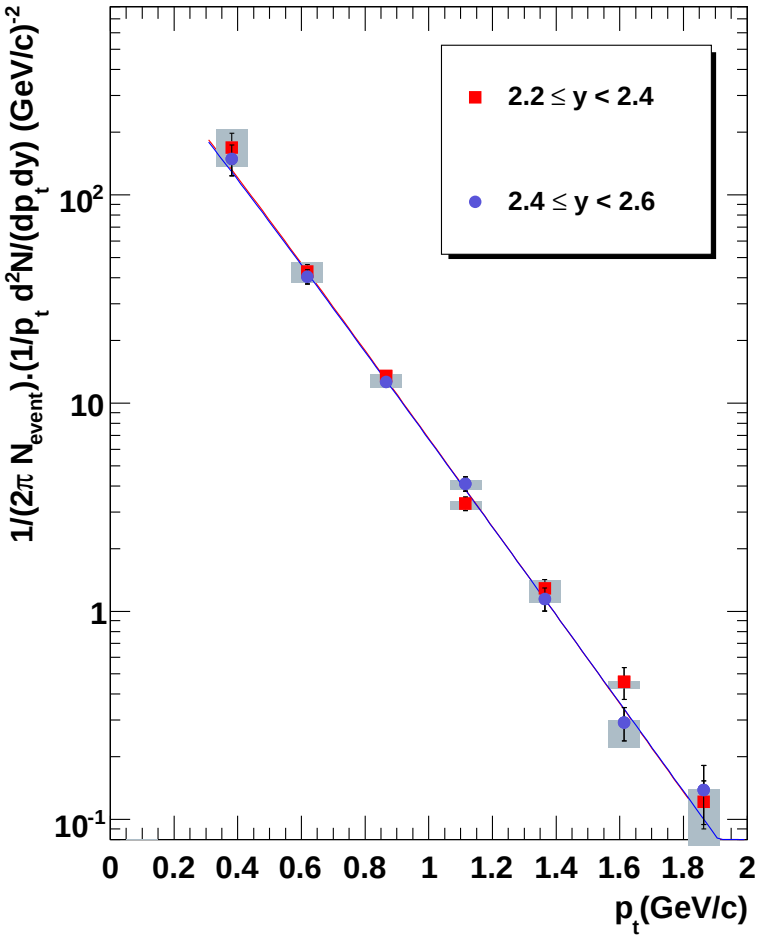

Figure 5.2: The corrected neutral pion transverse momentum spectra, the error bars are only statistical errors. Systematic errors are drawn as boxes.

Rapidity range	**T (MeV/c)**	dN/dy
$y_1 : 2.2 - 2.4$	204±6 (stat) ± 4 (sys)	215 ± 17 (stat) ± 12 (sys)
$y_2 : 2.4 - 2.6$	205±5 (stat) ± 5 (sys)	210 ± 15 (stat) ± 20 (sys)

Table 5.2: The measured inverse slope and the rapidity density in each rapidity range.

The π^0 transverse momentum in studied in the rapidity ranges and fitted with the function:

$$\frac{1}{2\pi}\frac{d^2N}{p_t dp_t dy} = \frac{1}{2\pi}\frac{dN/dy}{T.(T+m_0)}.exp\left(-\frac{\sqrt{m_0^2+p_t^2}-m_0}{T}\right) \tag{5.6}$$

Where $A = dN/dy$, $m_0 = 0.1349766$ GeV/c^2 is the neutral pion mass in the rest frame and T is the inverse slope which corresponds to the temperature parameter. Each transverse momenta spectra is fitted with the function indicated in the equation (5.6) and the corresponding temperature and dN/dy values are obtained. The T and dN/dy parameters of the fit function refers to the inverse slope and the rapidity density, respectively. The corresponding measured parameters of the fit function in each rapidity bin are listed in table 5.2.

5.3 The systematic uncertainties

The previous last two chapters have enable us to understand how to determine the π^0 transverse momentum corrected for efficiency and acceptance. The method used to extract the π^0 signal should have the statistical and systematic errors. The statistical errors depends on the neutral pion signal extracted in the $\gamma\gamma$ invariant mass distributions and the correction of the π^0 spectra using the Monte Carlo simulations. In addition to these two errors, we must add the systematic errors related to the different methods and cuts used in every step in the analysis and the Monte Carlo simulations. The estimation of the systematic errors of the final neutral pion measurements results mainly from uncertainties in the determination of the photon reconstruction, peak extraction, applied pair cuts and knowledge of the material. This step have been investigated with extensive studies by varying the polar angle cut of the reconstructed photons and then cross check the correct neutral pion transverse momentum spectra. The evaluation of the systematic errors are calculated by fitting the subtracted background of the $\gamma\gamma$ invariant mass distributions with different fit functions and by varying the two photon opening angle as function of p_t. These calculation steps are listed as follow:

- In our standard analysis we fit the $\gamma\gamma$ invariant mass distributions in different p_t and rapidity bins with gaussian function, then evaluating the π^0 yields by

integrating the $\gamma\gamma$ invariant mass distributions in the range $\mu \pm 2\sigma$. This calculation is applied in all the next steps.

- Fitting the $\gamma\gamma$ invariant mass distributions in the p_t range and rapidity bins mentioned in the first point with gaussian function and polynomial of the first order, then performing the integration of the π^0 signal.
- In this step we use different cut on the opening angle between the two photons mainly in the second p_t bin where we have required $0.10 rad$ and in the third p_t bin equal to $0.07 rad$ in the three rapidity regions (see table 3.2, for the definition of the standard cut). The $\gamma\gamma$ invariant mass distributions are then fitted by gaussian function.
- We use a gaussian function and a polynomial of the first order to fit the $\gamma\gamma$ distributions which results from the previous cut set.
- A global systematic uncertainty that will change the efficiency is coming from the missing material. To the best of our knowledge only the spokes holding the RICH2 mirror are missing in the Geant simulation. Our best estimation for this correction is a factor 1.05. This value is obtained from using the RICH2M volume, the volume of the spokes and the corresponding radiation length of each volume.

The final systematic errors on each point for the evaluation of the yields depending on the different fit functions and the opening angle cuts is presented in table 5.3.

5.4 Comparison to the CERES negative hadrons (h-)

The corrected π^0 transverse momentum spectra can be compared firstly to the negative hadrons measured also by the CERES experiment in the same data set [101] for the rapidity from 2 to 2.6. The negative hadrons are composed by π^-, K^-, and $\overline{P}$, π^- being the dominant contribution. The K^-/π^- ratio obtained in the thermal model [36] is 0.129 and the NA49 measured value is 0.095 ± 0.001 [98]. On the other hand, π^0/π^- ratio is approximately 1.07 due to the larger number of decays into π^0. Therefore, part of the extra contribution from the K^- cancels out, and only a difference of about 3 to 6 % is expected. The comparison is presented on figure (5.3). The π^0 yield is systematically larger than the h^-.

5.5 Comparison with UrQMD and PHSD models

The soft interactions are not described within the perturbative quantum chromodynamics (pQCD) because of the small Q^2 scale, whereas the pQCD is applicable to

y	p_t (GeV/c)	Material	Cuts	Fit	Total
2.2-2.4	0.25-0.5	$^{+21.77}_{-0.41}$%	$^{+0.43}_{-11.87}$%	$^{0}_{-3.8}$%	$^{+21.77}_{-12.47}$%
2.4-2.6	0.25-0.5	$^{+4.27}_{-8.24}$%	$^{+20.46}_{-0}$	$^{0}_{-2.04}$	$^{+20.9}_{-8.48}$%
2.2-2.4	0.5-0.75	$^{+6.32}_{-0.}$%	$^{+7.47}_{-1.35}$%	$^{0}_{-0.}$%	$^{+9.73}_{-1.35}$%
2.4-2.6	0.5-0.75	$^{+17.24}_{-0.}$%	$^{0}_{-7.04}$	$^{0}_{-1.42}$	$^{+17.24}_{-7.18}$%
2.2-2.4	0.75-1.	$^{+2.14}_{-0.}$%	$^{+2.65}_{-0.68}$%	$^{0}_{-2.18}$%	$^{+3.4}_{-2.28}$%
2.4-2.6	0.75-1.	$^{+9.27}_{-0.04}$%	$^{+1.20}_{0}$	$^{0}_{-6.5}$	$^{+9.34}_{-6.5}$%
2.2-2.4	1-1.25	$^{+4.3}_{-5.06}$%	$^{+2.72}_{0}$%	$^{0}_{-3.79}$%	$^{+5.8}_{-6.32}$%
2.4-2.6	1-1.25	$^{+0.3}_{-6.05}$%	$^{+3.12}_{0}$	$^{0}_{-3.01}$	$^{+3.13}_{-6.75}$%
2.2-2.4	1.25-1.5	$^{+0.63}_{-10.20}$%	$^{0}_{-3.03}$%	$^{0}_{-3.36}$%	$^{+0.63}_{-11.15}$%
2.4-2.6	1.25-1.5	$^{+21.70}_{-0.01}$%	$^{0}_{-4.14}$	$^{4.17}_{0}$	$^{+22.09}_{-4.14}$%
2.2-2.4	1.5-1.75	$^{+2.04}_{-4.92}$%	$^{+3.82}_{0}$%	$^{0}_{-5.99}$%	$^{+4.3}_{-7.75}$%
2.4-2.6	1.5-1.75	$^{0}_{-23.60}$%	$^{2.28}_{0}$	$^{0.17}_{0}$	$^{+2.82}_{-23.60}$%
2.2-2.4	1.75-2	$^{+3.13}_{-11.12}$%	$^{0}_{-0.006}$%	$^{0}_{-6.61}$%	$^{+3.13}_{-12.71}$%
2.4-2.6	1.75-2	$^{0}_{-45.76}$%	$^{0}_{-1.09}$	$^{1.17}_{0}$	$^{+1.17}_{-45.77}$%

Table 5.3: The different contributions to the estimated systematic uncertainties.

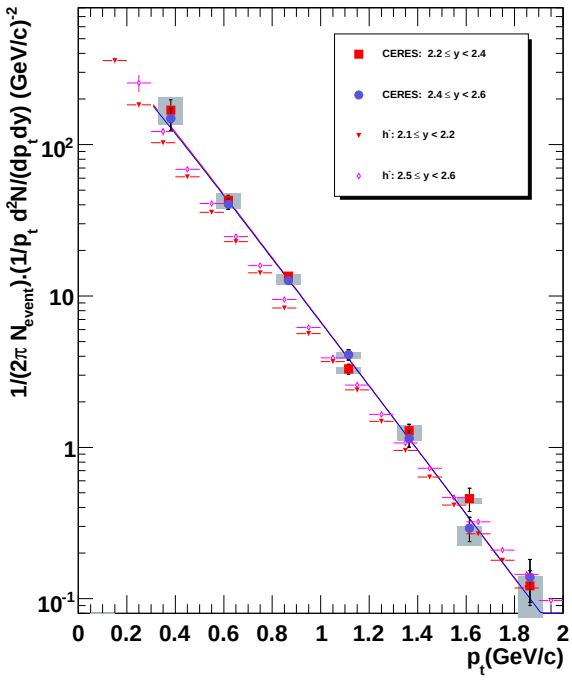

Figure 5.3: The corrected transverse momentum spectra compared to the CERES negative hadrons

describe the hard process with the large Q^2 four-momentum transfer. Consequently, the phenomenological models are needed to describe the collisions which are mainly happening at low transverse momentum. We will start by giving a brief description about the theoretical models that we use for the our comparison with our measured neutral pion.

Hadronic and nuclear collisions models have been developed to study macroscopic (statistical and hydrodynamical) systems and microscopic (string, transport, etc) systems. The microscopic models describe the subsequent individual hadron-hadron collisions such as the UrQMD model. The Ultra-relativistic Quantum Molecular Dynamic model (UrQMD) [102, 103] is microscopic transport model based on phase-space description of nuclear reactions. The UrQMD applies especially at high-energy collisions such as those produced in the energy range SIS up to AGS, SPS and RHIC. It therefore simulates the color strings formation and hadronic interactions at low and intermediate energies.

The comparison between experimental observations and the UrQMD predictions can

bring many information on the dynamics of the collision. The UrQMD model includes the color strings formation and their subsequent fragmentation into hadrons. The model is built upon a Monte-Carlo solution where a large set of partial differential equations for time evolution phase space densities of particle species and where each the nucleon is represented by Gaussian coherent state in the phase space. UrQMD initializes the projectile and target nuclei. We need just to set the two nuclei, beam energy and impact parameter and then we receive a list with all particles for each reaction. The total running time for first check is on the order of a couple of hours for some hundred events. The creation of transverse momentum spectra is then straight forward step, where we ask only for the PDG particle code for the particle identification.

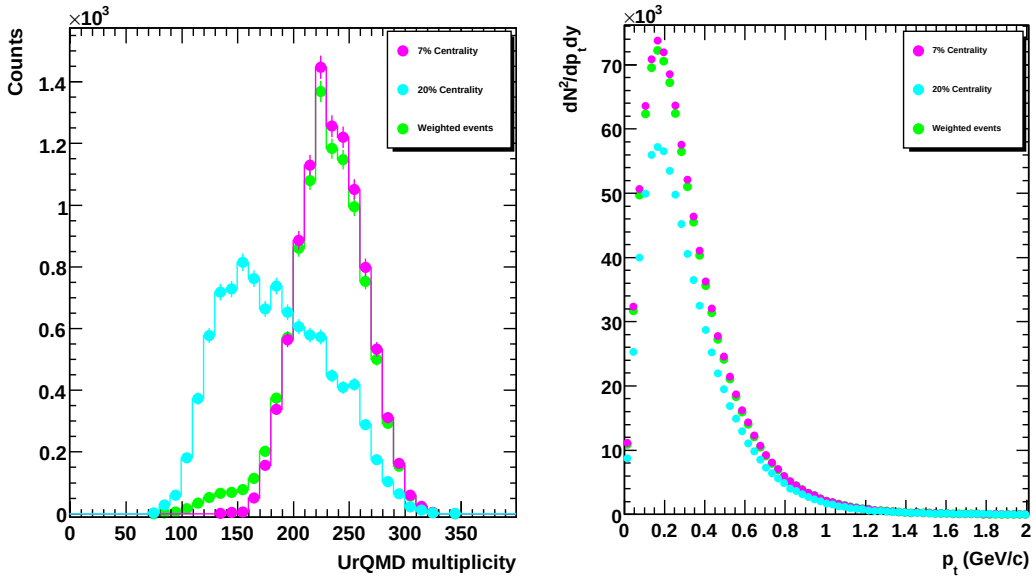

Figure 5.4: The left panel illustrates the UrQMD transport model charged particle multiplicity for different centralities. The light blue line represents the 20 % centrality events, the 7 % are represented by the magenta line and the weighted centrality in green which is the sum of 7% centrality events with factor 0.91 and the 20 % with factor 0.09. The neutral pion transverse spectra for different UrQMD centralities are shown on the right panel.

As starting point we have to check the TPC and UrQMD charged particle multiplicities, before comparing the neutral pion transverse momentum spectra to predictions of the UrQMD transport model. For that purpose, we produce two set of events in the UrQMD model to describe Pb-Au collisions at $\sqrt{s} = 17.2$ GeV/c. The

first set is for the 7% most central collisions, with the impact parameter $0 < b < 3.9$ fm.
To get good correspondence between the charged particle multiplicity distributions in UrQMD and in the data, the UrQMD multiplicity have been scaled up by a factor of 1.1 such that the two distributions agree. The second set consists of events created with a larger impact parameter $0 < b < 6.6$ fm, i.e. 20% centrality. The UrQMD π^0 distributions are obtained in the rapidity range $2.2 < y < 2.7$. The total UrQMD distribution is then the sum of the two different UrQMD distributions with the proper factors for each of them as given from the amount of data taken for each of the two centralities (see Section 3.1). The figure (5.4) presents the two different set of the produced events together the weighted average. In the left panel, the UrQMD multiplicities are shown and in the right panel, the neutral pion transverse momentum spectra with the UrQMD transport model for the different centralities is indicated. The comparison of the UrQMD model and the TPC multiplicities is shown in figure (5.5)

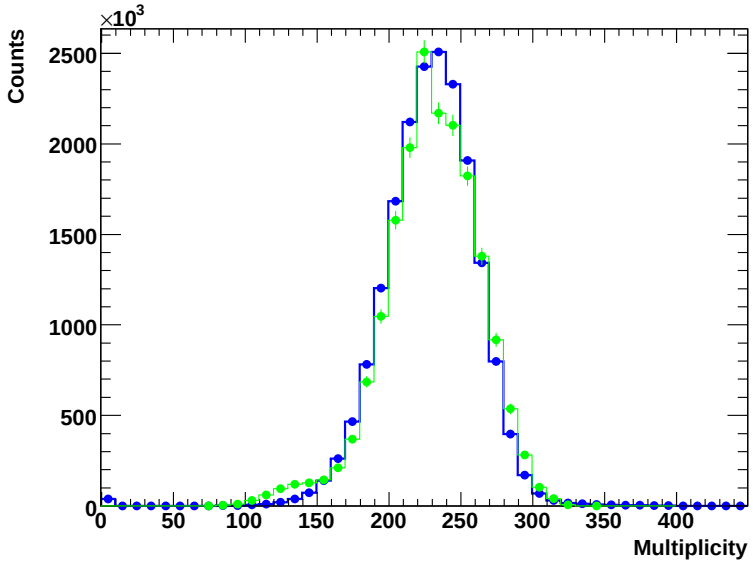

Figure 5.5: The comparison of the UrQMD transport model multiplicity in green and the TPC multiplicity in blue.

The second microscopic covariant transport model that will be compared to our results is the Parton-Hadron-String-Dynamics (PHSD) model [104, 105]. The relativistic hadronic transport approach is formulated to provide a dynamical description of parton-parton interactions (quark-gluon interaction). The concept of

this model is also based essentially on hadronic reactions, formation and decay of baryonic and mesonic resonances. The degrees of freedom are dynamical quarks, antiquarks, and gluons $(q, \overline{q}, g)$. The hadronic part is equivalent to conventional HSD approach [106]. The partonic part is based on DQPM [107, 108] where the following elastic and inelastic interaction are included $qq \leftrightarrow qq, \overline{qq} \leftrightarrow \overline{qq}, gg \leftrightarrow gg, gg \leftrightarrow g$, and $q\overline{q} \leftrightarrow g$. The PHSD results for the neutral pion spectra are for Pb-Pb collisions with 7% centrality in the rapidity bins 2.2-2.4, 2.4-2.6 and 2.2-2.6 [109].
The neutral pion transverse momentum spectra is compared to UrQMD and PHSD predictions. This is shown in figure (5.6). Both models show a different slope compared to the data.

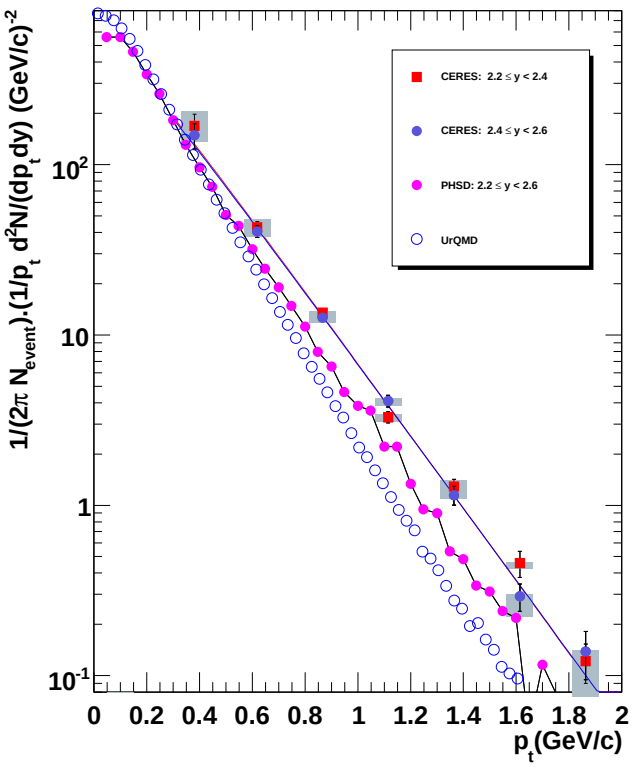

Figure 5.6: The corrected transverse momentum spectra compared to the UrQMD and PHSD phenomenological models.

5.6 Comparison with results from other SPS experiments

Before to compare our results with other experiments, the different measurement conditions have to be checked. Our results are compared with other SPS experiments, mainly the WA98 and NA49 experiments, which were performed at the same beam energy. The neutral pion measured by the WA98 experiment in Pb-Pb at 158 GeV/c are reconstructed using the decay channel $\pi^0 \longrightarrow \gamma\gamma$ within the pseudo-rapidity region $2.3 < \eta < 3.0$ for the centrality selection σ/σ_{geo} <6.8 % [93]. Figure (5.7) shows the comparison to neutral pions from the WA98 experiment and the negative pions from NA49 experiment.

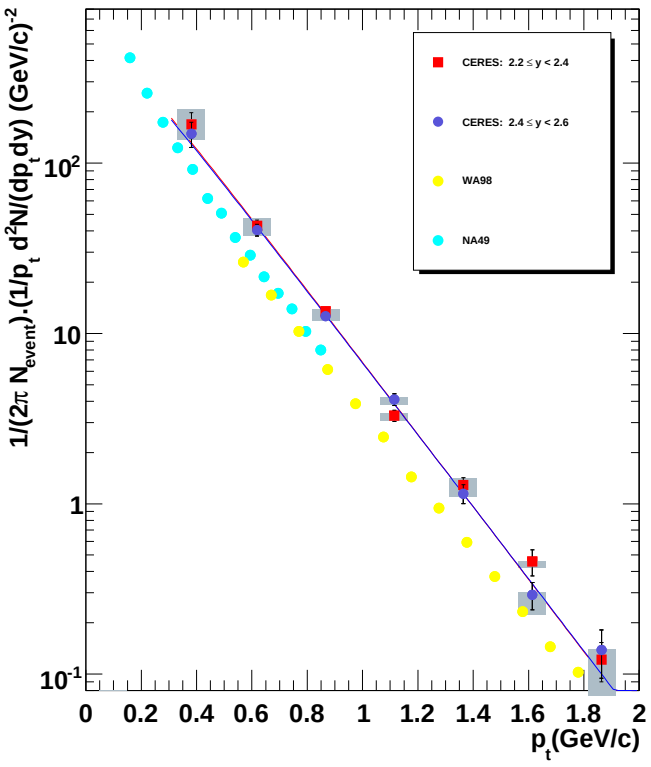

Figure 5.7: Comparison of the neutral pions transverse momentum presented in this work with the neutral pions measured by WA98 experiment (yellow circles) and negative pion from the NA49 experiment (light blue circles).

This comparison is done with π^- measurements from the NA49 experiment. The negative pions were produced at $0 < y < 0.2$ midrapidity [98]. One can scale the π^- from the NA49 experiment to our measured neutral pions by using the ratio π^-/π^0 from the thermal model [36]. is shown in figure .

In science one tries to tell
people, in such a way as to be
understood by everyone, something
that no one ever knew before.
But in poetry, it's the exact opposite. .

Paul Dirac

6

Conclusions and Outlook

In this Thesis work, the neural pions via theirs decay channel $\pi^0 \longrightarrow \gamma\gamma$ in 158 AGeV/c Pb-Au collisions have been measured. The neutral pion decays with 98.8 % probability within a fast life time scale. This physical process making the principal source of photons which convert into e^+e^-.
A method to measure photons that convert shortly before the TPC via the measurement of e^+e^- pairs in the TPC has been developed where the specific energy loss (dE/dx) information for each track provided by the CERES TPC was employed to identify the electron pairs. The main physics characteristic of the photon conversion, namely, the small opening angle between the e^+ and the e^- is used in order to identify photons. For that, a detailed study of the opening angle of the e^+-e^- pairs as function of momentum was performed to obtain the cut value. To select the photons that convert (shortly) before the TPC, mainly in the RICH2 mirror, we have developed a technique to reconstruct the Secondary vertices. By studying the Secondary vertex Z-position distributions as function of the momentum and the polar angle of the photon, we have defined a new cut to select only the photons which convert in the RICH2 mirror area. A good position resolution on the Secondary vertices and identification has been obtained.
We have identified the neutral pion mesons via the reconstruction of the invariant mass of all the photons combinations. All the photons which will not participate into the π^0 signal are then taken as combinatorial background that is calculated by the mixing event technique. To optimize the significance an opening angle cut between the two photons as function of the transverse momentum of the π^0 was implemented. However in order to suppress a part to the pronounced combinatorial background

at small transverse momentum regions, a tighter opening angle between the photon pairs in that phase space region was needed to improve the π^0 signal. A precise determination of electron/positron four-momentum, leads to a precise measurements of the photon momenta. A typical width of the π^0 peak of about 5 MeV/c^2 to 10 MeV/c^2 is obtained with this method compared to 15 MeV/c^2 obtained in the WA98 experiment based on a lead glass calorimeter.
The phase space of the data analysis was divided in the rapidity range $2.2 < y < 2.7$ and in 8 p_t bins, the number of π^0 as function of p_t for three rapidity intervals has been calculated by integrating the background subtracted invariant mass distributions of the photons pairs.
We have seen that the shapes of the neutral pion distributions are well reproduced in both cases the Monte Carlo simulations and in the data. The π^0 yields for the first two rapidity regions were larger than the last rapidity bin. The neutral pion yields were then corrected for the reconstructed efficiency and the geometrical acceptance factors. The main source of systematic error in this analysis was encountered mainly from uncertainties in the good mapping determination of the photon reconstruction in the Monte Carlo and the data. An other important source of the systematic errors comes from the knowledge of the reconstructed efficiency at low transverse momentum. As the e^+ and e^- from the converted photon are characterized by a very low p_t and, the efficiency of the standard tracking drops rapidity below momenta of 0.6 GeV/c, small difference between efficiency of data and MC will have an influence on the final results. In this p_t cut of 0.150 GeV/c on the photons has been used.
The obtained results were compared to two theoretical models (UrQMD and PHSD), and to experimental measurements from the CERES, WA98 and NA49 experiments. The measured rapidity density for the first rapidity range $dN/dy = 215 \pm 17(sta)$ and the corresponding inverse slope $T = 204 \pm 6(stat) \pm 4(sys)$, int the second rapidity we measure $dN/dy = 210 \pm 15(stat) \pm 20(sys)$and the inverse slope value $T = 205 \pm 5(stat) \pm 5(sys)$. The WA98 measurements have a 20% p_t independent systematic uncertainty for the neutral pion spectrum in central Pb+Pb collisions. Our results are systematically larger by approximately a factor 1.7 compared to WA98 results and by factor 1.6 with NA49 measurements. This difference is beyond the systematic errors quoted by the experiments.
The presented analysis method in this Thesis work can be used in the ALICE experiment which will start seeing first collisions in this year. The key detector in the central barrel of ALICE is also a TPC. We can simulate π^0 and η decays in the ALICE framework. The direct photons are one of the QGP signal, they are very difficult to measure experimentally due to the large background from π^0 and η meson decays. To accomplish this task one have to know the π^0 and η spectra with very high precision.

Bibliography

[1] S. L. Glashow. Partial Symmetries of Weak Interactions. *Nucl. Phys.*, 22:579–588, 1961.

[2] Abdus Salam. Weak and Electromagnetic Interactions. Originally printed in *Svartholm: Elementary Particle Theory, Proceedings Of The Nobel Symposium Held 1968 At Lerum, Sweden*, Stockholm 1968, 367-377.

[3] Steven Weinberg. A Model of Leptons. *Phys. Rev. Lett.*, 19:1264–1266, 1967.

[4] Andrew Watson. *The Quantum Quark*. Cambridge University Press, 2004.

[5] John F. Donoghue. General relativity as an effective field theory: The leading quantum corrections. *Phys. Rev.*, D50:3874–3888, 1994.

[6] John F. Donoghue. Introduction to the Effective Field Theory Description of Gravity. 1995.

[7] Chris Quigg. Beyond the standard model in many directions. 2004.

[8] T. P. Cheng and L. F. Li. Gauge theory of elementary particle physics. Oxford, Uk: Clarendon (1984) 536 P. (Oxford Science Publications).

[9] Chen-Ning Yang and Robert L. Mills. Conservation of isotopic spin and isotopic gauge invariance. *Phys. Rev.*, 96:191–195, 1954.

[10] T. Muta. Foundations of quantum chromodynamics. Second edition. *World Sci. Lect. Notes Phys.*, 57:1–409, 1998.

[11] Michael E Peskin and Daniel V Schroeder. *An Introduction to Quantum Field Theory; 1995 ed.* Addison-Wesley, New York, 1995. Includes exercises.

[12] Murray Gell-Mann. A Schematic Model of Baryons and Mesons. *Phys. Lett.*, 8:214–215, 1964.

[13] G. Zweig. An SU(3) model for strong interaction symmetry and its breaking. CERN-TH-401.

[14] Lowell S. Brown. Quantum Field Theory. Cambridge University Press . (Oxford Science Publications).

[15] D. J. Gross and Frank Wilczek. Asymptotically Free Gauge Theories. 1. *Phys. Rev.*, D8:3633–3652, 1973.

[16] Gerard 't Hooft. On the Phase Transition Towards Permanent Quark Confinement. *Nucl. Phys.*, B138:1, 1978.

[17] E. C. G. Stueckelberg and A. Petermann. Normalization of constants in the quanta theory. *Helv. Phys. Acta*, 26:499–520, 1953.

[18] D. J. Gross and Frank Wilczek. Ultraviolet behavior of non-abelian gauge theories. *Phys. Rev. Lett.*, 30:1343–1346, 1973.

[19] H. David Politzer. Reliable perturbative results for strong interactions? *Phys. Rev. Lett.*, 30:1346–1349, 1973.

[20] S. Bethke. Determination of the QCD coupling α_s. *J. Phys.*, G26:R27, 2000.

[21] L. Montanet et al. Review of particle properties. Particle Data Group. *Phys. Rev.*, D50:1173–1823, 1994.

[22] J. D. Bjorken. Asymptotic Sum Rules at Infinite Momentum. *Phys. Rev.*, 179:1547–1553, 1969.

[23] Richard P. Feynman. Very high-energy collisions of hadrons. *Phys. Rev. Lett.*, 23:1415–1417, 1969.

[24] M. Luscher, K. Symanzik, and P. Weisz. Anomalies of the Free Loop Wave Equation in the WKB Approximation. *Nucl. Phys.*, B173:365, 1980.

[25] J. Engels, F. Karsch, and H. Satz. A finite size analysis of the heavy quark potential in deconfining medium. *Nucl. Phys.*, B315:419, 1989.

[26] V. Bornyakov et al. Heavy quark potential in lattice QCD at finite temperature. 2003.

[27] Keith A. Olive. The Quark - hadron transition in cosmology and astrophysics. *Science*, 251:1194–1199, 1991.

[28] E.W. Kolb and M.S. Turner. *The Early Universe*. Addison-Wesley, Redwood City, 1990.

[29] John R. Ellis, Joseph I. Kapusta, and Keith A. Olive. Phase transition in dense nuclear matter with quark and gluon condensates. *Phys. Lett.*, B273:123–127, 1991.

[30] John R. Ellis, Joseph I. Kapusta, and Keith A. Olive. Strangeness, glue and quark matter content of neutron stars. *Nucl. Phys.*, B348:345–372, 1991.

[31] Norman K. Glendenning. FAST PULSAR IN SN1987A: CANDIDATE FOR STRANGE QUARK MATTER. *Phys. Rev. Lett.*, 63:2629, 1989.

[32] Edward V. Shuryak. Quark-Gluon Plasma and Hadronic Production of Leptons, Photons and Psions. *Phys. Lett.*, B78:150, 1978.

[33] Peter Braun-Munzinger and Johanna Stachel. The quest for the quark-gluon plasma. *Nature*, 448:302–309, 2007.

[34] P. Braun-Munzinger, J. Stachel, J. P. Wessels, and N. Xu. Thermal and hadrochemical equilibration in nucleus-nucleus collisions at the SPS. *Phys. Lett.*, B365:1–6, 1996.

[35] P. Braun-Munzinger, D. Magestro, K. Redlich, and J. Stachel. Hadron production in Au Au collisions at RHIC. *Phys. Lett.*, B518:41–46, 2001.

[36] A. Andronic, P. Braun-Munzinger, and J. Stachel. Hadron production in central nucleus nucleus collisions at chemical freeze-out. *Nucl. Phys.*, A772:167–199, 2006.

[37] Bertrand C. Barrois. Superconducting Quark Matter. *Nucl. Phys.*, B129:390, 1977.

[38] Roberto Turolla, Silvia Zane, and Jeremy J. Drake. Bare quark stars or naked neutron stars? The case of RX J1856.5-3754. *Astrophys. J.*, 603:265–282, 2004.

[39] Kenneth G. Wilson. Confinement of quarks. *Phys. Rev.*, D10:2445–2459, 1974.

[40] John B. Kogut. An Introduction to Lattice Gauge Theory and Spin Systems. *Rev. Mod. Phys.*, 51:659, 1979.

[41] John B. Kogut. The lattice gauge theory approach to quantum chromodynamics. *Rev. Mod. Phys.*, 55(3):775–836, Jul 1983.

[42] Frithjof Karsch. Lattice results on QCD thermodynamics. *Nucl. Phys.*, A698:199–208, 2002.

[43] B. Alessandro et al. ALICE: Physics performance report, volume II. *J. Phys.*, G32:1295–2040, 2006.

[44] P. Glassel. The ALICE TPC: An innovative device for heavy ion collisions at LHC. *Nucl. Instrum. Meth.*, A572:64–66, 2007.

[45] J. D. Bjorken. Highly Relativistic Nucleus-Nucleus Collisions: The Central Rapidity Region. *Phys. Rev.*, D27:140–151, 1983.

[46] Helmut Satz. Limits of confinement: The first 15 years of ultra- relativistic heavy ion studies. *Nucl. Phys.*, A715:3–19, 2003.

[47] Jean-Paul Blaizot. Signals of the quark-gluon plasma in nucleus nucleus collisions. *Nucl. Phys.*, A661:3–12, 1999.

[48] John W. Harris and Berndt Muller. The search for the quark-gluon plasma. *Ann. Rev. Nucl. Part. Sci.*, 46:71–107, 1996.

[49] P. Braun-Munzinger and J. Stachel. (Non)thermal aspects of charmonium production and a new look at J/psi suppression. *Phys. Lett.*, B490:196–202, 2000.

[50] T. Matsui and H. Satz. J/psi Suppression by Quark-Gluon Plasma Formation. *Phys. Lett.*, B178:416, 1986.

[51] C. Y. Wong. Introduction to high-energy heavy ion collisions. Singapore, Singapore: World Scientific (1994) 516 p.

[52] Yasuo Miake Kohsuke Yagi, Tetsuo Hatsuda. *Quark-gluon plasma : An Ultimate state of matter*. Cambridge Univ. Press, 2005.

[53] Joseph I. Kapusta, P. Lichard, and D. Seibert. High-energy photons from quark-gluon plasma versus hot hadronic gas. *Phys. Rev.*, D44:2774–2788, 1991.

[54] R. Baier, H. Nakkagawa, A. Niegawa, and K. Redlich. Production rate of hard thermal photons and screening of quark mass singularity. *Z. Phys.*, C53:433–438, 1992.

[55] Thomas Peitzmann and Markus H. Thoma. Direct photons from relativistic heavy ion collisions. *Phys. Rept.*, 364:175–246, 2002.

[56] F. Arleo et al. Photon physics in heavy ion collisions at the LHC. 2004.

[57] G. Agakishiev et al. Enhanced production of low mass electron pairs in 200-GeV/u S - Au collisions at the CERN SPS. *Phys. Rev. Lett.*, 75:1272–1275, 1995.

[58] G. Agakishiev et al. Systematic study of low-mass electron pair production in p Be and p Au collisions at 450-GeV/c. *Eur. Phys. J.*, C4:231–247, 1998.

[59] G. Agakishiev et al. Low-mass e+ e- pair production in 158-A-GeV Pb Au collisions at the CERN SPS, its dependence on multiplicity and transverse momentum. *Phys. Lett.*, B422:405–412, 1998.

[60] D. Adamova et al. Enhanced production of low-mass electron pairs in 40-A-GeV Pb Au collisions at the CERN SPS. *Phys. Rev. Lett.*, 91:042301, 2003.

[61] R. Baur et al. The CERES RICH detector system. *Nucl. Instrum. Meth.*, A343:87–98, 1994.

[62] P. Holl et al. Study of electron pair and photon production in Pb - Au collisions at the CERN SPS: Addendum to proposal SPSLC/P280. CERN-SPSLC-96-35.

[63] G. Agakishiev et al. First results from the CERES radial TPC. *Nucl. Phys.*, A661:673–676, 1999.

[64] The CERES Collaboration. The CERES/NA45 Radial Drift Time Projection Chamber. *Nucl. Instrum. Meth.*, A593:203–231, 2008.

[65] CERES Collaboration. CERN SPSLC/96-35/P280/Add 1. 1996.

[66] CERES Collaboration. CERN SPSLC/96-50 SPSLC/R110. 1996.

[67] A. Marin. New results from CERES. *J. Phys.*, G30:S709–S716, 2004.

[68] D. Miskowiec. Collections of CERES results. *Nucl. Phys.*, A774:43–50, 2006.

[69] H. Appelshauser. Physics with the upgraded CERES detector. *Acta Phys. Polon.*, B29:3153–3159, 1998.

[70] E. Gatti and P. Rehak. Semiconductor drift chamber - an application of a novel charge transport scheme. *Nucl. Instrum. Meth.*, A225:608–614, 1984.

[71] O. Nix. *Diploma Thesis,Einsatz und Lasertest von 4" Siliziumdriftdetektoren.* Universität Heidelberg, 1996.

[72] J. Seguinot and T. Ypsilantis. Photoionization and Cherenkov Ring Imaging. *Nucl. Instr. Meth.*, 142:377, 1977.

[73] Dissertation G.Hering. Technische Universität Darmstat, 2001.

[74] W.R. Leo. *Techniques for Nuclear and Particle Physics Experiments*. Springer-Verlag, 1987.

[75] W.Schmitz. *Dissertation*. Universität Heidelberg, 1996.

[76] K.Kleinknecht and T.D.Lee. *Particles and Detectors*. Springer-Verlag, 1986.

[77] R. Veenhof. GARFIELD, recent developments. *Nucl. Instrum. Meth.*, A419:726–730, 1998.

[78] Wilrid Ludolphs. *PhD thesis, Measurement of open charm in 158-AGeV/c Pb - Au collisions*.

[79] Sergey Yurevich. PhD Thesis, Electron-pair production in 158-AGeV/c Pb Au collisions from CERES.

[80] R. Brun, R. Hagelberg, M. Hansroul, and J. C. Lassalle. GEANT: Simulation program for particle physics experiments. User guide and reference manual. CERN-DD-78-2-REV.

[81] Computing CERN Application Software Group and Networks Division. Geant detector description and simulation tool. 1993. http://wwwasd.web.cern.ch/wwwasd/geant.

[82] Walter Blum, Luigi Rolandi, and Werner Riegler. Particle detection with drift chambers. Berlin, Germany: Springer (2008) 448 p.

[83] D. H. Perkins. *Introduction to High Energy Physics,fourth edition*. Cambridge University Press, 2000.

[84] C. Amsler et al. Review of particle physics. *Phys. Lett.*, B667:1, 2008.

[85] Yung-Su Tsai. Pair Production and Bremsstrahlung of Charged Leptons. (Erratum). *Rev. Mod. Phys.*, 49:421–423, 1977.

[86] M. Sánchez García. *Dissertation: Momentum Reconstruction and Pion Production Analysis in the HADES Spectrometer at GSI*. Universidade de Santiago de Compostela, 2003.

[87] Siegmund Brandt. *Data Analysis: Statistical and Computational Methods for Scientists and Engineers*. Springer, 1998.

[88] D. Drijard, H. G. Fischer, and T. Nakada. Study of event mixing and its application to the extraction of resonance signals. *Nucl. Instr. Meth.*, A225:367, 1984.

[89] D. L'Hote. About Resonance signal extraction from multiparticle data: combinatorics and event mixing methods. *Nucl. Instrum. Meth.*, A337:544–556, 1994.

[90] P. Crochet and P. Braun-Munzinger. Investigation of background subtraction techniques for high mass dilepton physics. *Nucl. Instrum. Meth.*, A484:564–572, 2002.

[91] J. Podolanski and R. Armenteros. Analysis of v-events. *Phil. Mag.*, 45:13–30, 1954.

[92] Christoph Blume. *Dissertation: Produktion neutraler Pionen in heier hadronischer Materie*. University of Muenster, 1998.

[93] M. M. Aggarwal et al. Transverse mass distributions of neutral pions from Pb-208 induced reactions at 158-A-GeV. *Eur. Phys. J.*, C23:225–236, 2002.

[94] John Adams et al. Photon and neutral pion production in Au + Au collisions at s(NN)**(1/2) = 130-GeV. *Phys. Rev.*, C70:044902, 2004.

[95] R. Brun and F. Rademakers. ROOT: An object oriented data analysis framework. *Nucl. Instrum. Meth.*, A389:81–86, 1997.

[96] Johanna Stachel. Towards the quark-gluon plasma. *Nucl. Phys.*, A654:119c–135c, 1999.

[97] C. Hohne. Strangeness production in nuclear collisions: Recent results from experiment NA49. *Nucl. Phys.*, A661:485–488, 1999.

[98] S. V. Afanasiev et al. Energy dependence of pion and kaon production in central Pb + Pb collisions. *Phys. Rev.*, C66:054902, 2002.

[99] P. Braun-Munzinger, I. Heppe, and J. Stachel. Chemical equilibration in Pb + Pb collisions at the SPS. *Phys. Lett.*, B465:15–20, 1999.

[100] R Brun, F Bruyant, M Maire, A C McPherson, and P Zanarini. *GEANT 3: user's guide Geant 3.10, Geant 3.11; rev. version*. CERN, Geneva, 1987.

[101] Ana Marin. Private communication.

[102] S. A. Bass et al. Microscopic models for ultrarelativistic heavy ion collisions. *Prog. Part. Nucl. Phys.*, 41:255–369, 1998.

[103] M. Bleicher et al. Relativistic hadron hadron collisions in the ultra- relativistic quantum molecular dynamics model. *J. Phys.*, G25:1859–1896, 1999.

[104] W. Cassing and E. L. Bratkovskaya. Parton transport and hadronization from the dynamical quasiparticle point of view. *Phys. Rev.*, C78:034919, 2008.

[105] W. Cassing. From Kadanoff-Baym dynamics to off-shell parton transport. *Eur. Phys. J. ST*, 168:3–87, 2009.

[106] W. Ehehalt and W. Cassing. Relativistic transport approach for nucleus nucleus collisions from SIS to SPS energies. *Nucl. Phys.*, A602:449–486, 1996.

[107] A. Peshier and W. Cassing. The hot non-perturbative gluon plasma is an almost ideal colored liquid. *Phys. Rev. Lett.*, 94:172301, 2005.

[108] W. Cassing. QCD thermodynamics and confinement from a dynamical quasiparticle point of view. *Nucl. Phys.*, A791:365–381, 2007.

[109] Elena Bratkovskaya. Private communication about the PHSD transport calculations.

Acknowledgments

I wish to express firstly my gratitude to Prof.Dr. Johanna Stachel for accepting me to join her group, and for all the offered support and guidance.

I would like to thank Prof.Dr. Norbert Herrmann, Prof.Dr. Matthias Bartelman and Prof.Dr. Jürgen Schaffner-Bielich for accepting to be the members of the examination committee.

I am deeply indebted to Dr. Ana Marin for her stimulating suggestions and encouragements. I remember now all the difficult analysis problems that have been passed away by making extreme effort to solve them and boost the several ideas till the end. I learned with her a lot and how the research can be the fontain of knowledge by a simple key: communication. Muchas gracias Ana.

I want to thank my CERES colleagues for all their interest, support and valuable discussion. Especially, I would like to thank Dr. Dariusz Miskowiec for his well ordered explanations and for all the exchanged emails.
I am thankful for the International Research Training Group where I benefit too much. The IRTG program enabled me to understand more the new developments in the Intelgent Detectors in physics.

I want to thank my colleagues at the Physikalische Institut: Kathrine, David, Kai and Hans Kristian for their encouragement and passing nice time with a constructive discussions. I am very thankful to my friend Joseph (Syracuse University) for passing together a long time discussing the analysis issues and techniques.
I would like also to convey thanks to my Professors: Prof. Olivier Pene at Orsay, and at the ICTP: Prof. Goran Senjanovic, Prof. Faheem Hussain, Dr. Borut Bajc, and Prof. Bobby Acharya for their encouragement and advises during my studies. Thanks also to Dr. Francois Arleo for his nice Lectures about the Photon world within the QGP where I learned how physics became wonderful with a very good Maestro. Merci Francois.

Special thanks goes to my parents for their understanding and endless love

through all the duration of my studies till arriving to this stage. My wife Linda, my daughter Tasnime, my sisters and my brothers for their patience and support in all the times.